2008-07-10

Ion Permeation through Membrane Channels: Molecular Dynamics Simulations Studies

Morad Mustafa
Brigham Young University - Provo

ION PERMEATION THROUGH MEMBRANE CHANNELS: MOLECULAR DYNAMICS SIMULATIONS STUDIES

by

Morad Mustafa

A dissertation submitted to the faculty of

Brigham Young University

in partial fulfillment of the requirements for the degree of

Doctor of Philosophy

Department of Chemistry and Biochemistry

Brigham Young University

August, 2008

BRIGHAM YOUNG UNIVERSITY

GRADUATE COMMITTEE APPROVAL

of a dissertation submitted by

Morad Mustafa

This dissertation has been read by each member of the following graduate committee and by majority vote has been found to be satisfactory.

Date	Douglas J. Henderson, Chair
Date	David D. Busath
Date	Matthew C. Asplund
Date	S. Scott Zimmerman
Date	Dean R. Wheeler

BRIGHAM YOUNG UNIVERSITY

As chair of the candidates graduate committee, I have read the dissertation of Morad Mustafa in its final form and have found that (1) its format, citations, and bibliographical style are consistent and acceptable and fulfill university and department style requirements; (2) its illustrative materials including figures, tables, and charts are in place; and (3) the final manuscript is satisfactory to the graduate committee and is ready for submission to the university library.

Date

Douglas J. Henderson
Chair, Graduate Committee

Accepted for the Department

David V. Dearden
Graduate Coordinator

Accepted for the College

Thomas W. Sederberg
Associate Dean, College of Physical and
Mathematical Sciences

ABSTRACT

ION PERMEATION THROUGH MEMBRANE CHANNELS: MOLECULAR DYNAMICS SIMULATIONS STUDIES

Morad Mustafa

Department of Chemistry and Biochemistry

Doctor of Philosophy

Molecular dynamics simulation was used to study ion permeation through different membrane proteins embedded in a lipid bilayer (DMPC) with different saline solutions. The potential of mean force (PMF) for ion transport was obtained by umbrella sampling simulations.

A revised MacKerell force field for tryptophan residues was studied using gramicidin A (gA) channel as a test model. The revised force field contribution to the Na^+ PMF was consonant with the prediction from the experimental results, but in stark contrast to the prediction of the CHARMM force field, version 22, for the tryptophan side-chain.

A new grid-based correction map algorithm by MacKerell group, called CMAP, was introduced into the CHARMM force field, version 31. The CMAP algorithm focused on optimizing ϕ, ψ dihedral parameters for the peptide backbone. The CMAP corrections reduced the excessive translocation barrier. Decomposition demonstrated the reduction in the translocation barrier was due to effects on the K^+ PMF_{H_2O} rather than on K^+ PMF_{gA}.

The presence of negatively charged sulfonate group at the entrance and exit of the gA channel affected the depth and the location of the highly occupied sites. The negatively charged sulfonate group produced a strong attraction for the cations in the bulk towards the channel mouth .

In the M_2 transmembrane domain channel (M_2-TMD), three M_2-TMD structures were studied, differing only in whether the selectivity-filter (four His^{37} side-chains) was uncharged, $+2$ charged, or $+3$ charged. M_2-TMD structural properties were compared with the structural properties of other models extracted from NMR and X-ray studies. The spontaneous cation and anion entry into the charged selectivity-filter was different from that into a neutral selectivity-filter. Cl^- ions had a lower free-energy barrier in the selectivity-filter than either Na^+ or NH_4^+ ions through the M_2-TMD channel. NH_4^+ ions had a lower free-energy barrier in the selectivity-filter than Na^+ ions. Based on accessible rotamer conformations, a revised conductance mechanism was proposed. In the proposed conductance mechanism, the His^{37} side-chain functioned as an acceptor and donor group, whereas the Trp^{41} side-chain functioned as a carrying group.

ACKNOWLEDGMENTS

Praise be to Allah, Lord of the worlds, the Beneficent, and the Merciful.

I acknowledge with special thanks all of my family members and friends for their support, encouragement, and prayers.

I owe my gratitude to Douglas Henderson and David Busath for their continual guidance, assistance, support, directions, and encouragement. Thanks to all of my graduate committee members for their support, help, and suggestions. I also wish to thank the Department of Chemistry and Biochemistry at BYU and its staff for their help.

I am grateful for the financial support of a Roland K. Robbins Graduate Research Fellowship. A generous allotment of computer time by the Ira and Marylou Fulton Supercomputing Center at BYU is acknowledged with thanks.

Table of Contents

List of Tables

List of Figures

Chapter 1

Introduction

1.1 Computer Simulations

Computer simulations of molecular systems utilize computer programs or algorithms, which run on one computer or on a network of computers.[1,2] These programs attempt to simulate the motions and observable configurations for the molecular system under study, which mimic those motions and observables in a particular realistic system under certain conditions.[1,2] The ability of computer simulation to bridge between the theoretical and the experimental worlds makes it very useful. For example, molecular simulation allows one to subject the molecular system to drastic conditions that cannot be performed in real experiments, such as high temperature or pressure.[3,4]

Based on time-dependent properties, molecular simulations are divided into two main categories, Monte Carlo and molecular dynamics simulations.[1,2]

1.1.1 Monte Carlo Simulation

Monte Carlo (MC) simulation is a technique that involves extensively generating random numbers in its calculations.[1,2] Random numbers should be chosen at random. However, even the best random number generator introduces a bias through a cycle in the random numbers.[1,2] That is, the random numbers are really only pseudo random.[1,2] However, with a good random number generator this bias is small with a long period for the cycle and, except in unusual situations, does not intro-

duce an error.[1,2] These random numbers are used with an algorithm, most commonly the Metropolis algorithm, that focuses upon the region of phase space that is favorable and of interest.[1,2]

The Metropolis method has three important steps, which are summarized as: first, randomly, a particle is selected and its potential energy (Φ) is calculated; second, a random displacement is given to this particle and its new potential energy (Φ') is calculated; finally, the new position is accepted based on the probability function $\{\text{minimum } [1, \exp(-(\Phi' - \Phi)/(k_B T)]\}$, where k_B is Boltzmann's constant and T is system's temperature.[1,2] This technique does not generate time-dependent properties for the system under study.

The MC method has not been applied successfully to problems, such as those problems considered in this dissertation, that involve both ions and water molecules even though it has been applied successfully to problems involving only ions and only water molecules. Every ion move is rejected in a system that has both salt and explicit water molecules (personal communication, Dezső Boda). It is believed the rejection issue is due to the fact that the Metropolis algorithm is a single particle algorithm. In contrast, the molecular dynamics method, which we now consider, moves all the particles simultaneously and has been applied to problems with both ions and water molecules.

1.1.2 Molecular Dynamics Simulation

Molecular dynamics (MD) simulation is a technique that applies known laws of physics (Newton's equations of motion) on the simulated atoms for a period of time.[1,2] The equations of motion deal with the intermolecular interactions, which resemble realistic system interactions.[1,2] It is difficult to have analytical solutions for these physics equations, when there is a large number of simulated atoms.[1,2] Therefore, numerical methods are used to obtain a solution for these physics equations.[1,2] The results of an MD simulation depend on which force fields have been used in the simulation.

Force fields are potential functions and parameters that describe the forces, which are the derivatives of the potential-energy, on the atoms.[5] They may include bond stretching, bond-angle bending, out-of-plane bending, torsion angles, interactions between these kinds of motion, van der Waals attractions and repulsions between non-bonded atoms, and electrostatic interactions between atoms.[5]

Two sources are commonly used in the development of the force fields, namely, ab initio calculations and experimental observations.[5] There are different force fields that are primarily developed for macromolecules, such as AMBER (Assisted Model Building with Energy Refinement), CHARMM (Chemistry at HARvard Macromolecular Mechanics), and GROMOS (GROningen MOlecular Simulation).[5] They exist as united-atoms, all-atoms, or both versions.[5] In the united-atoms force fields, such as GROMOS, the hydrogen atoms are not explicitly included bonded to aliphatic carbon atoms, whereas in the all-atoms force fields they are.[5]

MD simulation is an important tool for studying both biological and chemical systems. It can be used to study macromolecular vibrations at the atomic level, where macroscopic techniques cannot extract some biological phenomena, such as ligand-binding flexibility or details of protein-structural fluctuations.[6,7] For example, macromolecular structures can be restrained, with the aid of MD simulations, to be both energetically favored and compatible with the available NMR data.[8,9]

1.2 Free-Energy Calculations

Both MC and MD simulations can be used to calculate the Helmholtz free-energy difference (ΔA) between a system with a potential energy (Φ_0) and a system with a potential energy (Φ_1) as follows:[1,2]

$$\Delta A = -k_B T \ln\left[\frac{Q_1(N,V,T)}{Q_0(N,V,T)}\right], \tag{1.1}$$

$$= -k_B T \ln\left[\left\langle \exp\left(\frac{\Delta\Phi}{k_B T}\right)\right\rangle_0\right], \tag{1.2}$$

where N is the number of particles, V is the volume of the system, T is the temperature of the system, k_B is the Boltzmann's constant, Q is the canonical partition function, and $<\cdots>_0$ denotes an ensemble average in the reference system with Φ_0.

Nevertheless, MC and MD simulations may not efficiently produce certain statistical averages that represent properties like phase transition, protein folding, and ion transport because of high-energy barriers between limiting states, which are difficult to bypass with unrestrained MC or MD

simulations.[1,2] Therefore, free-energy sampling methods have been introduced, which can be used with either MC or MD method.[1,2]

There are many free-energy calculation methods in the field, which focus on barrier crossing problems.[1,2] For the scope of this work, we briefly mention one method, which is an umbrella sampling method.

1.2.1 Umbrella Sampling Method

The umbrella sampling method enhances sampling of configurational space regions by providing an appreciable overlap between a poorly and a well-sampled regions.[1,2] In MC simulations, umbrella sampling can be achieved by introducing a biasing weighting function ($W(\Phi)$) into the Metropolis calculations,[1,2] then subsequently removing it by the weighted histogram analysis method (WHAM).[10] Thus, the new position in MC simulations is accepted based on the new probability function (P):[1,2]

$$P = minimum\left[1, \left(\frac{W(\Phi_1)}{W(\Phi_0)}\right)\exp\left(-\frac{\Phi_1 - \Phi_0}{k_B T}\right)\right]. \tag{1.3}$$

In MD simulations, umbrella sampling can also be performed by introducing a biasing umbrella potential function, then subsequently unbiasing it using WHAM.[10] For example, the free-energy profile for an ion crossing through a membrane channel can be obtained this way.[11] The test ion can be set to sample closely spaced positions in configurational space along the transport coordinate and then restrained to the vicinity by a biasing potential. Having multiple independent simulations at different locations of the transport coordinate allows the test ion to efficiently explore the whole transport coordinate.

WHAM is a method to extract the potential of mean force (PMF), which is formally identical to the free-energy profile, from well-sampled trajectories.[10] Unbiasing the applied umbrella potential for each simulated "window" produces short segments of the PMF.[10] The WHAM equations, which are probability equations that deal with the configurational space, connect those PMF segments.[10]

WHAM results might be asymmetric [Fig. 1.1(a)], even though the simulated system is set to be symmetric. Different factors may contribute to that asymmetry, such as inadequate sampling, equi-

libration, or symmetry in the configuration. Traditionally, the statistical accuracy for symmetrical systems can be improved by symmetrization (i.e., averaging the two halves of the PMF profile). The symmetrization method primarily serves to average the free-energy effects due to asymmetries in the larger molecular configuration, such as protein and lipid positions, which can persist during the short umbrella sampling simulation. The symmetrization should be performed after the convergence of the PMF results is assured. Convergence, which reflects adequate local sampling, is illustrated by comparing the PMF profiles [Fig. 1.1(a)], which are constructed based on increasingly complete fractions of the simulation trajectories. Symmetrization is performed by averaging the free-energy values at positive and negative values of the zero-centered transport coordinate [Fig. 1.1(b)].

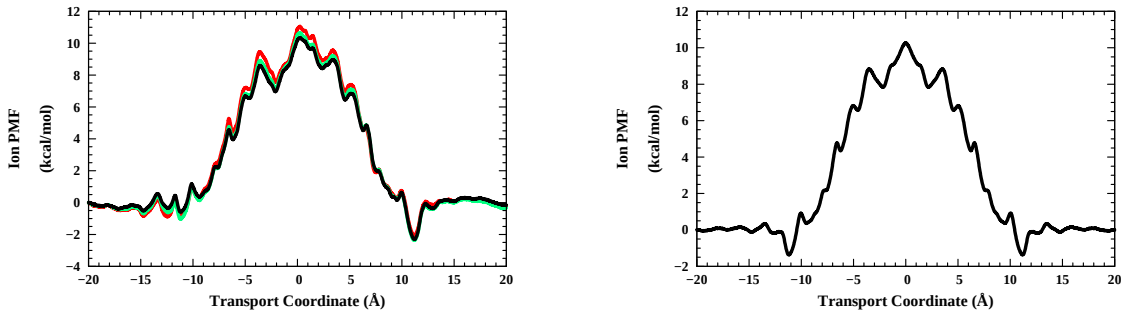

Figure 1.1: Asymmetrized and Symmetrized One-Dimensional ion PMFs as a function of the transport coordinate. (*a*) An asymmetrized ion PMF including different simulation times; 0.5 ns (red line), 0.75 ns (green line), and 1.0 ns (black line). (*b*) A Symmetrized ion PMF after 1.0 ns simulation time.

In the convergence demonstration [Fig. 1.1(a)], notice that the PMF converged to within 0.5 kcal/mol over the entire extent of the integration, whether based on 0.5, 0.75, or 1.0 ns, and to within 0.5 kcal/mol of the reference energy (0 kcal/mol at $z = -20$ Å) at the opposite z position ($z = 20$ Å). The demonstrated asymmetrized PMFs suggest that the energy uncertainty due to structural variations is on the order of ≈ 1 kcal/mol.

1.3 A New Improvement in the Force Fields

An improvement in the force fields, focused on the peptide backbone treatment, was recently introduced into the CHARMM force field, version 31, to improve the helix propensity of the protein backbone for protein-folding problems.[12] The improvement was introduced in the force field as a grid-based energy correction map to the CHARMM force field, version 22, which was called CMAP.[12] CMAP was extracted based on the dipeptide properties of L-alanine, glycine, and L-proline from quantum mechanical and molecular mechanical calculations.[12] After testing the initial quantum mechanics based corrections, CMAP required additional optimizations to compensate for the longer range (e.g., solvation) effects that were not included in the *in vacuo* ab initio simulations. These additional optimizations minimized the deviation between the simulation results and the experimental crystallographic data for various backbone positions of neighboring residues.[12] As implemented in the CHARMM force field, version 31, the optimized parameters that were obtained for L-alanine were also used for the other naturally occurring amino acids on the assumption that the side-chains would have little impact on the backbone energetics.

The CMAP corrections improve the treatment of protein-folding problems and protein-structural properties,[12] but its influence on other problems like the ion transport through membrane channels is unknown.

1.4 Scope of Work

Ion channels, which are integral membrane proteins that form pores through a plasma membrane, are important because they regulate ion flow across the plasma membrane.[13] Some ion channels selectively allow ion passage based on a particular charge type, magnitude, and species size,[13] such as in the case of the gramicidin channels. Other channels allow ion passage based on gating mechanisms,[13] such as ligand-gated channels like the acetylcholine and $GABA_A$ receptors, voltage-gated channels like Na^+, K^+, and Ca^{+2} channels, pH-gated channels like M_2 channels, or temperature-gated channels like transient receptor potential vanilloid receptors.

The first crystal structure obtained for an ion channel was for a rudimentary bacterial potassium

channel.[14] However, the potassium channel has neutral selectivity-filters. The selectivity-filter in cation-selective channels is a region of the channel, which is narrow and ringed by polar backbone or side-chains, that repels anions but attracts particular cations based on electrostatic and available volume effects. Because sodium and calcium channels differ dramatically in their physiological functions and have charged selectivity-filters,[13,15–18] how will a charged selectivity-filter affect the channel selectivity?

A notion was developed that calcium binding would be enhanced in a narrow selectivity-filter because of the competition of enthalpic electrostatic and available volume effects.[19] This notion was further developed with implicit water using MC[20–23] and Brownian dynamics[24–28] simulations. MD simulations with explicit water with a non-polarizable force field yielded little selectivity for Ca^{+2} passage over Na^{+} passage in a calcium-like channel.[29–31] But, the inclusion of polarizability in an MC study yielded strong Ca^{+2} selectivity for the Ca^{+2}-channel selectivity-filter and Na^{+} selectivity for the Na^{+}-channel selectivity-filter.[21] Furthermore, comparison of Brownian dynamics studies and MC simulations, both using implicit solvation, demonstrated that the charged moieties in the selectivity-filter must be exposed inside the selectivity-filter rather than buried in the walls to attain the high degree of selectivity revealed through electrophysiological experiments.[21,23]

Consequently, we explored the role of such charged ion pathways in two model systems: the gramicidin and the influenza A M_2 channels. In the gramicidin channel, introducing a negatively charged group at the channel entrance and exit enhanced the experimentally observed current flow,[32] but it is not known whether the negative charge enhances entry, translocation or exit. In the influenza A M_2 channel, where the selectivity-filter is titrated with protons in the active state, the channel was observed electrophysiologically to pass only protons.[33–36] The permeation of other ions through this channel is observed in experiments as well.[35,37–41]

We conducted MD and umbrella sampling simulations to study some aspects of dipolar and charged peptide moieties in gramicidin and M_2 channels. Also, we used the gramicidin channel as a test model to explore the effect of CMAP on the ion transport through a neutral channel. These are discussed in detail in Chapters 2–4. We used the NAMD package due to its many features, such as highly efficient parallelization and the flexibility of using different force fields, and the CHARMM

force field to allow direct comparison with numerous previous studies.

Besides the dissertation work, during my study at this university, six other papers on theoretical assessment of capacitor interfaces and MD simulations of emulsions have been published. These publications are listed in Appendix A. In addition to the published work, we have presented the dissertation work in scientific meetings. The presented papers are listed in Appendix B. The dissertation work has been submitted for publication. The detail of dissertation submission is mentioned in Appendix C.

It is very important in simulations that the molecular system resembles the configurational properties of a realistic molecular system, which allows the comparison between the two systems to be acceptable. Next, we discuss the importance of each preparation step for the system under study to achieve that goal.

1.4.1 Preparation Methodology

Starting from a crystal-like configuration requires a careful treatment until it gets to a well equilibrated and disordered configuration. For example, using periodic boundary conditions (PBC) in the molecular simulation helps to prevent the simulated molecules from evaporation and drifting away from each other.[1,2] Using the particle mesh Ewald (PME) method with the PBC on a periodic system enhances the convergence of electrostatic interactions calculations among the simulated molecules.[1,2]

Different methods can be used to achieve a well equilibrated and disordered configuration, but here we describe the steps of our methodology for preparing a system that consists of a protein embedded in a bilayer membrane.

1. Minimization: This process optimizes the system configuration by performing a particular algorithm, such as conjugate gradient. The algorithm minimizes the system energy at a particular temperature, usually 0 K, by looking for a structure that has no overlapped atoms. The minimization process runs under an NVT ensemble, where NVT stands for constant number of particles, constant volume, and constant temperature, respectively. Through the minimization process, the protein atoms are fixed at their original configuration to prevent them from

deviating from the experimentally derived structure. Also, the lipid head groups of the two bilayer leaflets are restrained at a particular separation distance to preserve the experimentally observed thickness.

2. Heating: This process sets the system to the desired temperature after the minimization process. Simply, starting from zero K, the heating process reassigns a new temperature to the system (i.e., new velocities based on the new temperature) every cycle of time steps. After each cycle of time steps the temperature is incremented by one. The increment process continues until the target temperature is achieved. The heating process runs under an NV ensemble, where the number of particles in the central volume are being held constant by the periodic boundary conditions, but the temperature is being varied during the heating process. Through the heating process, the protein atoms are fixed at their original configuration and the lipid head groups are restrained at the same separation distance as in the minimization process.

3. Equilibration 1: This process assures that free components of the system are thermally well equilibrated at the target temperature while the protein atoms are being fixed at their original configuration and the lipid head groups are being restrained at the same separation distance as in the minimization process. This equilibration process runs under an NVT ensemble using constant periodic boundary conditions and the Langevin dynamics to produce an effectively constant temperature.

4. Annealing: This process helps to disorder the lipid tails from the fully ordered form and produces realistic lipid properties. It consists of three stages with each stage including: 40 ps of heating to 1000 K followed by 80 ps of cooling to 303.15 K. The annealing process runs under an NV ensemble. Throughout the annealing process, the protein atoms are fixed at their original configuration and the lipid head groups are restrained at a the same separation distance as in the minimization process.

5. Equilibration 2: This process helps to switch the system from constant volume ensemble to constant pressure ensemble, after the annealing process. Throughout this equilibration pro-

cess, the protein atoms are being fixed at their original configuration and the force constant for the restraint on the lipid head groups is lowered. This equilibration process runs under an NPAT ensemble, where NPAT stands for constant number of particles, constant pressure, constant surface area, and constant temperature, respectively. Using a constant pressure ensemble in the annealing process often leads to a system explosion and does not provide enough space for the lipid tails to change their conformations. Therefore, if the constant pressure ensemble is needed, it should be used after the annealing process.

6. Equilibration 3: This process helps to obtain the experimentally surface area per head group, which prepares a realistic lipid environment for the peptide channel. Through this equilibration process, the protein atoms are being fixed at their original configuration and the force constant for the restraint on the lipid head groups is lowered. This equilibration process runs under an NPγT ensemble, where NPγT stands for constant number of particles, constant pressure, constant surface tension, and constant temperature, respectively. Surface tension (γ) is the force applied per unit length to a filament required to stretch a liquid film.[42,43] This equilibration process should run at least for 10 ns, and the details on how to choose the suitable γ value are discussed in Section 2.2.1.

7. Subsequent Equilibrations: These processes allow progressively release of all the applied restraints, letting the simulated system to run under natural forces. These processes run under an NPAT ensemble. In the NPAT ensemble of the the subsequent equilibration processes, the surface area represents a realistic surface area extracted from the end of the previous NPγT ensemble process. The choice of running the subsequent simulations under an NPAT ensemble allows us to compare our results with the results from previous studies.

Our preparation methodology is a general method and might be used with any molecular system that consists of protein and lipid molecules, even if minor modifications are needed based on the molecular system requirements. For example, the proteins in Chapters 2 and 3 (gramicidin A, gramicidin M, and taurine gramicidin A channels) have similar structural properties, which allow us to use the same procedure on all of them. The protein in Chapter 4 (transmembrane domain M_2

channel) is different from those proteins in Chapters 2 and 3 and has different structural properties, therefore, modification of the preparation methodology is needed. The detail of the preparation methodology for each protein system is discussed in the method section of each chapter.

Chapter 2

Direct and Indirect Effects of CHARMM Force Field Improvements

2.1 Background

The gramicidin A (gA) channel [Fig. 2.1(a)] is a polypeptide that dimerizes head–head to form a cation channel in lipid bilayer membranes. The gA channel is composed of two right-handed[44] single-stranded hydrogen-bonded $\beta^{6.3}$-helices[45,46] with the amino acid sequence: formyl-L-Val-L-glycine-L-alanine-D-Leu-L-alanine-D-Val-L-Val-D-Val-L-Trp^{9}-D-Leu-L-Trp^{11}-D-Leu-L-Trp^{13}-D-Leu-L-Trp^{15}-ethanolamine.[47] The gA channel has a simple well-known structure with well-defined functions.[8,48,49] Another interesting protein is the gramicidin M (gM) channel [Fig. 2.1(b)], where the tryptophan residues at positions 9, 11, 13, and 15 of gA channel are replaced with the phenylalanine residues. The tryptophan to phenylalanine replacement allows assessments of the difference in the side-chain dipole potentials along the channel transport pathway through measuring experimental channel currents and through MD simulations.

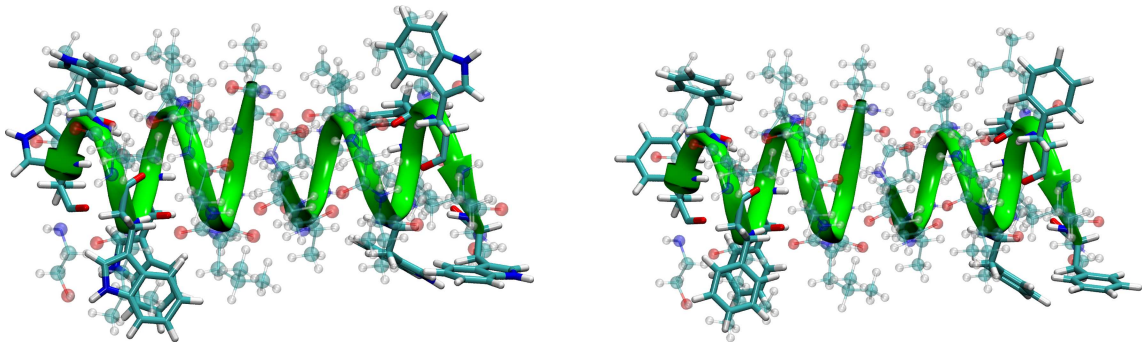

(a) **(b)**

Figure 2.1: Snapshots for (*a*) gA and (*b*) gM channels. Both proteins are drawn using the New Cartoon drawing method (with a green color) to represent the right-handed β-helices, and using the CPK drawing method to show all atoms. Both tryptophan and phenylalanine side-chains are drawn using the Licorice drawing method. The colored species represent: C (cyan), H (white), O (red), and N (blue).

The tryptophan side-chains are important for the gA channel organization and functions.[49–64] The tryptophan dipole moment affects the cation stability and affinity at the highly occupied site (HOS) (often called the binding site), the thermodynamic parameters of the cation affinity, and the cation free-energy barriers that govern the channel conductance.[8,65–75]

Binding site is a term loosely used by pharmacologists to refer to specific lock-in-key vdW–electrostatic–steric complementarity binding; by channelogists to refer to a local minimum in the free-energy profile; by biochemists to refer to a region on a protein, DNA, or RNA where specific ligands form selective van der Waals contacts through surface complementarity; and by biologists to refer to a region where an enzyme can attach itself to a compound and react with it. It is hard to know the limits on the use of the term binding site, and in gramicidin, the term has always been controversial (but still generally used) because the electrostatic factors causing the local minima in the free-energy profile appear to be long-range effects rather than intrinsic protein–ion interaction effects. Consequently, we prefer to use the term HOS instead of the term binding site because the long-range-electrostatic factors causing the local minima in the free-energy profile are specific in the sense that only one ion can fit at a time and it must be, with a few exceptions,[76,77] an alkali metal cation or ammonium, but not in the sense of complex ligand-shape complementarity.

A theoretical analysis of experimental results for gA, gM, and heterodimers of the two indicated

that the tryptophan dipole potential (relative to the phenylalanine dipole potential) must be bowl-shaped with a depth of ≈ -4.9 kcal/mol,[78] whereas version 22 of the CHARMM force field predicts a double-well potential for the static structure.[79] Because the ion potential is sensitive to the choice of the biomolecular force field,[11,80] could the dynamic average ion–Trp potential energy for gA be closer to experimental prediction if we use the newly recommended MacKerell force field[81] for tryptophan residues instead of version 31 of the CHARMM force field?

The cation-transport free-energy profiles, predicted by MD simulations,[11,80,82–89] yield a significantly higher translocation barrier than is expected from the predicted PMF from the physiological data.[78,90,91] The inclusion of the long-range-electrostatics corrections[11,80,84] and the introduction of polarizability[11,85,86,89,92] in the force field have partly alleviated this problem, but the relative roles of these and other factors are yet to be evaluated.

An improvement in the force fields, focused on the peptide backbone treatment, was introduced.[12] The improvement was introduced in the force field as a grid-based energy correction map, which was called CMAP.[12] CMAP was extracted based on the dipeptide properties of alanine, glycine, and proline from quantum mechanical and molecular mechanical calculations.[12] CMAP required additional optimized ϕ, ψ dihedral parameters to version 22 of the CHARMM force field, which minimized the deviation between the simulation results and the experimental crystallographic data for various backbone positions of neighboring residues.[12] The optimized parameters improve the treatment of protein-folding problems and protein-structural properties.[12]

Although the CMAP corrections are not chirally symmetric like version 22 of the CHARMM force field, we discovered that their use with the gA channel (in which alternate residues are of D chirality or glycine) yielded an improvement in the free-energy profile for cation transport. As we will show, the improvements (which admittedly may be fortuitous, in part, due to inaccurate corrections for the dihedral angles governing the D-residues) are due to indirect effects, mediated by channel water molecules.

How to obtain an accurate force field when switching from short-range[93] to long-range[72,74] interactions is a strong challenge for the ion permeation through membrane proteins and the selectivity mechanism of membrane channels. Therefore, we tested these two improvements, the new

MacKerell force field and the CMAP algorithm, on the ion permeation through the gA channel via umbrella-sampling simulations. Our findings show partial improvements for both issues and highlight the complications presented by indirect effects.

2.2 Methods

2.2.1 Model System and Parameters

The initial system consisted of a gA dimer, with the 1JNO structure [Fig. 2.1(a)],[8] embedded in 40 1,2-Dimyristoyl-sn-glycero-3-phosphocholine (DMPC) molecules as a lipid bilayer, as well as 2366 water molecules, and 1 mol/kg NaCl. The 1JNO structure is a relaxed structure, based on solution state NMR results for dimers in sodium dodecyl sulfate micelles,[8] and consistently reproduces the solution and the solid-state NMR properties.[94] The TIP3P model was used as the water model, which was modified in CHARMM from the original model[95]. The terminal residues, ethanolamine and formyl, were given their partial charges and force field parameters based on other similar atomic groups in the force field. The tryptophan residues were first given MacKerell force field parameters[81] and this system was denoted gA_{Mac}. The initial structure [Fig. 2.2(a)] was constructed, using the VMD software,[96] in a box with initial dimensions of $40 \times 40 \times 90$ Å in x, y, and z dimensions, respectively.

2.2.2 System Preparation

The total simulation time for system preparation was 25 ns, with different periodic boundary conditions and harmonic restraints (Table 2.1). The preparation included conjugate-gradient energy minimization of the initial configuration, followed by heating from 0 to 303.15 K, equilibration in the NVT ensemble, three-stages of annealing (40 ps of heating to 1000 K followed by 80 ps of cooling to 303.15 K), and progressive release of restraints on the protein over multiple stages of equilibration (Table 2.1). This preparation allowed relaxation of the protein and disordering the lipid molecules, ions, and water molecules [Fig. 2.2(b)] starting from the crystal-like structure [Fig. 2.2(a)].

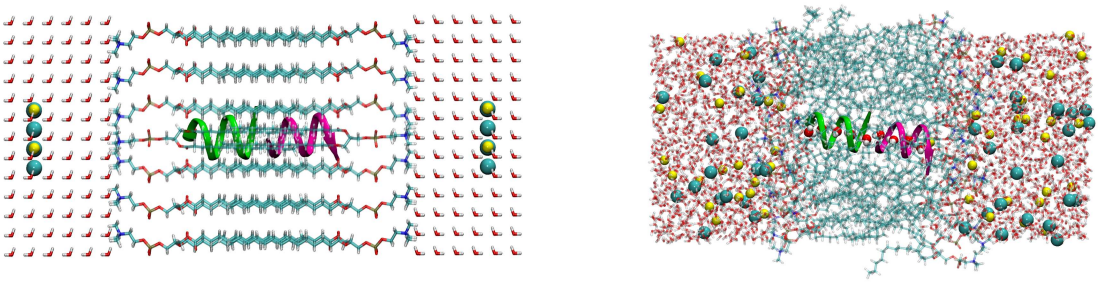

(a) **(b)**

Figure 2.2: gA_{Mac} System Snapshots: (*a*) Initially and (*b*) Equilibration 10 stage. gA dimer using the New Cartoon drawing method (green and magenta for left (L) and right (R) monomers, respectively); DMPC bilayer atoms using the Licorice drawing method: C (cyan), H (white), O (red), N (blue), and P (brown); Na^+ (yellow sphere); Cl^- (cyan sphere); Water atoms: O (red) and H (white). Nine water molecules inside the channel are shown using the CPK drawing method.

Table 2.1: Summary of a Gramicidin System Preparation Approach

Process	Ensemble [a]	Restraints (k_f [b], kcal/(mol·Å^2))				Steps
		Lipids [c]	Protein [d]			
		P	bb	non bb	COM	
Minimization	NVT	200	F	F		5000
Heating	NV	200	F	F		20,000
Equilibration 1	NVT	200	F	F		25,000
Annealing [e]	NV	200	F	F		200,000
Equilibration 2	NPAT	20	F	F		100,000
Equilibration 3	NPγT	10	F	F		10,000,000
Equilibration 4	NPAT	2	100	2		100,000
Equilibration 5	NPAT	1	40	1		100,000
Equilibration 6	NPAT		10			100,000
Equilibration 7	NPAT		2			100,000
Equilibration 8	NPAT		0.4			100,000
Equilibration 9	NPAT		0.1			400,000
Equilibration 10	NPAT				1000	1,250,000

[a] The symbols in this column stand for; N: constant number of atoms, V: constant volume, T: constant temperature, P: constant pressure, A: constant area, γ: constant surface tension

[b] k_f: force constant

[c] The symbol in this column stands for; P: phosphorus atoms

[d] The symbols in this column stand for; bb: backbone, COM: center-of-mass, F: fixed atoms

[e] It consists of three stages with each stage: 40 ps of heating to 1000 K followed by 80 ps of cooling to 303.15 K

Both the lipid deuterium order parameters and the lipid surface area are sensitive to the changes in the bilayer structures due to many factors, such as the lipid hydration level, number of lipid molecules, temperature, statistical ensemble, surface tension, and saline-solution concentration.[97–104] Surface tension (γ) is the force applied per unit length to a filament required to stretch a liquid film.[42,43] Mathematically, γ can be calculated in MD simulation of lipid bilayer system as follows:[100]

$$\gamma = \frac{1}{2}\left\langle L_z \times \left(P_{zz} - \frac{1}{2}(P_{xx} + P_{yy})\right)\right\rangle, \tag{2.1}$$

where L_z is the length of the unit cell, P_{zz} is the component of the pressure tensor normal to the surface, P_{xx} and P_{yy} are the tangential components of the pressure tensor, and the angle brackets denote an average over time. For simulating a pure lipid bilayer in pure water, the appropriate surface tension has been evaluated to be within the range of 30-45 dyn/(cm·interface).[100,102,105,106] However, with a more complex lipid bilayer system, such as one that includes salt and protein, the surface tension is unknown.

We carried out a test for the suitable surface tension using the Equilibration 3 stage conditions. The test was done by fixing the protein in the original 1JNO structure to avoid protein-surface perturbation effect on the lipid bilayer properties,[62] applying two planar harmonic restraints on the lipid phosphorus atoms (k_f = 10 kcal/(mol·Å^2)) at z = ± 17.5 Å to agree with the experimental head–head or phosphate–phosphate thickness of 35.3 Å,[107,108] and using 2.5 unit increments of the surface tension in the range of 0-75 dyn/(cm·interface). Based on accuracy and precision in the lipid molecular surface area, which was consistent with the experimental DMPC molecular surface area,[108] the optimal surface tension was found to be 40 dyn/(cm·interface).

The Equilibration 3 stage was then carried out with γ = 40 dyn/(cm·interface). In the Equilibration 3 stage, the protein was fixed in the original 1JNO structure, and two planar harmonic restraints were applied on the lipid phosphorus atoms (k_f = 10 kcal/(mol·Å^2)) at z = ± 17.5 Å (Table 2.1). This stage was run for 20 ns, which was enough time to obtain stable lateral dimensions for the system under study.[83] This stage gave, in the last 10 ns, a lipid surface area of 60.53 ± 0.82 Å^2 after subtracting 250 Å^2 as a gA surface area[61]. The purpose of this stage was to prepare a realistic lipid

environment for the peptide channel.

During the subsequent equilibrations, the restraints on the protein and the lipid phosphorus atoms were progressively reduced without significant changes in the system structure. These simulations in the NPAT ensemble (Equilibrations 4–10) utilized a tetragonal box having a lateral dimension of 38.22 Å. The lateral dimension (38.22 Å) was the final value after the end of the Equilibration 3 stage. Both the Equilibration 10 stage and the routine 10 ns production run (done in parallel with the umbrella sampling simulations) were performed with the protein center-of-mass (COM) as the only restraint. Considering that the lipid molecules immediately adjacent to the gA channel have different properties than those farther away from the channel due to protein-surface perturbations,[62] and that 16 lipids per leaflet has previously been shown to have sufficient bulk-like lipid surroundings for the gA dimer,[89] our final system has a reasonable size.

A second system was derived from the gA_{Mac} system, by replacing the MacKerell force field parameters[81] for tryptophan residues with version 31 of the CHARMM force field parameters, using the final frame of the Equilibration 9 stage structure for the Equilibration 10 stage. This system was denoted gA_{C31}.

Another system was derived from the gA_{C31}, replacing all Na^+ ions with K^+ ions, using the Equilibration 10 stage structure as the starting point. This system was used for PMF studies.

The gM system was derived from the gA system, replacing each tryptophan residue with a phenylalanine residue, and equilibrated in the same way as the gA_{Mac} system, using all of the preparation stages (Table 2.1).

2.2.3 MD Simulation Parameters and Analysis Details

Simulations were performed with NAMD software,[109] version 2.6, and using version 31 of the CHARMM force field.[12,110–114] Trajectory files were written every 1 ps for both the 10 ns test-ion-free production run and the umbrella sampling production runs using a time step of 2 fs and the NPAT ensemble. A smoothing function was applied to both the electrostatic and van der Waals forces at a distance of 8 Å with a switching cutoff distance of 12 Å, a pair list distance of 14 Å, and all bonds with hydrogen being rigid using the ShakeH algorithm. The non-bonded interactions

parameters (switching, spherical cutoff, and pair list distances) were carefully chosen to achieve realistic macromolecular simulations.[115] The Particle Mesh Ewald algorithm (PME) was used for electrostatic calculations with an interpolation function of order 5, and PME box grid size of 64, 64, 128 in *x*, *y*, and *z* direction, respectively. Langevin dynamics were used to maintain the temperature at 303.15 K with a damping coefficient of 5 ps^{-1}, whereas the pressure in the *z* direction was maintained at 1 atm using the Nosé–Hoover Langevin piston method with an oscillation of 1 ps and a damping time of 0.1 ps.[116,117]

All the analysis scripts were composed locally using both VMD and Tcl[118] commands. The deuterium order parameters of the deuterium-labeled segment were calculated from:[97,99,101,103]

$$S_{CD}^{(i)} = \frac{1}{2}\langle (3\cos^2\theta_i - 1)\rangle, \tag{2.2}$$

where θ_i is the angle between the *i*th C–H vector and the *z* axis (bilayer normal), and the angle brackets denote an average over both acyl chains from all lipid molecules, all C–H vectors associated with the *i*th carbon, and time. The deuterium order parameters have a range from −0.5 to 1.0 and reflect the lipid tails orientation (i.e., a −0.5 value represents fully ordered lipid tails, whereas a 1.0 value represents fully disordered lipid tails).

The root-mean-square displacement (RMSD) reflects the degree of similarity between three-dimensional protein structures. RMSD was computed by measuring the RMSD between equivalent atoms after optimal superposition of the two structures (the protein structure in trajectory frame *i* and the reference initial, equilibrated trajectory frame).

The conformational stability of the side-chains can be represented by their torsion angles (dihedral angles) such as χ_1 and χ_2 angles. For tryptophan and phenylalanine side-chains, the χ_1 angle is the counterclockwise rotation of the C_β–C_γ bond around the C_α–C_β bond in N–C_α–C_β–C_γ chain of atoms, whereas χ_2 angle is the counterclockwise rotation of the C_γ–C_{δ_1} bond around the C_β–C_γ bond in C_α–C_β–C_γ–C_{δ_1} chain of atoms.[119] This definition of torsion angles gives a positive torsion angle, whereas a negative torsion angle requires rotation in the opposite direction.

2.2.4 Umbrella Sampling Simulations

All the umbrella sampling simulations were performed using the final Equilibration 10 structure of the system under study as an initial structure. In these simulations, two umbrella-potential methods were used: 1) Relative Transport Coordinate (RTC), in which the protein COM is restrained to within 0.1 Å of the origin (k_f^{COM} = 1000 kcal/(mol·Å^2)) and the test ion, selected from the bath ions, in the *z* direction, is restrained relative to the protein COM (k_f^{RTC} = 15 kcal/(mol·Å^2)). 2) Independent Transport Coordinate (ITC), in which the protein COM is restrained to within 0.1 Å of the origin (k_f^{COM} = 1000 kcal/(mol·Å^2)) and the test ion, selected from the bath ions, is restrained to a plane normal to the *z* axis (k_f^{ITC} = 30 kcal/(mol·Å^2)). All k_f symbols designate force constants (i.e., harmonic spring constants).

The protein COM was strongly restrained to the origin to gain better convergence as deduced from earlier work.[86,87,89] Restraining the protein COM was achieved by applying a spherical restraint on the protein COM through the potential $\frac{1}{2}k_f^{COM}(r_{COM} - 0.1)^2$.

In the RTC method, the transport coordinate (traditionally called the reaction coordinate) was chosen to be the distance of the test ion relative to the protein COM in the *z* direction. An equal but opposite force [Eq. (2.4)] should be distributed over all the channel atoms; however, this was not implemented due to its negligible effect compared with the presence of the restraining force on the protein COM. In the ITC method, the transport coordinate was chosen to be the position of the test ion relative to the origin of the simulation box (0, 0, 0) in the *z* direction.

The restraining force on the protein COM is not a component of the transport coordinate in the ITC method, but rather a structural restraint designed to establish a reference point for the coordinate system, whereas it is in the RTC method. In both cases, RTC and ITC methods, the PMF is not expected to be affected by the structural restraining force[120] as long as the system is well equilibrated and the PMF is calculated with respect to the bulk.

The ITC approach has the advantages of being practically easier to implement in NAMD compared with the RTC method and producing the same results as the RTC method. We do not anticipate that the ITC approach would be affected by the presence of the restraining force on the protein COM,[120] which, in any case, is the same as in the RTC method.

During umbrella sampling with the test ion, a spherical restraint (k_f = 20 kcal/(mol·Å^2)) was applied on all other ions to keep them more than 14 Å away from the origin and a cylindrical restraint (k_f = 20 kcal/(mol·Å^2)) was applied on the test ion to keep it within 5 Å of the *z* axis. The purpose of the cylindrical restraint is to assure a bounded sampling region outside the channel for the test ion, whereas the purpose of the spherical restraint is to assure a one-ion PMF.[11,80,84]

We used 201 windows with a window width of 0.2 Å to cover the transport coordinate $-20 \leq z \leq 20$ Å. For each window, the *z* coordinate of the test ion was set to the window position and its *x* and *y* initial values were set to zero before performing minimization for 3000 steps, heating from 0 to 303.15 K, equilibration in the NPAT ensemble for 1 ns, and production in the NPAT ensemble for 1 ns. We used the weighted histogram analysis method (WHAM) to unbias the umbrella potential on the test ion and extract the PMF.[10] The code is available for free download from the web.[121] The mathematical details for calculating or extracting the PMF were discussed elsewhere.[10,80,122,123]

The decomposed potential of mean force (PMF_i) was calculated by integrating the *z* component of the mean force $\langle F_i(z_{ion})\rangle$ applied by the interesting group (*i*) on the test ion over the transport coordinate,[92]

$$PMF_i(z_w) \quad = \quad PMF_i(z_\circ) - \int_{z_\circ}^{z_w} \langle F_i(z_{ion})\rangle \, \mathrm{d}z_w, \tag{2.3}$$

where the $PMF_i(z_\circ)$ is an arbitrary reference value, generally assumed to be zero at $z_\circ$, z_w is the window-reference position, and $\langle F_i(z_{ion})\rangle$ is the average equilibrium force applied by group (*i*) on the test ion at window *w*. The force $F_i(z_{ion})$ was extracted via the pair-interaction-calculation method available in the NAMD software package. This method analyzes the available dynamic trajectory (ours was sampled every 1 ps for the ensemble average) and calculates the forces, vdW and electrostatic, from the second group, group (*i*), on the first group, the test ion.

The potential of mean restraint (PMR) was used as a test for the WHAM results. The PMR can

be extracted as follows:[120]

$$F^{\mathrm{RTC}}(z_{\mathrm{ion}}, z_{\mathrm{COM}}) = -\mathrm{k}_{\mathrm{f}}^{\mathrm{RTC}}(z_{\mathrm{ion}} - z_{\mathrm{COM}} - z_w), \tag{2.4}$$

$$F^{\mathrm{ITC}}(z_{\mathrm{ion}}) = -\mathrm{k}_{\mathrm{f}}^{\mathrm{ITC}}(z_{\mathrm{ion}} - z_w), \tag{2.5}$$

$$PMR^{\mathrm{RTC}}(z_w) = PMR^{RTC}(z_\circ) + \int_{z_\circ}^{z_w} \langle F^{\mathrm{RTC}}(z_{\mathrm{ion}}, z_{\mathrm{COM}}) \rangle \, \mathrm{d}z_w, \tag{2.6}$$

$$PMR^{\mathrm{ITC}}(z_w) = PMR^{ITC}(z_\circ) + \int_{z_\circ}^{z_w} \langle F^{\mathrm{ITC}}(z_{\mathrm{ion}}) \rangle \, \mathrm{d}z_w, \tag{2.7}$$

where z_{ion} is the test ion position in the z direction (sampled every 2 fs for the ensemble average), z_{COM} is the protein COM position in the z direction (sampled every 2 fs for the ensemble average), z_w is the window-reference position, $F^{\mathrm{RTC}}(z_{\mathrm{ion}}, z_{\mathrm{COM}})$ is the instantaneous restraint force applied in the z direction to the test ion under the RTC method, and $F^{\mathrm{ITC}}(z_{\mathrm{ion}})$ is the instantaneous restraint force applied in the z direction to the test ion under the ITC method. The symmetrization of our results was obtained by averaging the free-energy values at positive and negative values of the transport coordinate. The Composite Simpson's Rule was used as a numerical integration method.[124]

2.3 Results and Discussion

2.3.1 Preparation and Simulation Methods Stability

The preparation process successfully produced a stable and disordered system compared with the initial crystal-like structure [Fig. 2.2(a)]. On the basis of simulating two other gA systems (data not shown), which vary in the number of lipids molecules (i.e., one with 16 and the other one with 280 DMPC lipid molecules), we concluded that three-lipid shells surrounding the protein are required to provide the bulk lipid structural properties at the periodic boundaries.

The simulating annealing, based on the deuterium order parameters (Fig. 2.3), was sufficient to produce disordered lipid tails in gA_{Mac}, gA_{C31}, and gM systems. Our results agree excellently with both the experimental[125–127] and the simulation[103] results, except in the region close to the head group, where the order remains high in experiments,[125–127] but commonly declines in simulation.[103]

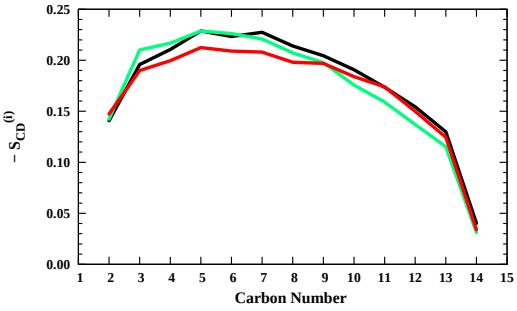

Figure 2.3: Deuterium order parameters for the DMPC tails in gA_{Mac} (black line), gA_{C31} (green line), and gM (red line) systems.

Our RMSD results show reasonable protein structural stability within the production run time scale except for slight excesses in the gA_{Mac} and gM systems after 5 ns (Fig. 2.4). The density profiles of those systems (data not shown) show a good distribution for all atoms. One contribution to the slight drifting in the RMSD is the mobility of the ethanolamine residues, which is higher in the gA_{Mac} and the gM systems than in the gA_{C31} system (Fig. 2.5).

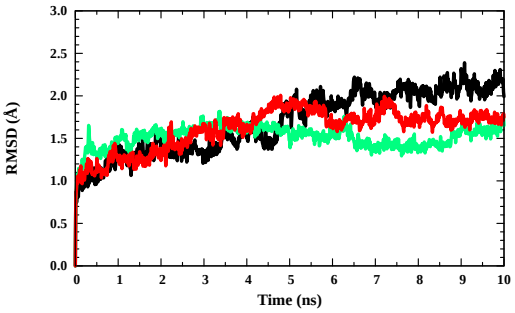

Figure 2.4: RMSD versus time for the protein in gA_{Mac} (black line), gA_{C31} (green line), and gM (red line) systems.

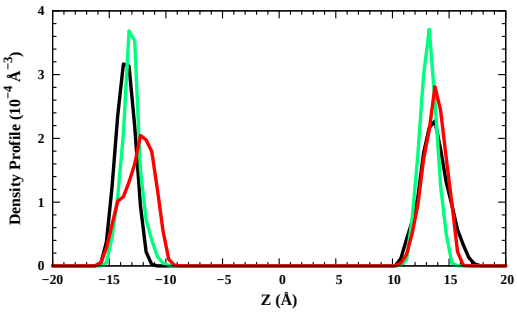

Figure 2.5: Density profile in the *z* direction for the oxygen atom of the ethanolamine residues in: gA_{Mac} (black line), gA_{C31} (green line), and gM (red line) systems.

Both χ_1 and χ_2 angles for the side-chain residues at positions 9, 11, 13, and 15 of the protein as a function of time are presented (Fig. 2.6).

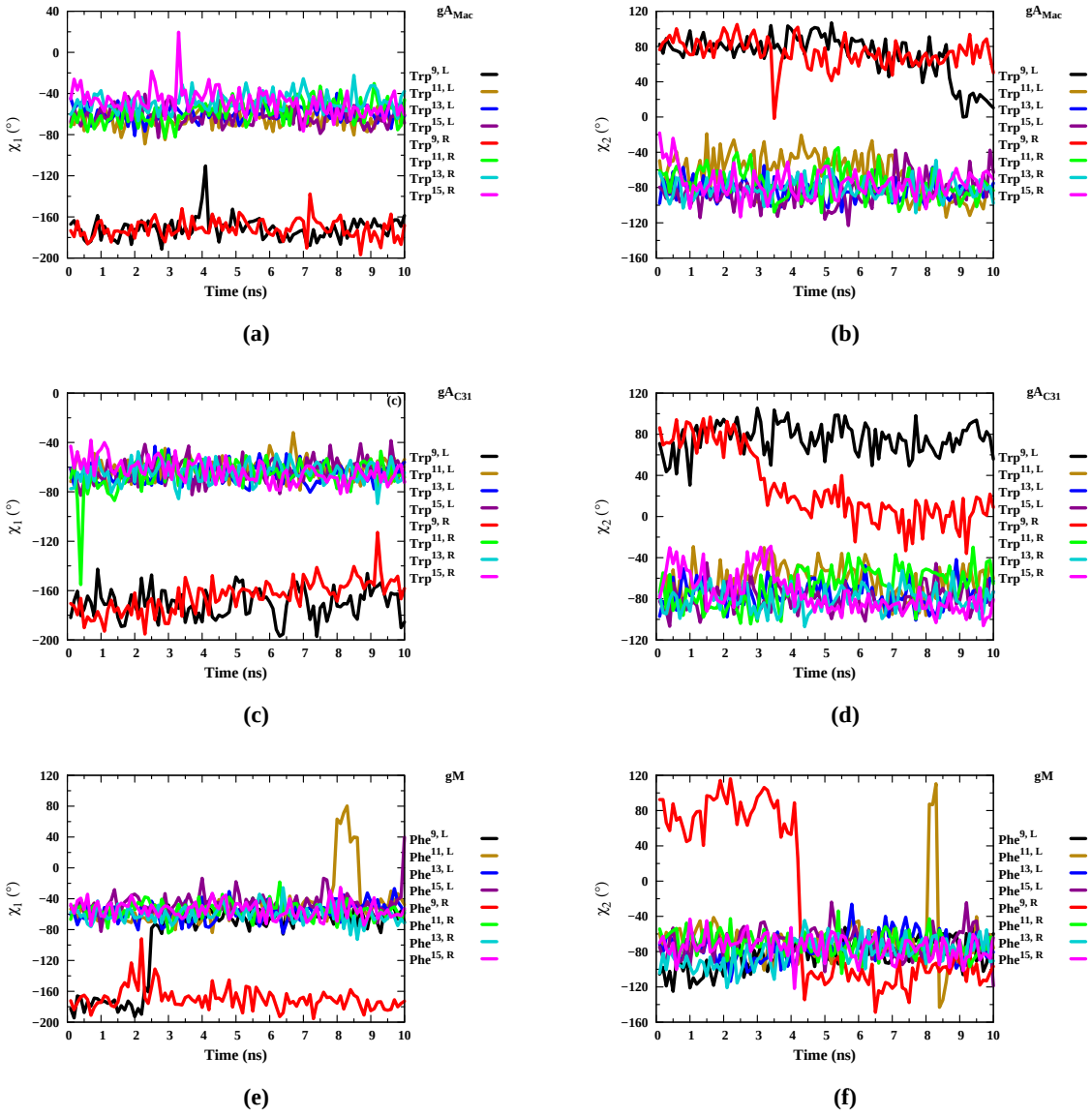

Figure 2.6: The torsion angles, χ_1 and χ_2, versus time for the side-chain residues during long production runs. The superscript notations on the side-chain residue abbreviation to the upper right of each plot represent the residue position and the protein monomer, respectively.

Trp^9 starts and mostly stays in a different rotameric state, and drifts a bit [Figs. 2.6(a–d)], compared with other positions, consistent with previously reported simulation results.[94] The reason for this difference is that all the tryptophan residues except Trp^9 are close to the membrane surface,

therefore, they have stronger interactions with the water molecules and the lipid head groups via hydrogen bonding, which stabilize them at their positions.[94]

On the basis of the Lovell et al. rotamer library nomenclature,[119] our results show that the Trp^{9} residues maintain the **t**90° rotamer state, whereas the $Trp^{11,13,15}$ residues maintain the **m**−90° rotamer state through the simulation time scale. Our results agree with those data extracted from the experimental results in sodium dodecyl sulfate micelles leading to the 1JNO structure,[8] but conflicts with the data extracted from those experiments in DMPC bilayers leading to the solid-state NMR results giving the 1MAG structure,[90] where Trp^{9} residues assumes the **m**−90° rotamer state. Based on the Lovell et al. database,[119] the most common rotamer state for tryptophan is **m**95° with 32% observations, whereas **t**90° and **m**−90° rotamer states were observed with 18% and 5%, respectively.

For the gA_{Mac} system, both χ_1 and χ_2 angles have reasonable and stable values throughout the production run time scale [Figs. 2.6(a) and (b)]. Clearly, the lipid head groups dramatically stabilize the side-chains because in vacuum their simulations show numerous rotamer changes on the ns time scale.[128] In the gA_{C31} system, except for some temporary fluctuations in χ_1 for $Trp^{11,R}$, and in χ_2 for $Trp^{9,R}$, the tryptophan side-chain positions are generally stable throughout the production run time scale [Figs. 2.6(c) and (d)], as is also true for the subsequent umbrella sampling runs.

Both χ_1 and χ_2 angles for phenylalanine residues on gM are shown in [Figs. 2.6(e) and (f)], respectively. Using the same nomenclature,[119] $Phe^{9,R}$ residue generally maintains the **t**80° rotamer state, whereas the rest of phenylalanine residues maintain the **m**−85° rotamer state through the simulation time scale. This is the first report of MD simulations of the gM channel allowing assessments of the conformational stability of the phenylalanine side-chains. They show good conformational stability on this time scale, with drifting of Phe^{9} residue in some cases and a temporary perturbation of $Phe^{11,L}$ residue in other cases. According to Lovell et al. database,[119] the common rotamer state for phenylalanine is **m**−85° with 44% observations, whereas **t**80° rotamer state was observed with 33%. The phenylalanine rotamer states in our gM simulations primarily reflect the initial conformations.

The conformational variants for the tryptophan and the phenylalanine side-chains in the gram-

icidin channels as well as the slight excesses of the RMSD for the gramicidin channels are not expected to produce much asymmetry or error in the Na^+ PMFs, because they do not occur in the umbrella sampling runs, which are generally similar to the first two ns of the production runs, except for minor fluctuations induced by the test ion.

2.3.2 Force Fields Comparison

How the two types of the force field and the side-chain residue species affect the shape and the amplitude of the Na^+ $PMF_{(side\,chains)}$ are shown [Fig. 2.7(a)]. As stated in the Methods section [Eq. (2.3)], the Na^+ $PMF_{(side\,chains)}$ is calculated from the z component of the mean force exerted by the side-chain on the test ion, starting with the β-carbon. The PMF_i profiles (Fig. 2.7) were calculated with respect to the reference $z = \pm 20$ Å. The CHARMM force field, version 31, produces a double-well shaped potential for phenylalanine with a minimum of -3.2 kcal/mol and for tryptophan with a minimum of -5.7 kcal/mol. In contrast, the new MacKerell force field[81] for tryptophan produces a bowl-shaped potential with a minimum of -7.1 kcal/mol.

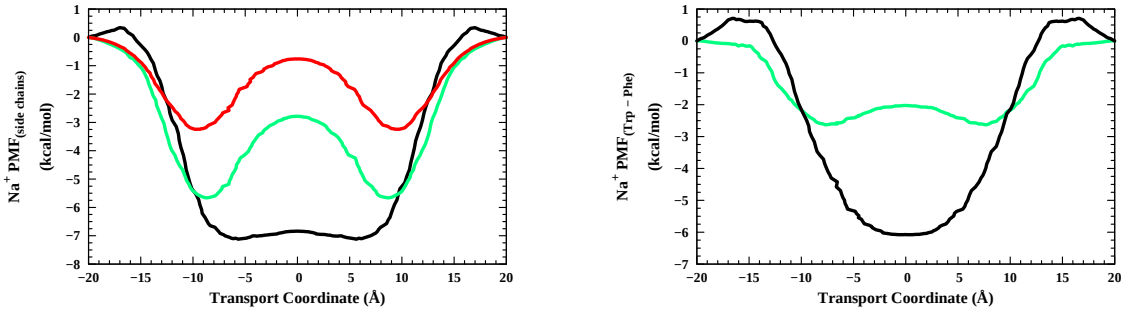

Figure 2.7: Symmetrized one-dimensional Na^+ PMF_i as a function of the transport coordinate from the force of the side-chains on the test ion. (*a*) The tryptophan effect is shown from both the MacKerell (black line) and version 31 of the CHARMM (green line) force fields, whereas the phenylalanine effect is shown from version 31 of the CHARMM force field (red line). (*b*) The tryptophan effect relative to the phenylalanine effect (after subtracting the phenylalanine profile from the tryptophan profiles) is shown for both the MacKerell (black line) and version 31 of the CHARMM (green line) force fields.

The MacKerell force field result for the free-energy difference (Na^+ PMF_{Trp} minus Na^+ PMF_{Phe}) [Fig. 2.7(b)], when compared to the experimentally derived gA-gM free-energy-difference profile,[78] has the same bowl-shape. The minimum in the computed side-chain PMF is -6.1 kcal/mol, within the simulation and experimental uncertainties, which is similar to the experimental minimum of ≈ -4.9 kcal/mol. Therefore, apparently, the MacKerell force field is superior to the CHARMM force field, version 31, in treating tryptophan electrostatic properties, producing a more accurately shaped, albeit somewhat deeper, profile.

Since the new tryptophan potential has a shape and minimum different from that of the older one, could we see the long-sought reduction in the Na^+ translocation barrier due to this change in the force field for the tryptophan residues? The answer to this question is discussed in the next section.

2.3.3 Force Fields Effects on the Na^+ PMF

The Na^+ PMF in gA_{Mac} and gA_{C31} systems is presented in [Fig. 2.8(a)]. Surprisingly, there is little difference between the two curves in spite of change in the force field. Both force fields produce HOSs at ± 9.1 Å in agreement with those at ± 9.2 Å extracted from ^{13}C chemical shift anisotropy experiments[79] and differ dramatically from previous simulation result[89] with regard to the absolute magnitude of the translocation barrier, ≈ 4 kcal/mol versus ≈ 15 kcal/mol.

One way to explore why changing the force field has no impact on the Na^+ PMF is by decomposing it into its components [Fig. 2.8(b)]. The PMF_i profiles [Fig. 2.8(b)] were calculated with respect to the reference $z = \pm 20$ Å. The choice of extracting the PMF_i with respect to this reference, $z = \pm 20$ Å, is based on the use in previous work of this reference. Even though our calculations with respect to the reference ($z = \pm 20$ Å) yielded flat (i.e., bulk-like) PMFs [Fig. 2.8(a)] at the symmetrical reference points, the component PMFs [Fig. 2.8(b)] were not flat at these symmetrical reference points. Therefore, the lack of flatness at the reference points may be expected to be in error here and in subsequent chapters, probably by a fixed amount related to the slope of the component PMF at the reference points. Nevertheless, comparisons of components for the two force fields, MacKerell and CHARMM force fields, are still appropriate because the two force fields are generally converged

near the references, and therefore the two component PMFs are subject to approximately the same offsets.

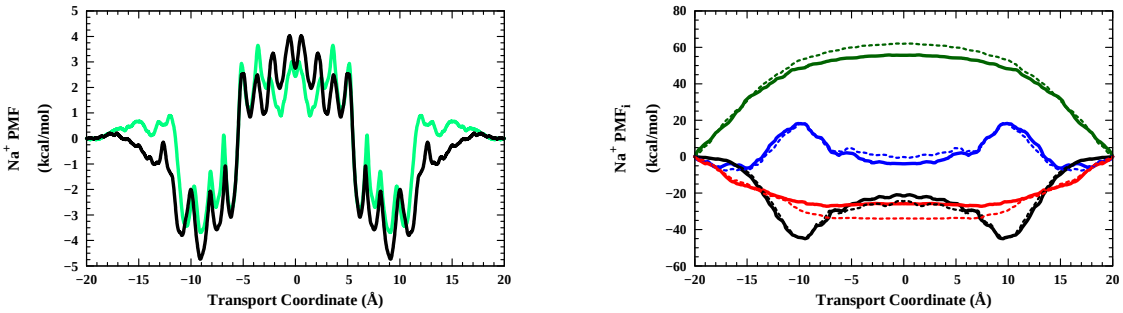

(a) **(b)**

Figure 2.8: Symmetrized one-dimensional Na^+ PMF and symmetrized one-dimensional Na^+ PMF_i as a function of the transport coordinate using the ITC method. (*a*) The Na^+ PMF is shown for both gA_{Mac} (black line) and gA_{C31} (green line) systems. (*b*) The Na^+ PMF_i for both gA_{Mac} (— line) and gA_{C31} (– – line) systems is shown from the force of ions (green), H_2O (blue), gA (black), and lipid molecules (red) on the test ion.

The Na^+ PMF_{Trp} most affects the larger components of the Na^+ PMF in the translocation region ($-12.5 \leq z \leq 12.5$ Å), but not in the expected ways. Rather than making the Na^+ PMF_{gA} a bowl-shaped potential, as one would expect from the direct electrostatic effect [Fig. 2.7(b)], the MacKerell force field causes the ion–protein interaction to be less favorable throughout the translocation region. From this, it is clear that effects of the tryptophan side-chains on the ion, mediated by the protein backbone or other side-chains, must have more impact than the direct electrostatic effects. We will refer to this phenomenon as an *indirect* effect, that is, an effect of the modified force field on the free-energy profile mediated by induced changes in the positions or dynamics of other atoms in the system. Other indirect effects, mediated by the lipids, the other ions, and the water molecules, are also remarkably large. Ultimately, there is a complete compensation between two groups, the Na^+ PMF_{gA} and Na^+ PMF_{lipids} versus the Na^+ PMF_{H_2O} and Na^+ PMF_{ions}. Under the MacKerell force field, the first group has a higher Na^+ PMF_i than with the CHARMM force field, version 31, within the channel region, $-12.5 \leq z \leq 12.5$ Å, whereas the second group has a lower one. This behavior

is consistent with and explains previous MD simulations showing that the gA channel structurally responds to external perturbations such as an ion in the pore.[80,92]

For completeness, we show the Na^+ PMF in the gM system (Fig. 2.9). The phenylalanine residues have small partial charges compared with tryptophan residues in the empirical force field, which should give a Na^+ PMF with a higher central-translocation barrier in the gM system compared with that in the gA_{C31} system. This prediction is supported by the results of the kinetic analysis of the homo- and heterodimer conductance data,[78] which indicate that the translocation step is ≈ 100-fold faster in gA than in gM. It is also supported by the side-chain PMFs from our simulations, which show the Na^+ PMF_{Phe} with a higher maximum-energy compared with that of Na^+ PMF_{Trp} [Fig. 2.7(a)]. However, the Na^+ PMF has net translocation free-energy barriers of 6.7 and 8.7 kcal/mol for gA_{C31} and gA_{Mac} [Fig. 2.8(a)], respectively, which are higher than the net translocation free-energy barrier of 5.7 kcal/mol for gM (Fig. 2.9), rather than a broad peak, exceeding that in gA by 2.0-3.0 kcal/mol at the center of the channel as envisioned in the kinetic analysis of heterodimers[78] and perturbations of gM function[129]. We suppose that the difference between our results and the experimental prediction reflects inaccuracies in the force fields like those suggested by the results presented above for tryptophan side-chains.

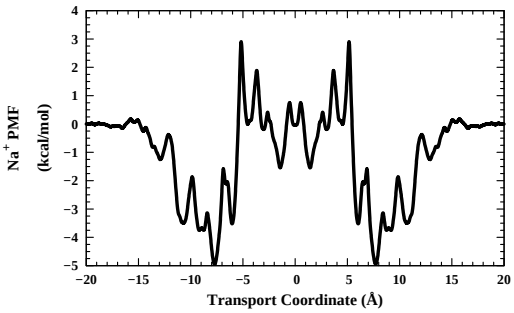

Figure 2.9: Symmetrized one-dimensional Na^+ PMF as a function of the transport coordinate using the ITC method in gM system.

Why then do we have a much lower translocation-energy barrier for the gA channel [Fig. 2.8(a)] compared with prior results,[82,89] even before any long-range-electrostatic corrections[11,80,84] and with a non-polarizable force field? If changing the force field for the tryptophan residues has no effect on the Na^+ PMF, what could be the reason for this acceptably low-translocation barrier? To answer this question we first reproduced the K^+ PMF results, because of extensive work that has

been done using that cation, searching for a possible explanation for this result. The next section shows that it was the inclusion of the CMAP algorithm in the CHARMM force field, version 31 that reduced the central-barrier height.

2.3.4 CMAP Impact and Umbrella Potential Methods Effect

The K^+ PMF using the CHARMM force field, version 31, with and without the CMAP algorithm is shown in [Fig. 2.10(a)]. In the former case, simulations were carried out with two different umbrella-potential methods. The K^+ PMF without the use of the CMAP algorithm (red curve) is similar to other previously reported K^+ PMFs[80,83,84,88,89], demonstrating that previous computations are reproducible. Again, with K^+ ions, the PMF with the use of the CMAP algorithm has a dramatically reduced central energy barrier and more negative HOS free-energies. We also compared these results to those obtained with the PMR method [Eq. (2.6)], which match qualitatively and quantitatively to within statistical errors.

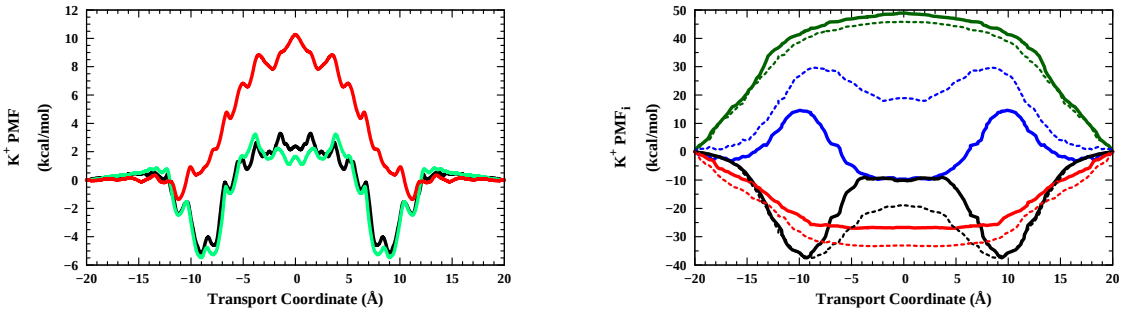

(a) **(b)**

Figure 2.10: One-dimensional K^+ PMF and one-dimensional K^+ PMF_i as a function of the transport coordinate. (*a*) The symmetrized K^+ PMF is shown from RTC without CMAP (red line), RTC with CMAP (green line), and ITC with CMAP (black line) implementations. (*b*) The K^+ PMF_i for both RTC with CMAP (— line) and RTC without CMAP (– – line) implementations is shown from the force of ions (green), H_2O (blue), gA (black), and lipid molecules (red) on the test ion.

The RTC method, both with and without the CMAP algorithm, shows excellent convergence. That is, PMFs based on increasingly complete fractions of the umbrella sampling trajectory (0.25, 0.5, 0.75, and 1.0 ns) converged to within 0.5 kcal/mol over the entire extent of the integration,

and to within 0.5 kcal/mol of the reference energy (0 kcal/mol at $z = -20$ Å) at the opposite z position ($z = 20$ Å). The non-symmetrized PMFs suggest that the energy uncertainty due to structural variations is on the order of ≈ 1 kcal/mol.

Further tests are desirable to understand why CMAP lowers the energy barrier and whether symmetrization for chirality would further modify the free-energy profile for gramicidin cation transport. In this paper, we illustrate the breadth of the issue by decomposing the K^+ PMF, obtained with the current version of CMAP, into four major components, K^+ PMF_i [Eq. (2.3)], where i denotes the mean force applied on the test ion by the other ions, the water, the peptide, or the lipid. We compare the component K^+ PMFs, K^+ PMF_i, from our simulations in the presence and in the absence of the CMAP algorithm using the RTC method [Fig. 2.10(b)]. The PMF_i profiles [Fig. 2.10(b)] were calculated with respect to the reference $z = \pm 20$ Å.

The direct effect of the CMAP algorithm, seen in K^+ PMF_{gA}, raises the translocation barrier by 8.8 kcal/mol. With the CMAP algorithm, the K^+ PMF_{H_2O} is lower in energy than without. This means that there is a stronger attraction between water molecules and the test ion in the channel when using the CMAP algorithm. This may indicate the water molecules inside the channel can more easily flip to aid in solvating the test ion when using the CMAP algorithm. Apparently, CMAP affects the peptide motions or structure, or water interaction in a way that facilitates the stabilization of the test ion by the single-file waters, and allows a decrease in mean force they exert on the ion as it translates through the channel. We suggest that this may be a crucial aspect of solving the high translocation barrier problem, and suspect that it will persist with chirality symmetrization of the CMAP corrections, which hopefully will provide further improvements in the backbone structure.

In the CMAP calculations,[12] backbone torsion energies were taken from quantum mechanical predictions for alanine, glycine, and proline with empirical corrections needed for alanine and glycine. Perhaps the generalization of the corrected L-alanine parameters to both L- and D- stereoisomers of Leu, Val, and to L-Trp in gA, could cause misleading results. However, we expect that this would not be a major problem and that our results would be qualitatively correct. Also, we note that CMAP was refined based on the protein folding problem,[12] but was not tested for other problems like ion transport through membrane channels.

The ITC method produces results essentially identical to the RTC method [Fig. 2.10(a)], including the quality of convergence. Because ITC is easier to apply under some circumstances, we will use the two methods interchangeably in this and subsequent chapters.

Future work will be required to balance force field issues (direct and indirect, including polarizability) and to assess whether channel conductance estimated from simulations accurately predicts the full range of measurements now available for this model system.

2.4 Conclusions

The results indicate that the original CHARMM force field, version 31, for tryptophan differs from that predicted by data-fitting, being double-well shaped potential, and that the MacKerell force field is consistent with data-fitting, being bowl-shaped potential and ≈ -6.1 kcal/mol deep at the center of the channel. However, the benefit of the improved partial charges is completely ablated by indirect effects, apparently a victim of small differences of large components judging from the decomposition, so the Na^+ PMF for gA does not differ appreciably from that for gM and does not predict the observed differences in current-voltage-concentration relationships between these two channels.

The CMAP algorithm lowers the translocation energy barrier to a reasonable level in the upgraded CHARMM force field, version 31. However, the PMF for gM channels does not have the higher translocation barrier expected from experimental studies.

Both represent examples of indirect effects (i.e., consequences of the force field mediated by "innocent bystander" molecules). Again, indirect effects of force field changes, especially those mediated by channel water molecules, were shown to be complex and unpredictable.

Chapter 3

A Gramicidin Entryway Sulfonate Inhibits Translocation

3.1 Background

Taurine gramicidin A (TgA) channel[32] [Fig. 3.1(a)] is an analog of gA channel [Fig. 3.1(b)] for which the ethanolamine residue at the C-terminus, which lies nearest to the lipid-water interface at each end of the channel, is replaced with taurine (i.e., the hydroxyl group of the C-terminus is replaced with the sulfonate group).

In previous TgA channel studies, the single-channel conductance for the TgA channel in 0.1–1.0 mol/kg KCl was found to be higher than that for the gA channel.[32] The higher single-channel conductance in TgA channel compared with that in gA channel was consistent with other experimental studies.[50,130–133] That is, the presence of a negatively charged group at the entrance of analogs of the gA channel caused an increase in the cation transport rate at low ionic concentration ($<$ 1.0 mol/kg).[50,130–133] The high single-channel behavior was explained as a result of an electro-

static effect of the fixed negative charges localized near the entrance of the channel.[130] Nevertheless, at higher ionic concentrations ($\geq$ 1.0 mol/kg), there is insignificant difference between the gA and its analogs single-channel conductance.

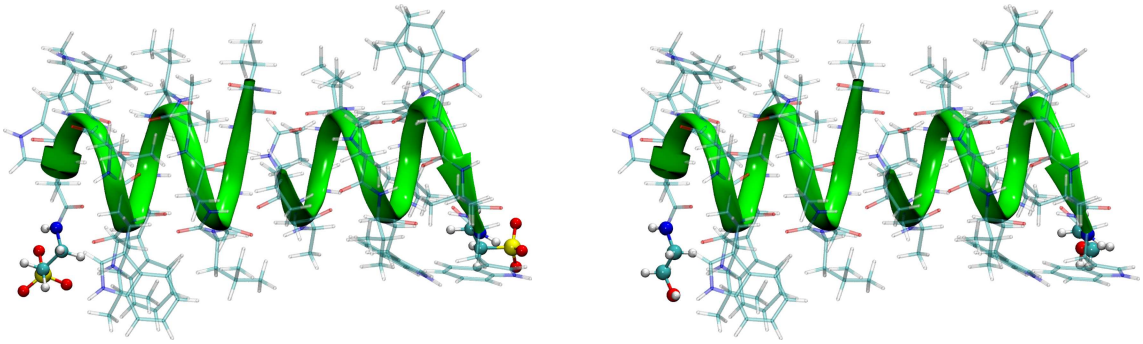

(a) **(b)**

Figure 3.1: Snapshots for (*a*) TgA and (*b*) gA channels. Both proteins are drawn using the New Cartoon drawing method (with a green color) to represent the right-handed β-helices, and using the Licorice drawing method to show all atoms. Both taurine and ethanolamine residues are drawn using the CPK drawing method. The colored species represent: C (cyan), H (white), O (red), S (yellow), and N (blue).

Intuitively, the negatively charged sulfonate group at the entrance of the channel is expected to attract the cations in the bath towards the vicinity of the channel entrance (i.e., the affinity of the channel for permeant cations, such as Na^+, is enhanced). But it is not clear whether the net effect of tighter binding would be to reduce or enhance the translocation-energy barrier between HOSs and the corresponding internal resistance of the channel. Also, why do TgA and gA channels not differ appreciably in conductance at this the higher concentration?

Here, we compare the one-dimensional free-energy profile for cation transport through the gA and TgA channels, extracted from umbrella-sampling simulations, to explore these specific questions and with the more general goal of illuminating the roles of negatively charged side-chains in other ion channels such as the voltage-gated calcium and sodium channels with their polyvalent selectivity-filters.[20,21,134–136]

3.2 Methods

3.2.1 Model System and Parameters

The initial gA system is the same system as what was denoted gA_{C31} in Chapter 2. The initial TgA system was modeled in the same way as the gA system except for the taurine residue. Because the only difference between the TgA dimer and the gA dimer is the C-terminal sulfonate residue, the two ethanolamine residues ($NHCH_2CH_2$–OH) in the 1JNO dimer structure were replaced with taurine ($NHCH_2CH_2$–SO_3^-) to produce the TgA dimer. The taurine residue was split into two parts: the $NHCH_2$ group and the $CH_2SO_3^-$ group. The first part was assigned the same parameters as the glycine residue, whereas the methylsulfonate parameters were obtained using the Extensible Computational Chemistry Environment (ECCE)[137] after performing quantum mechanics calculations using NWChem[138,139]. A ($CH_3CONHCH_2$–$CH_2SO_3^-$) molecule was built in ECCE and geometrically optimized at the RHF level of theory with the 6-311++G(3df,3pd) basis set, with Pople(3df,3pd) as a polarization function, and with Pople-style as a diffusion function. The bond lengths for methyl sulfonate and its connections in the taurine residue were derived from the resulting structure. The atomic partial charges were derived using electrostatic potential fitting while constraining the two hydrogens in the $CH_2SO_3^-$ group and all atoms in the $CH_3CONHCH_2CH_2$ group with the atomic partial charges from the empirical force field. The taurine parameters are listed (Table 3.1). To produce electroneutrality for the TgA system, two Cl^- ions were removed.

Table 3.1: Taurine Parameters

Stretching	Elements	Energy constant (K_b) [a] (kcal/(mol·Å^2))	Bond length (Å)	
	C–S	198.0	1.789	
	S–O	540.0	1.429	
Bending	Elements	Energy constant (K_θ) [a] (kcal/(mol·rad^2))	Bond angle (°)	
	C–C–S	58.0	112.231	
	H–C–S	46.0	106.872	
	C–S–O	85.0	104.331	
	O–S–O	130.0	114.085	
Torsional	Elements	Energy constant (K_χ) [a] (kcal/mol)	Multiplicity [a]	δ [a] (°)
	C–C–S–O	0.86	3	0.0
	H–C–S–O	0.16	3	0.0
Electrostatic	Elements	Atom type [a]	Partial charge	
	N	NH1	−0.47	
	H	H	0.31	
	C	CT2	−0.02	
	H	HA	0.09	
	H	HA	0.09	
	C	CT2	−0.428484	
	H	HA	0.09	
	H	HA	0.09	
	S	SL	1.926253	
	O	O2L	−0.892590	
	O	O2L	−0.892590	
	O	O2L	−0.892590	

[a]Extracted from version 31 of the CHARMM force field

3.2.2 System Preparation and Simulation Parameters

We applied the same detailed preparation steps and all simulation parameters as mentioned in Sections 2.2.2–2.2.4. Briefly, we mention the differences between the two approaches.

Equilibration 3 stage gave, in the last 10 ns, a lipid surface area of 60.5 ± 0.8 Å^2 and 60.4 ± 1.0 Å^2 in the gA and TgA systems, respectively, after subtracting 250 Å^2 as a gA surface area,[61] which we did on the reasonable assumption that the C-terminus replacement has negligible

effect on the TgA surface area compared to gA surface area. The simulations in the NPAT ensemble (Equilibrations 4–10) utilized a tetragonal box having a lateral dimension of 38.2 Å for both the gA and TgA systems, the final value after the Equilibration 3 stage.

The similarity of the values obtained independently for the two systems demonstrates the robustness of the equilibration procedure and the stability of the lipid-peptide-electrolyte structures after electrolyte homogenization and lipid melting.

In the umbrella sampling simulations, the ITC method was used to define the transport coordinate for both systems.

3.3 Results and Discussion

3.3.1 Preparation and Simulation Methods Stability

The RMSD results show reasonable protein stability throughout the 10 ns production run time scale in both the TgA and gA systems (Fig. 3.2).

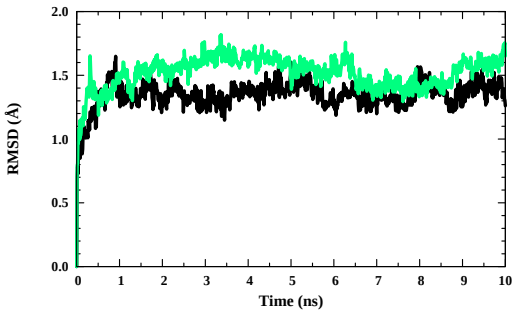

Figure 3.2: RMSD versus time for the protein in TgA (black line) and gA (green line) systems.

There is reasonable head group stability, demonstrated by the averaged *z*-positions of the lipid-phosphorus atoms during the production run, in both the TgA and gA systems [Figs. 3.3(a) and (b)]. The C-terminus stability in the TgA system is demonstrated by the *z*-positions of the taurine-

sulfur atoms [Fig. 3.3(a)], whereas the C-terminus stability in the gA system is demonstrated by the *z*-positions of the ethanolamine-oxygen atoms [Figs. 3.3(b)].

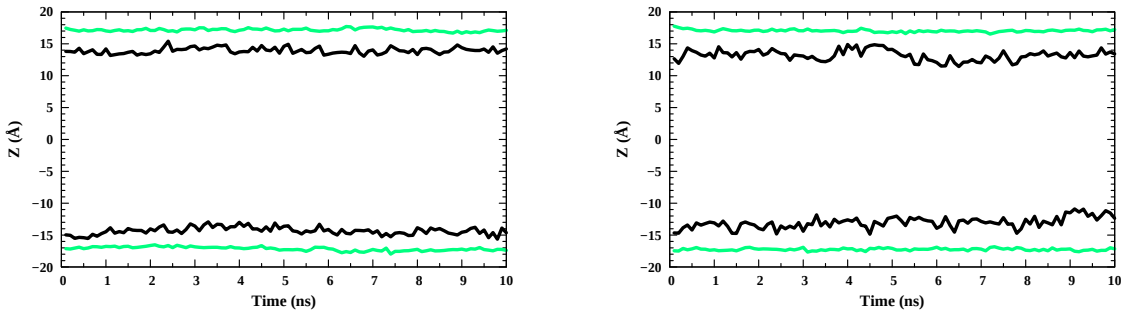

Figure 3.3: (a) Averaged *z*-positions of the lipid-phosphorus atoms (green line) and the *z*-positions of the taurine-sulfur atoms (black line) through the simulation time scale in the TgA system. (b) Averaged *z*-positions of the lipid-phosphorus atoms (green line) and the *z*-positions of the ethanolamine-oxygen atoms (black line) through the simulation time scale in the gA system.

The effect of the taurine terminal compared with that of the ethanolamine terminal is shown by the molality profile in the *z* direction (Fig. 3.4). Ignoring the high occupancy at ($9 \leq z \leq 11$ Å), there is a higher Na^+ ion occupancy near the mouth of the TgA channel ($12 \leq |z| \leq 22$ Å) compared with that of the gA channel. The high occupancy at ($9 \leq z \leq 11$ Å) in the long simulation was spontaneous, the channel having started empty, and that it was not the case for the umbrella sampling runs, which started and ended with no occupancy of the HOSs by mobile cations.

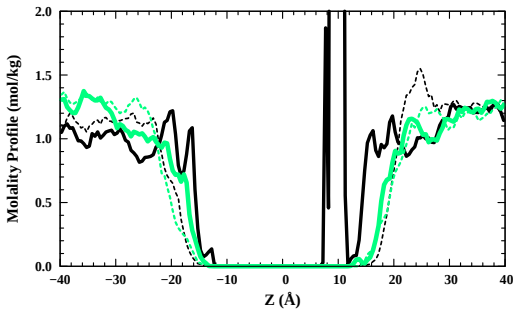

Figure 3.4: Molality profile in the *z* direction for Na^+ (— line) and Cl^- (– – line) ions in both the TgA (black line) and the gA (green line) systems.

Because of the interaction between the taurine terminals and the Na^+ ions near the mouth of the channel, could we see a deepening of the HOS energy well and a reduction in the Na^+ PMF translocation barrier in the TgA system compared with that in the gA system due to electrostatic attraction? The answer to this question is discussed in the next section.

3.3.2 Terminal Effects on the Na^+ PMF

The Na^+ PMF in the TgA and the gA systems is shown (Fig. 3.5). Generally, the Na^+ PMF in the TgA system is lower than that in the gA system except at the central-channel region ($-4 \leq z \leq 4$ Å), where it is higher. The TgA channel has HOSs at ± 10.5 Å with HOS well depth of -3.0 kcal/mol and a central-barrier height of 3.5 kcal/mol, whereas the gA channel has HOSs at ± 9.1 Å with HOS well depth of -1.9 kcal/mol and a central-barrier height of 1.2 kcal/mol. The low central barrier for the gA system is a product of introducing the CMAP algorithm in our simulations, as discussed previously in Section 2.3.4.

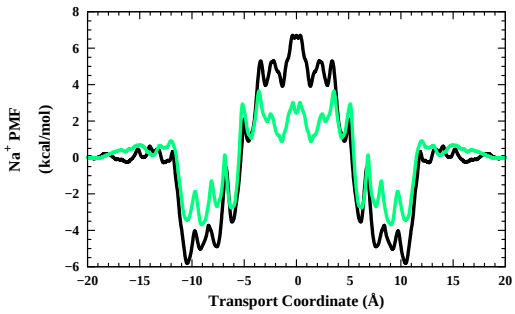

Figure 3.5: The symmetrized one-dimensional Na^+ PMF as a function of the transport coordinate for both the TgA (black line) and the gA (green line) systems.

Indeed, the HOSs are deeper in the TgA system compared with that in the gA system, but the central-barrier height is higher. The higher central-energy barrier in the TgA means a lower single-channel conductance would be anticipated in the TgA channel compared with that in the gA channel in disagreement with experimental studies[32,50,130–133], unless compensated by other factors, such as

increased entry rate due to electrostatic attraction to the channel entry.

Convergence, determined from increasingly complete data sets, symmetry in the free-energy profile, accuracy judged from the proximity of the free-energy integral endpoint to the reference potential on the opposite side of the bilayer, and methodological independence judged from comparison of the WHAM method to the PMR method [Eq. (2.7)], were all excellent, yielding uncertainties of ≈ 1 kcal/mol.

One way to explore why replacing the terminal ethanolamine residues with the taurine residues increases the energy of the Na^+ PMF at the center of the channel is by decomposing it into its components, Na^+ PMF_i [Eq. (2.3)]. First, we show the channel C-terminus components of the two peptides (Fig. 3.6), that is, the PMF of the SO_3^- group from TgA on the test ion (black line) in comparison to the PMF of the OH group from gA on the test ion (green line).

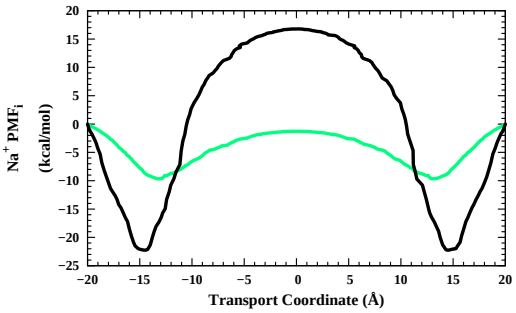

Figure 3.6: Symmetrized one-dimensional Na^+ PMF_i as a function of the transport coordinate. The SO_3^- group effect (black line) relative to the OH group effect (green line) on the Na^+ ion.

A stronger attraction of Na^+ for the SO_3^- group than for the OH group is shown by deeper global minima (Fig. 3.6). The central-energy barrier for $PMF_{SO_3^-}$ is quite striking, even exceeding zero, but upon reflection one can see that this should not be possible. The $PMF_{SO_3^-}$ should be similar to the dynamic average electrostatic potential energy for the test ion passing along an axis equidistant from the two SO_3^- groups (except for entropic and off-axis effects), which could not

exceed zero. Examination of the slope at the reference points, $z = \pm 20$ Å, as mentioned in Section 2.3.3, explains the problem. There would still be considerable work required to move the test particle towards infinity from the left-hand side. We did not carry out test ion sampling of more distant regions, but we expect that the curve would rise monotonically to a plateau on the left and right sides. The same case is true for the gA system, but to a lesser extent. Therefore, we only use this figure to illustrate that the central-energy barrier for the TgA system would be expected to be higher than for the gA system.

To further illuminate the sources of difference between the PMF for the gA system and for the TgA system, we next examine some of the important factors that contribute to the differences between the PMFs for the TgA and gA systems. As stated in Chapter 2, indirect effects of force field changes can be complex and the compensation among the major system components in producing the total PMF can be unpredictable. There in Chapter 2, we defined the indirect effect as an effect of the modified force field on the free-energy profile mediated by induced changes in the positions or dynamics of other atoms in the system. For instance, changes in the peptide torsion angle parameterization strongly affect ion–water interactions.

We illustrate the same principle here, focusing on two of the four major components of the system, the protein and the water (Fig. 3.7).

There is a higher central-barrier height for the Na^+ PMF_{TgA}, as well as deeper HOSs well depth and shifted HOSs compared with those in Na^+ PMF_{gA} (Fig. 3.7). Furthermore, comparing water contributions for the two systems (Fig. 3.7, dashed lines), the Na^+ PMF_{H_2O} has higher values outside the channel region. The high Na^+ PMF_{H_2O}

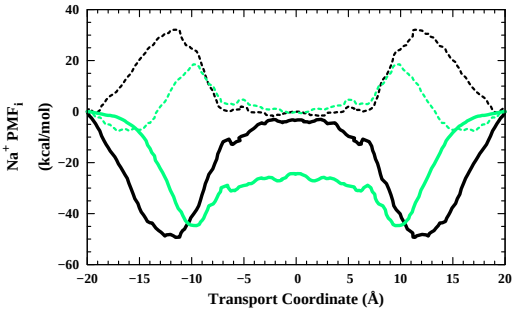

Figure 3.7: Symmetrized one-dimensional Na^+ PMF_i as a function of the transport coordinate. The Na^+ PMF_i for both TgA (black line) and gA (green line) systems is shown from the force of H_2O (– – line) and protein (— line) on the test ion.

barrier beyond $z = \pm 10$ Å counteracts or partially screens the effect of the SO_3^- group. The screening effect of water molecules is more dominant in the TgA system than in the gA system. The dominant screening effect in the TgA system may, in part, be the result of using the spherical restraint that excludes cations from a sphere of radius 14 Å where the channel is in the center of this sphere. If cations were allowed to approach the SO_3^- more closely, they would have moderated this water reaction.

These two examples demonstrate the complexity of indirect effects and show that it is difficult to predict the free-energy barriers to transport from intuition based on electrostatics. Therefore, the final height of the central-energy barrier of Na^+ PMF in the TgA system (Fig. 3.5) may be influenced by the indirect water, protein, or lipid effects induced by introducing the CMAP algorithm, the lack of the polarizability effect in our simulations,[11,85,86,89,92] or other unintended consequences of empirical force field parameters or applied restraints.

To elaborate a bit further on the second point, the high central-energy barrier in the PMF for the TgA system compared with that in the gA system (Fig. 3.5) might be exaggerated from applying the 1-ion PMF condition (i.e., applying the spherical restraint). That is, the spherical restraint excludes cations from a sphere of radius 14 Å where the channel is in the center of this sphere. No cations are allowed to approach the channel prevents the natural phenomenon where the cations screen the negatively charged group. Hence, when using the spherical restraint, alleviating the influence of the negatively charged group (SO_3^- group) is only achieved by orientation of water molecules with the water hydrogen atoms pointing towards the SO_3^- group. Consequently, part of the water molecules inside the TgA channel points to one direction, whereas the other part points to the other direction. The water orientation inside the TgA channel may therefore have difficulty flipping during the cation passage. The flipping difficulty of water molecules inside the TgA channel could enhance the internal resistance, reflected in the increased height of the central-energy barrier.

As an interesting side issue, we also explored the behavior of water both inside and outside the channel by showing its orientation, averaged for all waters located within 0.5 Å thick slabs parallel to the bilayer in each umbrella sampling window, as a function of transport coordinate [Figs. 3.8(a) and (b)]. The angle θ is the angle between the product of the two O–H vectors and the z axis.

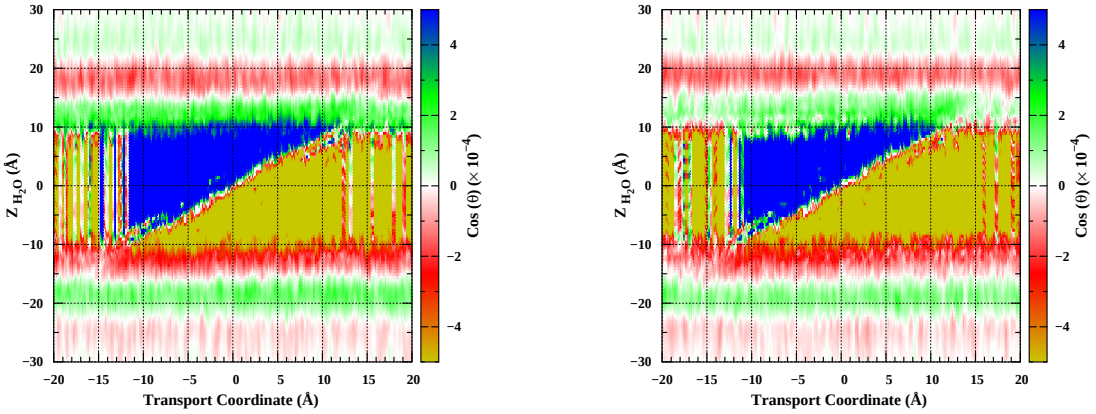

Figure 3.8: Normalized water orientation as a function of the transport coordinate and the *z* axis of a particular window frame for both (a) the TgA and (b) the gA systems.

There is a layering of external water molecules in the *z* direction with the innermost layer being slightly more intense in the TgA system [Fig. 3.8(a)] than that in the gA system [Fig. 3.8(b)] as a result of replacing the hydroxyl group with the sulfonate group. Such oscillations are reminiscent of large oscillations in water density observed in simulations within 1 nm of a rigid surface,[140] and may play a role in the decay in dielectric coefficient observed as an atomic force microscope tip gets within ≈ 10 nm of a mica surface.[141]

Since the locations of the SO_3^- groups are around $z = \pm 15$ Å, the majority of water molecules in the first layer around $z = \pm 15$ Å are oriented with the hydrogens pointing toward the SO_3^- group. Therefore, the SO_3^- groups in the TgA channel are well surrounded with two oppositely oriented water molecules, whereas the OH groups in the gA channel are surrounded with oriented water molecules in one direction. (Of course, this effect is somewhat muted by averaging with waters in the head group region, which are similarly oriented for both systems). The difference in water orientation probably contributes to the difference in water contributions to the TgA and gA cation

transport PMFs. The oscillations in water structure persist clear out to $z > 20$ Å [Figs. 3.8(a) and (b)], even though the lipid and water molecules and, in the case of the gA system, the ion channel are net neutral in charge.

In future studies, it may be interesting to consider the possible effects of this structured water on membrane functions, such as ion transport. In particular, although the layering doesn't appear to affect the cation transport free-energy profile near the channel entrance (Fig. 3.5), structured water near the membrane surface may play a role in the interesting phenomenon of lateral diffusion by protons observed with biological membranes.[142–144]

3.4 Conclusions

The presence of the negatively charged taurine residues instead of the electroneutral ethanolamine residues at the entrance of the gA channel affects both the depth and the location of the HOSs producing a strong attraction for the cations in the bulk.

The direct and indirect effects of changing the C-terminus on the test ion are interwoven in a complicated way and respond in complex ways to changes in force field to produce the PMF, in which the translocation barrier is enhanced rather than diminished, such that the intra-channel resistance would be increased by the presence of the charges, as expected from the experimentally observed enhancement in single channel cation conductance.

The potential of mean force by the sulfonate on the test ion is highly modulated by indirect effects, but the increased resistance survives. Revisions in parametrization that take indirect effects into account may be necessary to provide agreement with experimental results.

The high central free-energy barrier in the TgA system compared with that in the gA system might be partly a result of the spherical restraint. The presence of the spherical restraint might cause a flipping difficulty for water molecules inside the TgA channel, which in turn enhances the internal resistance (i.e., produces a higher central free-energy barrier).

Chapter 4

M_2-TMD Channel Structure and Conductance Mechanism

4.1 Background

The influenza A virus is a genus of the orthomyxovirus family of viruses. It is coated by a cell membrane containing several copies of three integral membrane proteins: a receptor-cleavage protein known as neuraminidase, a fusion protein known as hemagglutinin, and a proton channel known as an M_2 channel.[145,146] After the endocytosis process of the virus in an epithelial cell of a host, the engulfed virus appears in an endosome, which has a low pH environment with a pH range of 4.9–5.2.[147] At this low pH, the M_2 channel assumes an active form that allows protons to pass through it to acidify the matrix of the virus prior to the fusion of the virion membrane with the endosomal membrane.[33,37,39,40,148] This acidification facilitates the uncoating process, which allows a release of the viral genome. Amantadine (1-Aminoadamantane hydrochloride) has an antiviral activity for this type of viruses at low concentrations ($\leq 5\ \mu$M).[33,36–38,149–154] It blocks the M_2 channel and

disallows it from passing protons to the virion interior.[33,36,37,40,152,154–159] Previous experimental data indicate that the M_2 protein is an essential part in virus replication and assembly.[145,151,160–164]

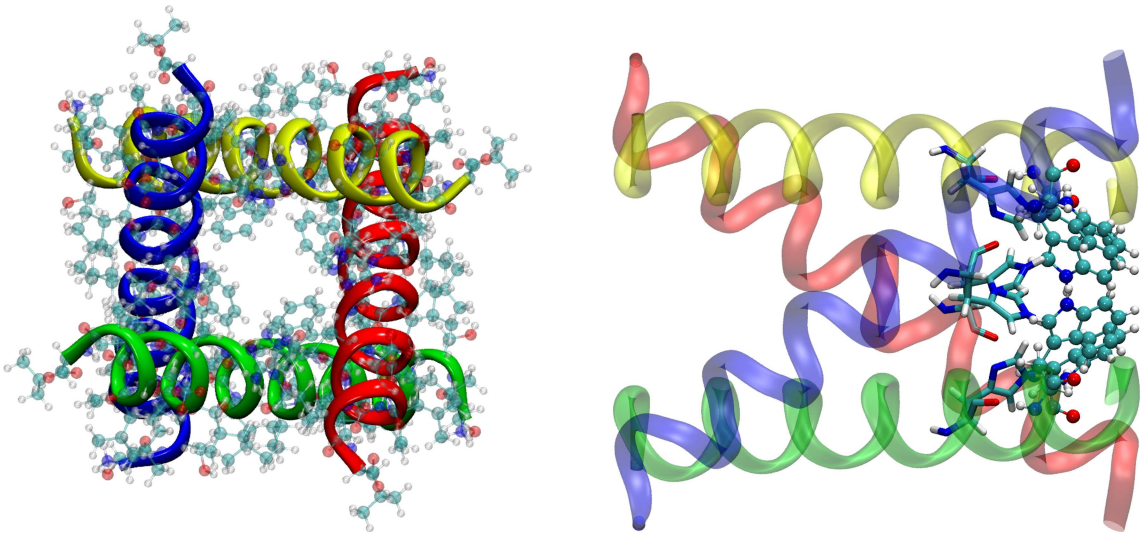

(a) **(b)**

Figure 4.1: M_2-TMD Channel Snapshots: (*a*) A view from the C-terminus end shows the protein atoms drawn using the CPK drawing method. (*b*) a side view shows the His^{37} residues, drawn using the Licorice drawing method, and Trp^{41} residues, drawn using the CPK drawing method. In both snapshots, the New Cartoon drawing method is used to represent the four α-helices: A (red), B (green), C (blue), and D (yellow).

The M_2 protein is comprised of four identical monomers,[148,160,165–168] each consisting of 97 amino acids.[146] Each monomer consists of three domains: an extracellular N-terminal domain of 18 to 23 amino acid residues, an intracellular C-terminal domain of 54 amino acid residues, and an internal transmembrane domain (TMD) of 20 to 25 amino acid residues.[145,146] The M_2-TMD consists of a left-handed bundle of four α-helices[169,170] [Fig. 4.1(a)] stabilized by disulfide bonds between the N-terminal domains of the M_2 protein at Cys^{17}, Cys^{19}, or both.[148,165] Thus the homotetrameric structure is either as a pair of disulfide-linked dimers[148,171] or four disulfide-linked monomers[165]. The helices of the influenza A M_2-TMD protein are tilted in such a way [Fig. 4.1(b)] that the N-terminal end of the channel is wider than the C-terminal end.[167] This tilted-helix bundle geometry [Fig. 4.1(b)] enables the amantadine molecule to enter the channel and interact with the residues close to the N-terminal end and prevents it from passing through the C-terminal end of the

channel.[167] The M_2-TMD channel has an amphiphilic nature that contributes to its role as a target of the amantadine interaction.[148,155]

Under ideal conditions, the M_2 channel only transports protons and this permeation increases as the external pH decreases below 8.5 until it reaches a saturation level at pH 4.[33–36] The permeation of other ions through this channel is observed in experiments as well.[35,37–41] Mutagenesis studies suggested that the Trp^{41} side-chains function as a gate that opens and closes the M_2-TMD pore for proton current at low and high pH, respectively,[41] whereas the the His^{37} side-chains function as a selectivity-filter for protons.[39,172]

Two hypothesized conductance mechanisms could naturally produce proton-selective transport, namely, the shuttle[170] and the water-wire[173] mechanisms. In the water-wire mechanism, protonation of the His^{37} residues, leads to an electrostatic repulsion among these residues, causing them to move apart like the opening of a shutter, which allows formation of a narrow strand of water through the pore. Then protons hop by proton-selective Grotthuss transport[174] through a continuous water wire from the virus exterior to the virus interior. In the shuttle mechanism, protonation of the imidazole N_{δ_1}, which points to the virus exterior, is followed by deprotonation of the imidazole N_{ε_2}, allowing the proton translocation into the virus interior. Then a tautomerization (His^{37} ring flip) completes the cycle. There are many studies that support the water-wire mechanism,[156,171,173,175,176] but there are also many evidences that support the shuttle mechanism.[41,170,177–179]

A more complex aspect of M_2 conductance is its so-called acid-activation. The channel clearly transports more protons at lower pH, but it is not clear whether this represents activation of a rate-limiting shuttle mechanism or just the effect of mass action with the water-wire mechanism. If the latter case is true, there is no need to invoke a gating mechanism to explain the increase in conductance at low pH, but there are some subtle experimental observations that still suggest some sort of gating mechanism. For instance, external basification reduces outward proton flow in transfected cells.[33] Therefore, some gating of current flow may occur. One might expect mutual repulsion between titrated His^{37} residues[173] or uncoupling of imidazole-imidazolium complexes[180] to open the channel for water-wire formation, but the positively-charged selectivity-filter might also electrostatically inhibit proton passage. Experimental evidence seems to suggest that acid-activation involves

Trp^{41}, which may be coupled to His^{37} protonation and which partly or completely closes off the channel at high pH.[41] Although gating may be most relevant in explaining acid-activated proton currents for the water-wire mechanism, it may also play a role in explaining the subtle modulations observed experimentally in the context of the shutter mechanism.

This study explores the behavior of ionic species in the M_2-TMD channel based on solid state NMR observables (PDB #1NYJ) and initially thought to represent the closed state.[9] Previous simulations with this structure have demonstrated that, when the selectivity-filter is multiply-titrated, it relaxes to a water-containing structure, which can pass protons but still has a high barrier to Na^+.[159] However, the relaxed, water-filled structure observed in such simulations raises questions about the occupancy of the charged selectivity-filter thought to represent the open state. Namely, do Cl^- ions occupy the charged selectivity-filter and neutralize it? Is the free-energy barrier to Cl^- passage lower than that of cation passage when there is fixed charge in the selectivity-filter? With slight relaxations, does the structure retain its tightness against Na^+ transport? Are there significant structural differences between the 1NYJ model and other models extracted from NMR and X-ray experiments? We conducted molecular dynamics (MD) and umbrella sampling simulations to answer those questions. In the process, we observed His^{37} and Trp^{41} configurations that suggested a mechanistic coupling of the shuttle and shutter mechanisms.

4.2 Methods

4.2.1 Model System and Parameters

The initial system consisted of an M_2-TMD homotetramer, with the 1NYJ structure (Fig. 4.1),[9] embedded in 96 DMPC molecules as a lipid bilayer, as well as 6400 water molecules, and 1 mol/kg NaCl or NH_4Cl. The 1NYJ structure represents M_2-TMD channel as homotetramer with a left-handed bundle of four α-helices.[9] The α-helix was obtained from solid-state NMR spectroscopy in a hydrated DMPC bilayer, which consists of 22–46 residues with the amino acid sequence: NH_3^+-Ser^{22}-Ser-Asp-proline-Leu-Val-Val-alanine-alanine-Ser-Ile-Ile-glycine-Ile-Leu-His^{37}-Leu-Ile-Leu-Trp^{41}-Ile-Leu-Asp-Arg-Leu^{46}-COO^-.[9] A TIP3P model was used as the wa-

ter model, which was modified in CHARMM from the original model[95]. The initial crystal-like structure was constructed, using the VMD software,[96] in a box with initial dimensions of 62 × 62 × 80 Å in *x*, *y*, and *z* dimensions, respectively. This system was denoted M_2-$TMD_{His_4^{+0}}$.

Another two M_2-TMD systems were modeled using the same traditional empirical-force-field approach as the M_2-$TMD_{His_4^{+0}}$. In the first system, two opposite histidine residues were protonated, whereas in the second system three histidine residues were so protonated using a covalent bond in the force field. The former system was denoted M_2-$TMD_{His_4^{+2}}$, whereas the later was denoted M_2-$TMD_{His_4^{+3}}$. This approach allows us to examine the limiting electrostatic effects of His^{37} titration.

The ammonium ion (NH_4^+) force field was not available in the empirical force field. Its parameters were obtained using the Extensible Computational Chemistry Environment (ECCE)[137] after performing quantum mechanics calculations using NWChem[138,139]. The ammonium ion was built in ECCE and geometrically optimized at the RHF level of theory with the 6-311++G(3df,3pd) basis set, with Pople(3df,3pd) as a polarization function, and with Pople-style as a diffusion function. The bond lengths for the ammonium ion were derived from the resulting structure. The atomic partial charges were derived using electrostatic potential fitting. Energy constants were taken from the CHARMM, version 22, force field for primary amines. The ammonium ion parameters are listed (Table 4.1). To produce electroneutrality for the M_2-TMD systems, appropriate numbers (4, 2, or 1) of Cl^- ions were removed from M_2-$TMD_{His_4^{+0}}$, M_2-$TMD_{His_4^{+2}}$, or M_2-$TMD_{His_4^{+3}}$, respectively.

Table 4.1: Ammonium Ion Parameters

Stretching	Elements	Energy constant (K_b) [a] ($kcal/(mol·Å^2)$)	Bond length (Å)
	N–H	403.0	1.003
Bending	Elements	Energy constant (K_θ) [a] ($kcal/(mol·rad^2)$)	Bond angle (°)
	H–N–H	44.0	109.471
Electrostatic	Elements	Partial charge	
	N	−0.625490	
	H	+0.406372	

[a]Extracted from version 31 of the CHARMM force field

4.2.2 System Preparation and Simulation Parameters

We applied the same simulation parameters as mentioned in Sections 2.2.2–2.2.4 but different detailed preparation steps (Table 4.2). Briefly, we mention the differences between the two approaches.

We used the same surface tension value, γ = 40 dyn/(cm·interface), which was used with gA system in Section 2.2.2, because of a well estimated surface area of gA channel,[61] whereas it is unknown for the M_2-TMD channel.

Table 4.2: Summary of M_2-TMD System Preparation Approach

Process	Ensemble [a]	Restraints (k_f [b], kcal/(mol·Å^2))				Steps
		Lipids [c]	Protein [d]			
		P	bb	non bb	com	
Minimization 1	NVT	200	F	F		10,000
Heating 1	NV	200	F	F		20,000
Equilibration 1	NVT	200	F	F		100,000
Annealing [e]	NV	200	F	F		200,000
Minimization 2	NVT	200	F			3000
Heating 2	NV	20	F			50,000
Equilibration 2	NPAT	20	F			100,000
Equilibration 3	NPγT	10	F			10,000,000
Equilibration 4	NPAT	2	100			100,000
Equilibration 5	NPAT	1	40			100,000
Equilibration 6	NPAT		10			100,000
Equilibration 7	NPAT		2			100,000
Equilibration 8	NPAT		0.4			100,000
Equilibration 9	NPAT		0.1			267,000
Equilibration 10	NPAT				1000	1,250,000

[a] The symbols in this column stand for; N: constant number of atoms, V: constant volume, T: constant temperature, P: constant pressure, A: constant area, γ: constant surface tension
[b] k_f: force constant
[c] The symbol in this column stands for; P: phosphorus atoms
[d] The symbols in this column stand for; bb: backbone, com: center-of-mass, F: fixed atoms
[e] It consists of three stages with each stage: 40 ps of heating to 1000 K followed by 80 ps of cooling to 303.15 K

The simulations in the NPAT ensemble (Equilibrations 4–10) utilized a tetragonal box having a lateral dimension of 59.849 Å, the final value after the Equilibration 3 stage.

The conformational stability of the side-chains can be represented by their torsion angles (dihe-

dral angles) such as χ_1 and χ_2 angles. For histidine side-chains, the χ_1 angle is the counterclockwise rotation of the C_β–C_γ bond around the C_α–C_β bond in N–C_α–C_β–C_γ chain of atoms, whereas χ_2 angle is the counterclockwise rotation of the C_γ–N_{δ_1} bond around the C_β–C_γ bond in C_α–C_β–C_γ–N_{δ_1} chain of atoms.[119] For tryptophan side-chains, the χ_1 angle is the counterclockwise rotation of the C_β–C_γ bond around the C_α–C_β bond in N–C_α–C_β–C_γ chain of atoms, whereas χ_2 angle is the counterclockwise rotation of the C_γ–C_{δ_1} bond around the C_β–C_γ bond in C_α–C_β–C_γ–C_{δ_1} chain of atoms.[119] These definitions give a positive torsion angle, whereas a negative torsion angle requires rotation in the opposite direction. The rotameric state was given to each side-chain based on observing their χ_1 and χ_2 fluctuations around their averages, most of the simulation time scale (8–10 ns). A rotameric state combination is represented with a notation (His^{37}, Trp^{41}).

The tilt angle was computed by calculating the angle between the helix principle axis and the bilayer normal, and then averaged over all helices and trajectories.

The interhelical distance was computed by calculating the distance between two neighboring helices using their COM, and then averaged over all trajectories.[159,181,182] This distance was also calculated at another two different points, at the C-terminal end of the principle axis and at the N-terminal end of the principle axis taken at equal distances from the helix COM.

Another interesting distance was computed after averaging over all trajectories is the $Trp^{41}_{C_\gamma}$–$His^{37}_{N_{\delta_1}}$ distance, which is the distance between C_γ in Trp^{41} from $helix_i$ and N_{δ_1} in His^{37} from $helix_{i+1}$.[9] The notation $H_{i-(i+1)}$ was used to denote distances between residues on $helix_i$ and $helix_{i+1}$, where the latter is the clockwise adjacent helix as viewed from the C-terminus side.

In the umbrella sampling simulations, the ITC method was used to define the transport coordinate for both systems. During umbrella sampling with the test ion, the spherical restraint was not applied, but a cylindrical restraint (k_f = 20 kcal/(mol·Å^2)) was applied on the test ion to keep it within 10 Å of the *z* axis. The purpose of the cylindrical restraint is to assure a bounded sampling region outside the channel for the test ion.[11,80,84]

4.3 Results and Discussion

4.3.1 Preparation and Simulation Methods Stability

The preparation process generally produced stable and randomized systems compared with the initial crystal-like structures. For example, the simulating annealing, based on the deuterium order parameters [Figs. 4.2(a) and (b)], was sufficient to produce disordered lipid tails in the presence of either NaCl or NH_4Cl saline solution. Our results agree excellently with both the experimental [125–127] and the simulation [103] results, except in the region close to the head group, where the order remains high in experiments, [125–127] but commonly declines in simulation. [103] The consistency in the order parameters results among different M_2-TMD structures as well as saline solutions is an indication of the robustness of the preparation method.

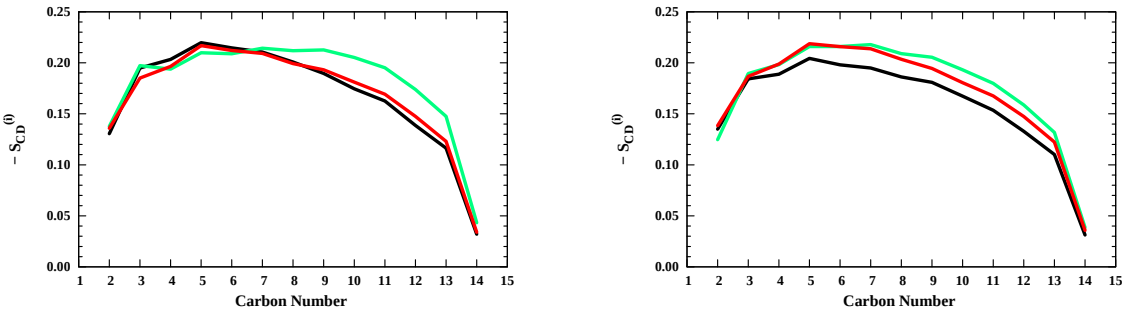

Figure 4.2: Deuterium order parameters for the DMPC tails in M_2-$TMD_{His_4^{+0}}$ (black line), M_2-$TMD_{His_4^{+2}}$ (green line), and M_2-$TMD_{His_4^{+3}}$ (red line) systems with (*a*) NaCl and (*b*) NH_4Cl saline solutions.

Our RMSD results show reasonable protein-backbone structural stability within the production run time scale for all M_2-TMD structures in NaCl saline solution [Fig. 4.3(a)], whereas slight excesses occurred in the presence of NH_4Cl saline solution [Fig. 4.3(b)] after 3 ns, specially for the M_2-$TMD_{His_4^{+3}}$ structure. This might indicate some structural variations, but are not necessarily caused by the presence of the NH_4Cl saline solution. However, our RMSD results are in good agreement with previous simulation observations. [171,175,178,183,184]

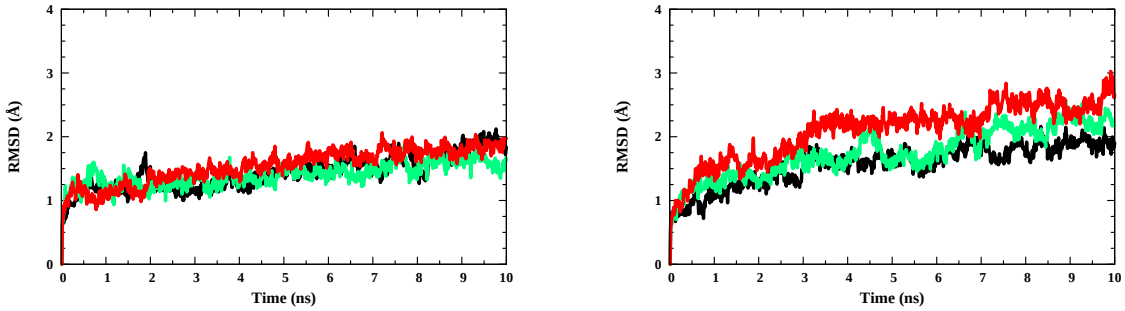

Figure 4.3: RMSD versus time for the protein backbone in M_2-TMD$_{His_4^{+0}}$ (black line), M_2-TMD$_{His_4^{+2}}$ (green line), and M_2-TMD$_{His_4^{+3}}$ (red line) systems with (*a*) NaCl and (*b*) NH_4Cl saline solutions.

4.3.2 M_2-TMD Channel Structural Analysis

Some of the M_2-TMD channel structure properties in the presence of NaCl or NH_4Cl saline solutions are listed (Tables 4.3 and 4.4) and compared with those from experimental models using our calculations. The tilt angle averages in the presence of two different saline solutions are in a good agreement with experimental observations,[9,159,168,169,185] even though there are large fluctuations in the protonated structures. Slight variances of our results with some experimental[186–188] and simulation[171,173,177,178,189] results are expected because of different M_2-TMD length, lipid bilayer environment, water model, hydration level, experimental source, equilibration level, or simulation length. However, the basic size and shape of the molecule is now established, and our results further attest to the stability of the 1NYJ structure in the lipid membrane environment.

The interhelical distances at the C- and N-termini have rather modest fluctuations around their averages and are higher than those from the experimental models. We speculate that these values might be moderated and stabilized for the whole protein in simulations as they are in experiments.[188] On the other hand, the average distances between the COM of two neighboring helices are consistent with results from experimental studies.[159,185,186] Previous studies suggested that an interhelical

distance within the range of 9.5–10.2 Å is an indication of a channel in the closed form, where water penetration is not possible.[9,173,178,187] The slight increase in this distance, as we change the M_2-TMD$_{His_4^{+0}}$ to the M_2-TMD$_{His_4^{+3}}$ structure, may be caused by the electrostatic repulsion effect in the selectivity-filter, which was also observed in other MD simulations.[173,175–178]

Table 4.3: Some M_2-TMD Channel Structure Properties in NaCl Saline Solution

PDB Structure		1NYJ			1NYJ	2H95	2RLF [a]	3C9J
		M_2 TMD$_{His_4^{+0}}$	M_2 TMD$_{His_4^{+2}}$	M_2 TMD$_{His_4^{+3}}$				
Source		MD Simulations			NMR	NMR	NMR	X-ray
Residues		22–46			22–46	26–43	18–60	22–46
Lipid Bilayer		DMPC			DMPC	DMPC	DHPC [b]	
Reference		This work			(9)	(186)	(187)	(185)
Tilt Angle (°)		36.9 ± 3.9	39.6 ± 5.6	38.0 ± 2.8	37	23	16	32
Interhelical	C [c]	17.6 ± 0.9	19.5 ± 2.2	17.8 ± 1.1	17	12	12	24
	M [d]	11.4 ± 0.8	11.7 ± 1.3	11.6 ± 0.8	10	13	10	12
Distance (Å)	N [e]	18.9 ± 2.1	18.9 ± 1.1	19.5 ± 1.3	17	16	13	11
Trp$^{41}_{C_\gamma}$–His$^{37}_{N_{\delta_1}}$	H_{A-B}	5.5 ± 0.4	8.1 ± 0.8	4.8 ± 0.5	3.8	10.9	9.3	16.0
	H_{B-C}	5.6 ± 0.7	5.4 ± 1.0	7.4 ± 0.8	3.7	10.9	9.0	13.7
Distance (Å)	H_{C-D}	6.8 ± 1.0	5.3 ± 0.4	5.6 ± 0.5	3.7	10.9	8.6	15.0
	H_{D-A}	5.8 ± 0.9	4.6 ± 0.4	6.1 ± 0.6	3.8	10.9	8.6	14.0
His^{37}	H_A	**t**−80°	**t**−80° [f]	**t**−80° [f]	**t**−160°	**t**−160°	**t**−80°	**t**60°
	H_B	**t**60°	**m**−170° [g]	**t**−80° [f]	**t**−160°	**t**−160°	**t**−80°	**t**60°
Rotamer [h]	H_C	**t**60°	**t**60° [f]	**t**−80° [f]	**t**−160°	**t**−160°	**t**−160°	**t**−160°
	H_D	**t**−80°	**t**−80°	**t**60°	**t**−160°	**t**−160°	**t**−80°	**t**60°
Trp^{41}	H_A	**t**−105°	**t**−105°	**t**90°	**t**−105°	**m**95°	**t**−105°	**t**90°
	H_B	**t**90°	**m**0°	**t**−105°	**t**−105°	**m**95°	**t**−105°	**t**90°
Rotamer [h]	H_C	**t**90°	**t**90°	**t**−105°	**t**−105°	**m**95°	**t**−105°	**t**90°
	H_D	**t**−105°	**t**90°	**t**−105°	**t**−105°	**m**95°	**t**−105°	**t**90°

[a] The analysis for this structure was performed on the residues 22–46
[b] DHPC stands for 1,2-Dihexanoyl-sn-glycero-3-phosphocholine
[c] C Stands for the distance between two neighboring helices using the C-terminal end of the principle axis
[d] M Stands for the distance between two neighboring helices using the COM of each helix
[e] N Stands for the distance between two neighboring helices using the N-terminal end of the principle axis
[f] This is for a protonated histidine residue
[g] This is not a common rotamer in the Lovell et al. library.[119]
[h] H_i stands for helix *i*

Table 4.4: Some M_2-TMD Channel Structure Properties in NH_4Cl Saline Solution

PDB Structure		1NYJ			1NYJ	2H95	2RLF [a]	3C9J
		M_2 $TMD_{His_4^{+0}}$	M_2 $TMD_{His_4^{+2}}$	M_2 $TMD_{His_4^{+3}}$				
Source		MD Simulations			NMR	NMR	NMR	X-ray
Residues		22–46			22–46	26–43	18–60	22–46
Lipid Bilayer		DMPC			DMPC	DMPC	DHPC [b]	
Reference		This work			([9])	([186])	([187])	([185])
Tilt Angle (°)		37.2 ± 3.8	36.1 ± 3.5	37.9 ± 6.4	37	23	16	32
Interhelical	C [c]	17.1 ± 1.3	18.0 ± 2.4	17.7 ± 1.2	17	12	12	24
	M [d]	11.2 ± 0.8	11.5 ± 1.8	11.8 ± 0.6	10	13	10	12
Distance (Å)	N [e]	18.9 ± 2.4	18.5 ± 3.1	20.0 ± 1.5	17	16	13	11
$Trp^{41}_{C_\gamma}$–$His^{37}_{N_{\delta_1}}$	H_{A-B}	4.5 ± 0.4	5.5 ± 0.9	5.0 ± 0.7	3.8	10.9	9.3	16.0
	H_{B-C}	5.4 ± 0.3	6.6 ± 1.3	4.9 ± 1.0	3.7	10.9	9.0	13.7
Distance (Å)	H_{C-D}	5.7 ± 0.3	5.4 ± 0.9	5.8 ± 0.7	3.7	10.9	8.6	15.0
	H_{D-A}	5.6 ± 0.5	7.2 ± 1.2	7.3 ± 0.9	3.8	10.9	8.6	14.0
His^{37}	H_A	**t**−80°	**t**−160° [f]	**t**−160° [f]	**t**−160°	**t**−160°	**t**−80°	**t**60°
	H_B	**t**60°	**t**−80°	**t**−160° [f]	**t**−160°	**t**−160°	**t**−80°	**t**60°
Rotamer [g]	H_C	**t**60°	**t**−160° [f]	**t**−160° [f]	**t**−160°	**t**−160°	**t**−160°	**t**−160°
	H_D	**t**−80°	**t**−80°	**t**60°	**t**−160°	**t**−160°	**t**−80°	**t**60°
Trp^{41}	H_A	**t**−105°	**t**−105°	**t**90°	**t**−105°	**m**95°	**t**−105°	**t**90°
	H_B	**t**90°	**t**−105°	**t**−105°	**t**−105°	**m**95°	**t**−105°	**t**90°
Rotamer [g]	H_C	**t**−105°	**t**−105°	**t**−105°	**t**−105°	**m**95°	**t**−105°	**t**90°
	H_D	**t**90°	**t**90°	**t**−105°	**t**−105°	**m**95°	**t**−105°	**t**90°

[a] The analysis for this structure was performed on the residues 22–46
[b] DHPC stands for 1,2-Dihexanoyl-sn-glycero-3-phosphocholine
[c] C Stands for the distance between two neighboring helices using the C-terminal end of the principle axis
[d] M Stands for the distance between two neighboring helices using the COM of each helix
[e] N Stands for the distance between two neighboring helices using the N-terminal end of the principle axis
[f] This is for a protonated histidine residue
[g] H_i stands for helix i

A REDOR solid-state NMR spectroscopy study suggested that the distance between the C_γ in Trp^{41} from $helix_i$ and N_{δ_1} in His^{37} from $helix_{i+1}$ is < 3.9 Å and represents the channel in the closed form.[9] Our results are relatively higher than 3.9 Å (Tables 4.3 and 4.4) and less than those values measured experimentally,[185–187] but consistent with a previous simulation observation.[176] Because the thermally relaxed version of the solid state NMR M_2-TMD structure is somewhat more open in the region of His^{37} cluster, there may be other components, such as the Trp^{41} residues, shuttering the channel (see below).

4.3.3 The Rotameric Basis of Trp^{41} Gating

Various rotameric states for His^{37} and Trp^{41} side-chains were observed in our simulations with NaCl or NH_4Cl saline solution (Tables 4.3 and 4.4). The most commonly observed rotameric states **t**-105° [Fig. 4.4(a)], which blocks the channel from passing water molecules or ions [Fig. 4.4(b)], and the **t**90° [Fig. 4.4(c)], which allows the channel to pass water and ions with the size of water or smaller [Fig. 4.4(d)]. This apparent gating function of Trp^{41} side-chains in our simulations is in a good agreement with the mutagenesis study.[41] To our knowledge, the Trp^{41} side-chain rotamer, **t**-105°, has never previously been proposed to be the rotamer that blocks the M_2-TMD channel.

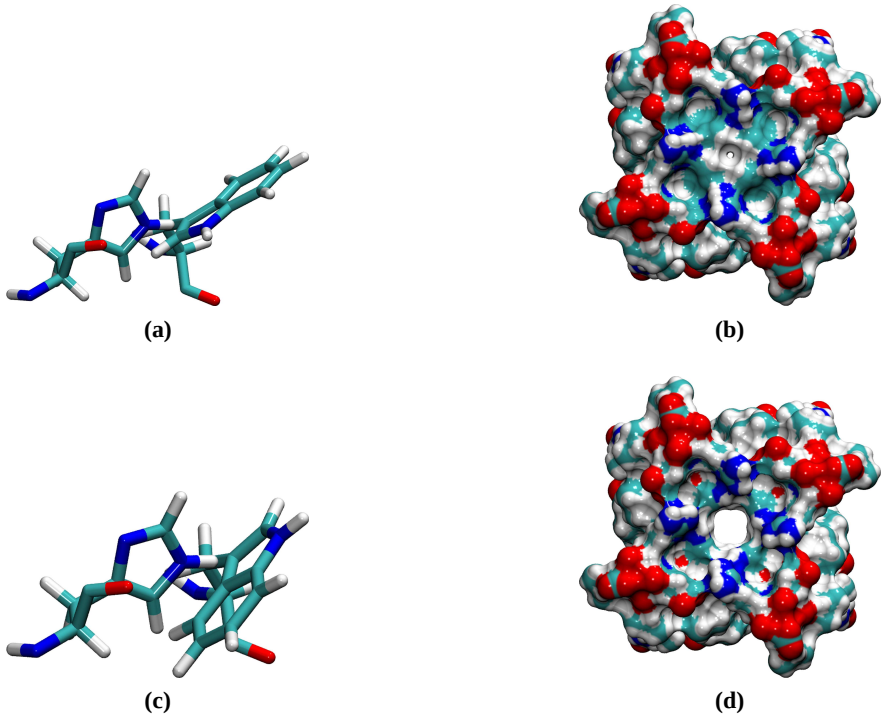

Figure 4.4: Selected Rotameric states for the (His^{37}, Trp^{41}) conformations; (**t**-80°, **t**-105°) in (*a*) and (*b*), (**t**-80°, **t**90°) in (*c*) and (*d*), are demonstrated using the initial 1NYJ structure. The His^{37} and Trp^{41} residues from two adjacent helices are shown by the Licorice drawing method, whereas the whole protein is shown by the Maximal Speed Molecular Surface (MSMS) drawing method using a probe radius of 1.4 Å.The colored objects represent: C (cyan), H (white), N (blue), and O (red). In the Licorice images, the left-side of the image points toward the N-terminus side, whereas the right-side of it points toward the C-terminus side. In the molecular surface view, the perspective is looking from the C-terminus end.

The illustrations of side-chains configurations [Figs. 4.4(a) and (c)] reveal that there is a possible favorable interaction between N_{ε_1} in Trp^{41} residue from $helix_i$ and H_{ε_2} in His^{37} residue from $helix_{i+1}$ as a hydrogen bonding (H-bonding) interaction. Although the NMR spectra results suggested that there is a possibility of H-bonding interactions as imidazole–imidazolium interactions,[180] an alternative interpretation could be H-bonding interactions between His^{37} and Trp^{41} residues.

The **t**-160° His^{37} rotameric state and the **t**-105° and **t**90° rotameric states for Trp^{41} side-chains were also observed in restrained MD simulations.[176] Assuming Trp^{41} side-chains function as a gate in the M_2-TMD channel, will it be necessary for all four to assume the **t**-105° rotameric state at high pH to prevent water or ion penetrations? The next discussion explores the importance of this rotameric state for spontaneous water and ion distributions in the channel.

4.3.4 Distribution of Water Molecules and Ions

A zoomed-in water density inside the M_2-TMD channel in the *z* direction for two different saline solutions are shown [Figs. 4.5(a) and (b)]. There is an occasional presence of few water molecules in the selectivity-filter at z = 5 Å, even for the M_2-$TMD_{His_4^{+0}}$ structure. The occasional presence of water molecules in the filter raises the possibility that ions can enter the channel as well.

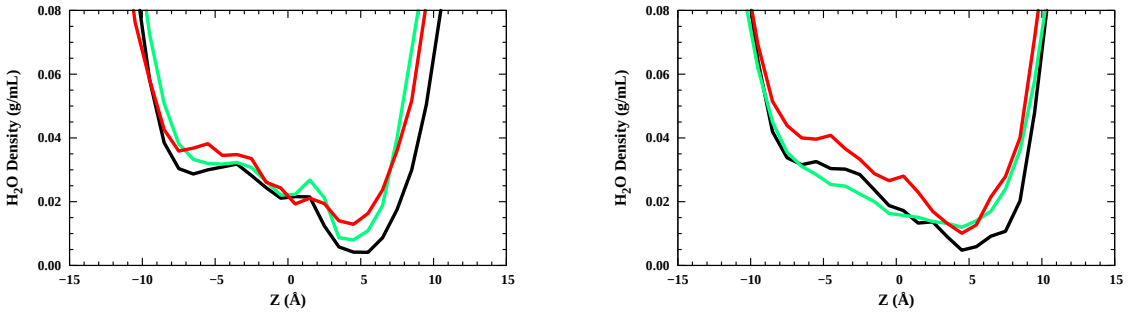

Figure 4.5: A zoomed in water density profile inside a channel in the *z* direction in M_2-$TMD_{His_4^{+0}}$ (black line), M_2-$TMD_{His_4^{+2}}$ (green line), and M_2-$TMD_{His_4^{+3}}$ (red line) systems with (*a*) NaCl and (*b*) NH_4Cl saline solutions.

We examined the Cl^- ions molality profiles [Figs. 4.6(a) and (b)] in NaCl or NH_4Cl saline solution, respectively. There are not any Cl^- ions in the selectivity region (around z = 5 Å) for M_2-$TMD_{His_4^{+0}}$ and M_2-$TMD_{His_4^{+2}}$ structures during the simulation time scale, whereas some Cl^- ions were able to enter the selectivity-filter region for M_2-$TMD_{His_4^{+3}}$ structure.

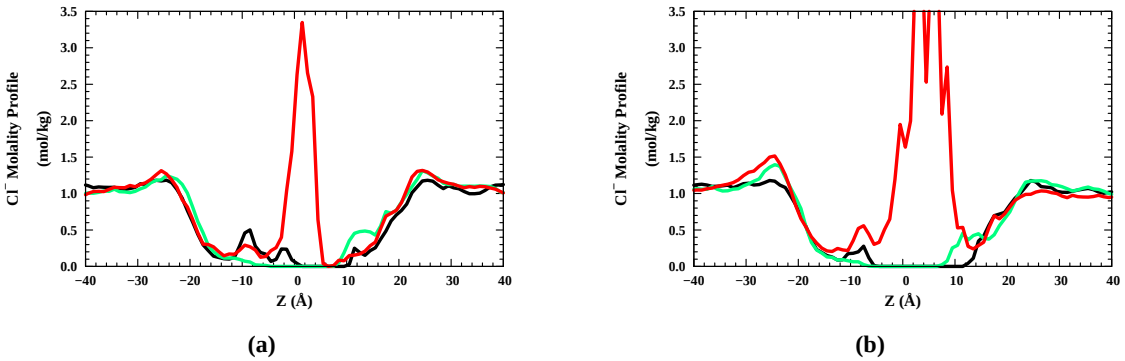

Figure 4.6: Cl^- ions molality profiles in the z direction in M_2-$TMD_{His_4^{+0}}$ (black line), M_2-$TMD_{His_4^{+2}}$ (green line), and M_2-$TMD_{His_4^{+3}}$ (red line) systems with (*a*) NaCl and (*b*) NH_4Cl saline solutions.

Neither Na^+ [Fig. 4.7(a)] nor NH_4^+ [Fig. 4.7(b)] ions have any occupancy in the selectivity-filter region. In all M_2-TMD structures, the high cation occupancy in the region ($10 < z < 20$ Å) is due to the negatively charged C-terminus side. The high cation occupancy in the M_2-$TMD_{His_4^{+0}}$ structure in ($-4 < z < 4$ Å) is reduced by the repulsion effects from protonated imidazole rings for the $+2$ and $+3$ states. All anion and cations molality profiles show good homogeneity in the bulk region ($|\, z \,| > 30$ Å).

Because Cl^- ions have a better chance of entering the selectivity-filter than their counterions due to electrostatic effect, we next examine the height of the free-energy barrier in the selectivity-filter region. In the next section, extracted PMFs from umbrella sampling simulations are used to answer that question using the partially open-gated channels for which the simulation started with the side-chains conformations as listed (Tables 4.3 and 4.4).

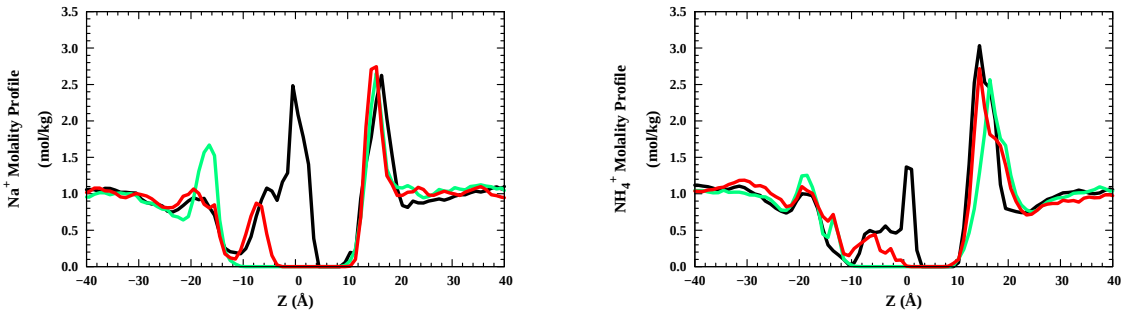

(a) **(b)**

Figure 4.7: Cation molality profiles in M_2-$TMD_{His_4^{+0}}$ (black line), M_2-$TMD_{His_4^{+2}}$ (green line), and M_2-$TMD_{His_4^{+3}}$ (red line) systems for (*a*) Na^+ and (*b*) NH_4^+ ions.

4.3.5 Ions Potential of Mean Force

Generally, the free-energy barrier in the selectivity-filter region (Fig. 4.8) does not exceed 8 kcal/mol for any of the three ions or any of the three-charged states, which would probably be low enough to allow significant permeation.[91] Therefore, the partially open state used in these umbrella sampling simulations does not fully exclude water and ions, as we would expect the fully closed state would do.

Changing from M_2-$TMD_{His_4^{+0}}$ to M_2-$TMD_{His_4^{+3}}$ structure, the selectivity-filter free-energy barrier in the Cl^- PMF [Fig. 4.8(a)] gets lower. As expected, this behavior is in the opposite sense for the Na^+ PMF [Fig. 4.8(b)] and for the NH_4^+ PMF [Fig. 4.8(c)], except for the M_2-$TMD_{His_4^{+3}}$ structure, where the more open form of the channel allows a lower barrier in spite of the electrostatic repulsion of the tetraimidazole selectivity-filter.

The electrostatic attraction between the Cl^- ion and the protonated imidazole rings is the apparent cause for the decrease in the Cl^- translocation free-energy barrier. A possible explanation for the low NH_4^+ PMF barrier, using the M_2-$TMD_{His_4^{+3}}$ structure, is the potential of NH_4^+ ions to form hydrogen bonds with the protonated imidazole rings, which might partially compensate the repulsion effect in the selectivity-filter.

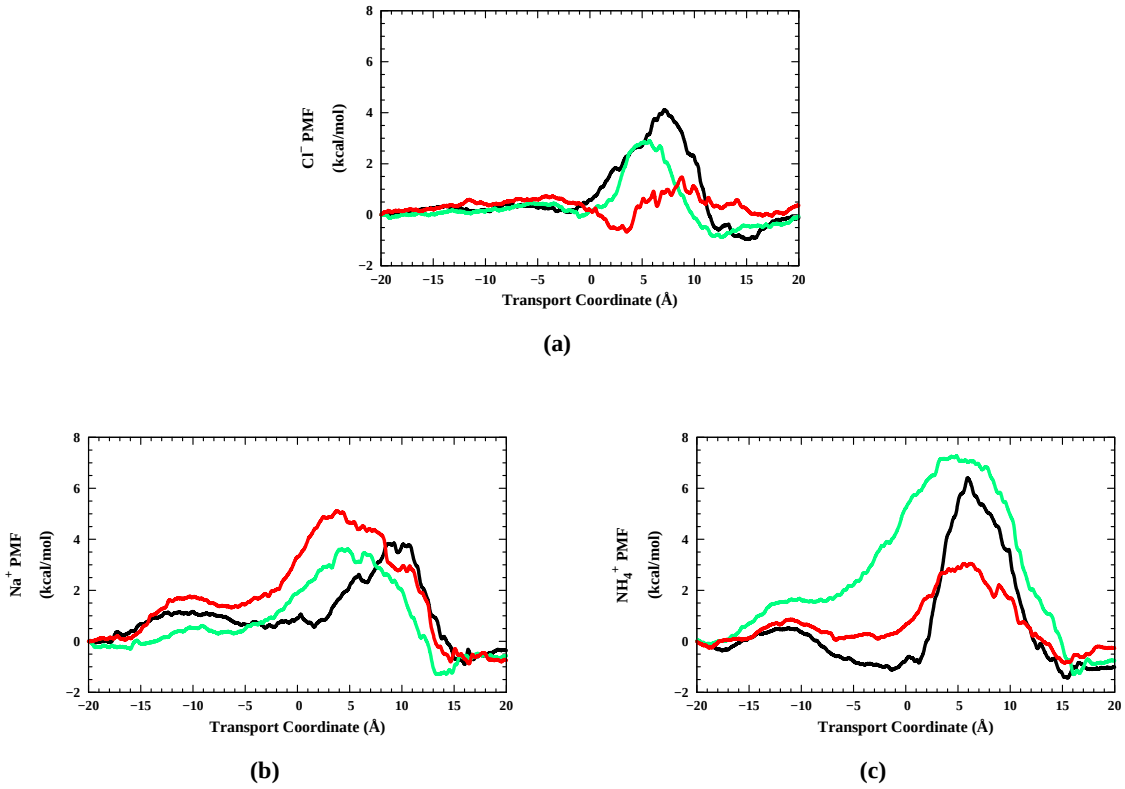

Figure 4.8: One-dimensional ions PMF as a function of the transport coordinate. The PMF is shown in M_2-$TMD_{His_4^{+0}}$ (black line), M_2-$TMD_{His_4^{+2}}$ (green line), and M_2-$TMD_{His_4^{+3}}$ (red line) systems for (*a*) Cl^-, (*b*) Na^+, and (*c*) NH_4^+ ions.

The cation results imply that the channel has a higher permeability for NH_4^+ ions than for Na^+ ions, which is in a good agreement with some of the electrophysiological results.[40] However, the simulations make the prediction that the channel would have a higher permeability for Cl^- ions than for either Na^+ or NH_4^+ ions, which, although might be expected on electrostatics grounds, was not seen in whole-cell clamping of mouse erythroleukemia (MEL) cells.[33,36] Of course, in contrast to the simulations with covalently titrated imidazole groups, experimentally, the protons titrating the His^{37} residues could flea in advance of incoming cations and might not substantially inhibit cation flow, and likewise a fourth titration might stabilize and be stabilized by Cl^- in the filter. So, the remarkable finding here is that non-protonic current would appear to be moderately high for this structure in any of the selectivity-filter states, provided that the Trp^{41} side-chains are in the open configuration.

Convergence, determined from increasingly complete data sets, accuracy, judged from the proximity of the free-energy integral endpoint to the reference potential on the opposite side of the bilayer, and methodological independence, judged from comparison of the WHAM method to the PMR method [Eq. (2.7)], were all excellent, yielding uncertainties of ≈ 1 kcal/mol.

From our simulations of Cl^- and NH_4^+ transport, it appears that the open 1NYJ-based structure would not fully exclude non-protonic ions like the whole protein in MEL cells does. Of course, the whole protein may yield slightly different tilt angles and His^{37}–Trp^{41} rotamer positions.[188] From our results, we next speculate briefly about the rotameric basis that may underlie a shuttle mechanism for selective proton transport.

4.3.6 M_2-TMD Revised Conductance Mechanism

Our proposed conductance mechanism is evolved from the shuttle mechanism,[170] its revised form,[41] and the following evidences and observations: 1) The M_2 channel is selective for protons with the Na^+:H^+ permeability ratio $< (3\text{–}8) \times 10^{-7}$ and the alkali-ions:H^+ permeability ratio $< 1 \times 10^{-5}$, as estimated from electrophysiological data.[33–36,190] 2) The M_2 channel still has the ability to permeate ions (non-protons) under certain conditions albeit with very low permeability ratio.[33–36,190] 3) Cation–π interaction between protonated His^{37} and indole ring of Trp^{41} was observed in a Raman spectroscopy experiment,[156] and in ab initio calculations with a suggested (**t**60°, **t**90°) conjugate rotamer.[176] Cation–π interactions are common in biological receptors, especially involving side-chains of aromatic amino acids, such as phenylalanine, tyrosine, or tryptophan.[191–196] The cation–π interaction in the M_2 channel, might resemble a H–π interaction in the HF-benzene complex,[197] where the H–π bond energy was estimated to be 2 kcal/mol. 4) His^{37} side-chains function as a selectivity-filter for protons in the M_2 channel.[39,172] 5) Trp^{41} side-chains function as a gate in the M_2 channel.[41] 6) A possible H-bonding interaction between H_{ε_2} from His^{37} and N_{ε_1} from Trp^{41}, as suggested from previous illustrations, might stabilize the closed form (unprotonated imidazole rings) of the M_2 channel.[180] 7) The proton turnover rate estimated from vesicle uptake experiments[34,190] may be as low as 1 s^{-1} if indeed the protein was fully active after reconstitution, probably must be lower than 10^6 s^{-1} if selectivity is to be retained, and has been estimated to be $\approx$

1000 s^{-1} based on current density and estimated protein density in Xenopus oocytes.[198]

The proposed conductance mechanism scenario is: 1) As the pH goes down (< 6),[33,39,159,175] a proton approaches N_{δ_1} in the indole ring from the N terminus side, protonating it, while His^{37} and Trp^{41} residues are in the (**t**-80°, **t**-105°) rotameric state, which provides a proposed H-bonding interaction[180] [Fig. 4.9(a)]. 2) After protonating N_{δ_1} of the imidazole ring, both His^{37} and Trp^{41} residues start to change their conformations (χ_1 and χ_2) to stabilize this perturbation [Fig. 4.9(b)], proceeding towards a transition state. This protonating process destabilizes the imidazole ring with sufficient substantial energy ($\approx$ 17 kcal/mol),[199] initiating the energy barriers through going to the transition state. 3) During the conformational change process, we suggest two important intermediate conjugate rotamers; the (**t**0°, **t**-105°) [Fig. 4.9(c)], where the His^{37} residue changes its (χ_1 and χ_2) to (165° and 0°), and the (**t**0°, **t**90°) [Fig. 4.9(d)]. The stable conformation (**t**0°, **t**90°) was observed in ab initio calculations, where the calculated energy for changing His^{37} rotamer from **t**-160° to **t**0° was 5 kcal/mol.[176] 4) A possible transition state [Fig. 4.9(e)] provides a cation–π interaction. Changing (χ_1 and χ_2) for His^{37} residue to (165° and 90°), and for Trp^{41} residues to (150° and 100°) helps obtain the transition. For this transition, the indole ring rotates clockwise (from the lumenal perspective) from [Fig. 4.9(c)] to [Fig. 4.9(e)]. It appears that this is the only possible rotation direction, where there are no side-chains in the indole's way, whereas using the other direction will cause a collision between His^{37} imidazolium ring and Trp^{41} indole ring. 5) The cation–π interaction deprotonates the N_{δ_1} [Fig. 4.9(f)], then the indole π-cloud temporarily holds this proton during the conformational changes of both His^{37} and Trp^{41} residues, as reversible processes through similar intermediates [Figs. 4.9(d) and (c)], before releasing it to the nearby water molecules in the virus interior. This mechanism step helps return the aromaticity to the imidazole ring, which is more stable than the imidazolium ring.[199] During the steps 3–5 the channel would be open for water molecules and other ions for the lifetime of this process, which must be short-lived to preserve selectivity. 6) Departure of the proton completes the cycle.

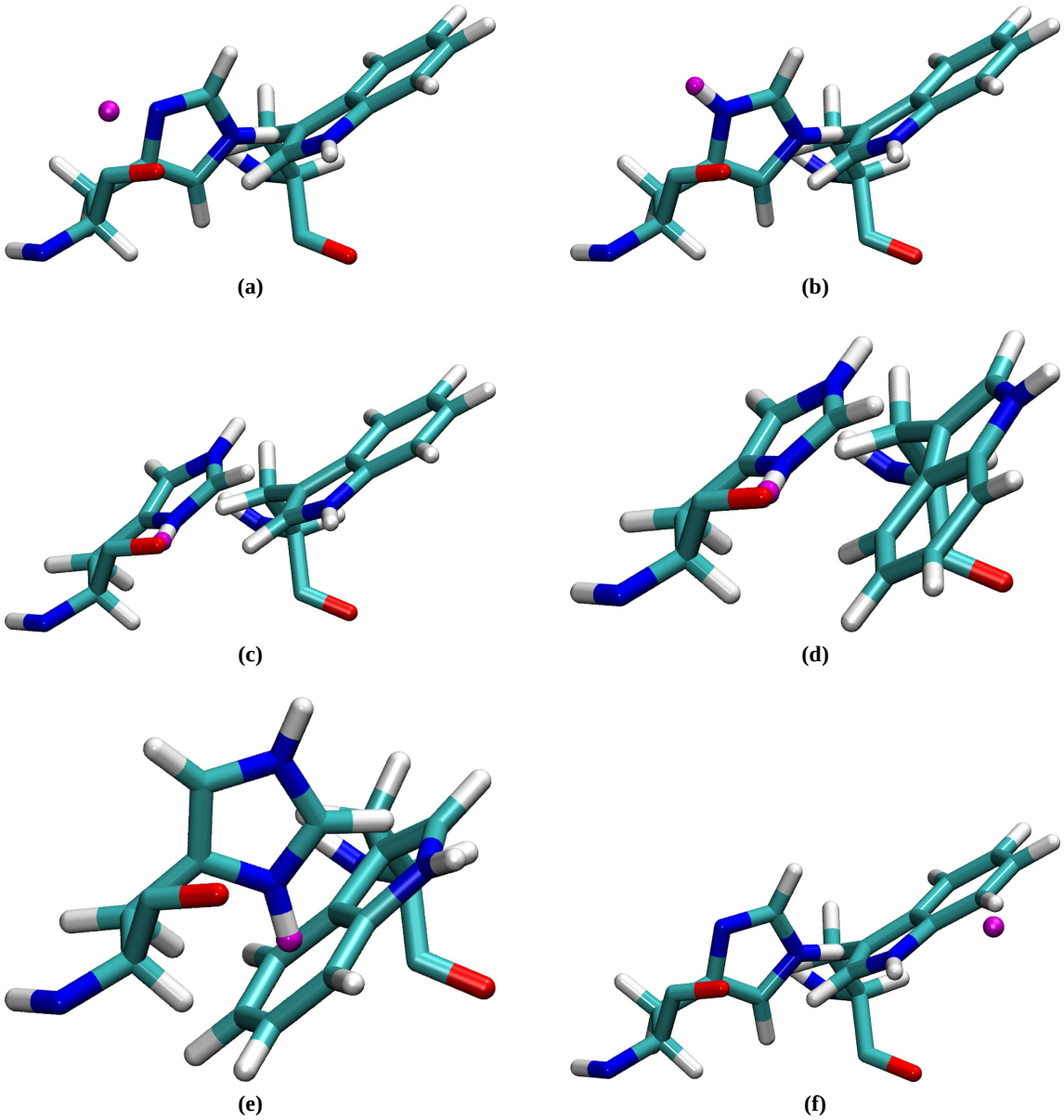

Figure 4.9: Proposed conductance mechanism snapshots using the initial 1NYJ structure. The Trp^{41} from $helix_i$ and His^{37} from $helix_{i+1}$ are shown by the Licorice drawing method, whereas a transported hydrogen entering and leaving the selectivity-filter region is drawn as a sphere. The colored objects represent: C (cyan), H (white), N (blue), O (red), transported-H (magenta). The left-side of each image points toward the N-terminus side, whereas the right-side points toward the C-terminus side.

In this mechanism, the His^{37} side-chain functions as an acceptor and donor group,[172] whereas the Trp^{41} side-chain functions as a carrying group. The cycle could be reversible, so the channel could carry current in either direction.[36]

This proposed mechanism has the ability to explain both the channel selectivity for protons and a modest degree of univalent cation transport through the channel. The observed transportation of univalent cations through the channel in some experiments could be due to some unknown experimental perturbations that make the lifetime of the proposed transition state get longer. Possible future studies include estimating the lifetime for the proposed transition state, simulating H^+–π interactions, exploring the favorable rotamer for His^{37} side-chains when the M_2-TMD is in the closed form, and extracting restrained anion and cation PMFs for the fully opened- and closed-gate M_2-TMD channels.

4.4 Conclusions

Three M_2-TMD structures with two different saline solutions were studied using MD and umbrella sampling simulations. The $M_2\text{-TMD}_{His_4^{+0}}$ has been thought to represent a closed form, whereas the $M_2\text{-TMD}_{His_4^{+2}}$ and $M_2\text{-TMD}_{His_4^{+3}}$ represent intermediate forms.

Generally, our M_2-TMD structures, after 25 ns preparation time with the CHARMM force field, have several of the features observed in NMR and X-ray studies.

The **t**-105° rotamer for Trp^{41} blocks the channel from passing water molecules, whereas the **t**90° rotamer allows the channel to pass them.

Cl^- ions have a lower free-energy barrier in the selectivity-filter region of the M_2-TMD channel than either Na^+ or NH_4^+ ions, and NH_4^+ ions have a higher permeability than Na^+ ions.

A revised conductance mechanism is proposed, in which the His^{37} side-chain functions as an acceptor and donor group,[172] and the Trp^{41} side-chain functions as a carrying group. The proton-transport cycle would be reversible, so the channel could carry current in either direction.[36] Based on this mechanism, because the non-proton ion PMFs have lower energy barriers than the H^+ PMF, which was computed with the empirical valence bond method,[159] the shutter function of the Trp^{41} side-chains, if open long enough, might allow moderate amounts of non-proton ion flow.

Chapter 5

Summary

We have conducted MD and umbrella-sampling simulations to explore the influence of two CHARMM force field improvements on the ion permeation as well as the role of charged ion pathways.

Based on the experimentally derived tryptophan potential relative to phenylalanine potential from rate theory modeling of current-concentration-voltage data, the MacKerell force field for tryptophan residues produces a dynamic average potential energy profile consistent with the predicted free-energy profile. However, in spite of the consistency between the theoretical result for the ion–side-chain interaction and experimental results, there is no significant effect of using the new force field for tryptophan residues on the net free-energy profile. Hence, the improvement in the force field does not improve the agreement between theory and experiment.

The CMAP algorithm helps lower the translocation energy barrier to a reasonable level, despite its lack of chiral symmetry for D-amino acids. That is, the CMAP parameters have been optimized only for L-amino acids, which means a D-amino acid positioned in the chirally inverted configuration will not have the same backbone dihedral energy corrections with CMAP as an L-amino acid. In

contrast, the original peptide bond parameters in version 22 of the CHARMM force field are chirally symmetric. The chiral asymmetry of CMAP limits its usefulness in this work.

Consequently, balancing force field issues (direct and indirect, including polarizability) is required for future studies to assess whether channel conductance estimated from simulations accurately predicts the experimental measurements. In addition, the CMAP algorithm requires further development and testing with different models to produce predictable results that are consistent with those observables extracted from real experiments. Future studies might explore the chirality symmetrization of the CMAP method, the influence of the polarizable water model on the CMAP results, and estimate the conductance from the free-energy profile to compare it with the conductance from the real experiment.

The presence of the negatively charged taurine residues instead of the electroneutral ethanolamine residues at the entrance of the gA channel produces a strong attraction for the cations in the bulk towards the channel mouth. The high central free-energy barrier in the TgA system compared with that in the gA system might be a result of the spherical restraint. The presence of the spherical restraint might cause a flipping difficulty for water molecules inside the TgA channel, which in turn enhances the internal resistance (i.e., produces a higher central free-energy barrier). Future studies might explore the PMF in the TgA system without the spherical restraint as well as how the estimated conductance from the free-energy profile would be compared to the conductance from the real experiment.

Generally, our well-equilibrated M_2-TMD structures have several of the structural features observed in NMR and X-ray studies. We discovered that the Trp^{41} side-chains could function as a steric gate for ion passage. Based on PMF results, Cl^- ions have a higher permeability in the M_2-TMD channel than either Na^+ or NH_4^+ ions, and NH_4^+ ions have a higher permeability than Na^+ ions. A revised conductance mechanism is proposed, in which the His^{37} side-chain functions as an acceptor and donor group, and the Trp^{41} side-chain functions as a carrying group that flips from sterically closed to sterically opened state during the process. The sterically open state could allow small anion and cation passage if it lasts long enough. Based on this mechanism, the shutter function of the Trp^{41} side-chains would have to have a short lifetime to prevent the flow of non-proton ions.

However, if under some circumstances the lifetime is prolonged, moderate amounts of non-proton ions might flow causing a reduction in the extremely tight Chizhmakov selectivity.

However, the proposed conductance mechanism requires further studies as well as the conformations of the selectivity-filter side-chains. For instance, what is the lifetime for the proposed transition state? Is this mechanism reversible? How can we simulate H^+–π interactions and the migration process? What is the favorable rotamer for His^{37} side-chains when the M_2-TMD is in the closed form? What are the anion and cation PMFs when all His^{37} and Trp^{41} side-chains are restrained to represent the closed and opened forms? What is the hydronium PMF, when all His^{37} and Trp^{41} side-chains are restrained to represent the closed and opened forms, compared to the H^+ PMF result from MS-EVB simulations? What is the estimated conductance from the free-energy profile compared to the conductance from the real experiment?

From the work in this dissertation, it is clear that great care must be paid to indirect effects of force fields on long-range structural changes. Long-range structural changes have a strong impact on the free-energy profile for ion transport, which include effects of side-chains on channel structure, the water inside the channel, and the neighboring lipid molecules. In the M_2-TMD channel, both His^{37} and Trp^{41} side-chains have unexpected importance. In the TgA channel, both SO_3^- group effects on the water inside the channel and the shielding of SO_3^- group by bulk cations represent difficult challenges for estimating a correct PMF. Nevertheless, our molecular simulations have significantly illuminated the ion transport process.

Appendix A

Published Work Performed During the Period of the Research in this Dissertation

A.1 Monte Carlo Simulation of the Double Layer at an Electrode Including the Effect of a Dielectric Boundary

Alawneh, Morad; Henderson, Douglas. Monte Carlo Simulation of the Double Layer at an Electrode Including the Effect of a Dielectric Boundary. *Molecular Simulation*. 2007;**33**(6):541–547.

Abstract: Monte Carlo values of the density profiles and related properties of the double layer formed by an electrolyte near a charged electrode are reported for the cases where the electrode has a dielectric coefficient greater, equal, and smaller than that of the electrolyte that causes a surface polarization that can be represented by electrostatic images. As expected, compared to the case where there is no dielectric boundary the ions near the electrode are attracted or repelled by the electrode if the dielectric coefficient is greater or smaller, respectively, than that of the electrolyte.

This effect is most pronounced near the electrode and is stronger for 2:2 electrolytes than for 1:1 electrolytes. For both monovalent and divalent ions the effect of the dielectric boundary is stronger at low concentrations.

A.2 A Modified Poisson-Boltzmann Theory and Monte Carlo Simulation Study of Surface Polarization Effects in the Planar Diffuse Double Layer

Bhuiyan, Lutful Bari; Outhwaite, Christopher W.; Henderson, Douglas; Alawneh, Morad. A Modified Poisson-Boltzmann Theory and Monte Carlo Simulation Study of Surface Polarization Effects in the Planar Diffuse Double Layer. *Molecular Physics*. 2007;**105**(10):1395–1402.

Abstract: The equilibrium structural properties of an electric double layer in the presence of a dielectric discontinuity at a plane charged interface are studied through a modified PoissonBoltzmann equation and some Monte Carlo simulations. The diffuse double layer is modeled by a symmetric valency restricted primitive model electrolyte next to a uniformly charged planar wall whose relative permittivity (ε_w) is, in general, different from that of the electrolyte (ε_r) leading to polarization or image forces. The situations when the wall is a conductor ($\varepsilon_w \to \infty$, $\varepsilon_w \neq \varepsilon_r$), or when the wall is an insulator ($\varepsilon_w = 1$, $\varepsilon_w \neq \varepsilon_r$) are treated and contrasted with the case $\varepsilon_w = \varepsilon_r$, that is, no imaging. The results show that the influence of image forces on the diffuse double layer structure can be substantial, especially at or near zero surface charge density. The theoretical predictions are in nearly quantitative agreement for 1:1 salts or in semi-quantitative or better agreement for 2:2 salts with existing Monte Carlo simulations in the literature and some new simulations presented here.

A.3 Application of a Recently Proposed Test to the Hypernetted Chain Approximation for the Electric Double Layer

Henderson, Douglas; Alawneh, Morad; Saavedra-Barrera, Rafael; Lozada-Cassou, Marcelo. Application of a Recently Proposed Test to the Hypernetted Chain Approximation for the Electric

Double Layer. *Condensed Matter Physics*. 2007;**10**(3(51)):323-330.

Abstract: Bhuiyan, Outhwaite, and Henderson, *J. Electroanal. Chem.*, 2007, **607**, 54, have studied the electric double layer formed by a symmetric electrolyte in the restricted primitive model and suggested that an examination of the product of the coion and counterion profiles, normalized to the one when the distance of an ion from the electrode is large, is an interesting and useful test of a theory. This product is identically one in the Poisson-Boltzmann theory but simulation results show that, at contact, this product can be greater or smaller than one at small electrode charge but always seems to tend to zero at large electrode charge. In this study we report the results of the hypernetted chain approximation (HNC/MSA version) for this product and find that, at contact, for this theory this product is always greater than the one at small electrode charge but tends to zero at large electrode charge.

A.4 The Effect of Dielectric Polarization of the Electrode on Anomalous Temperature effects in the Electrical Double Layer

Alawneh, Morad; Henderson, Douglas; Outhwaite, Christopher W.; Bhuiyan, Lutful Bari. The Effect of Dielectric Polarization of the Electrode on Anomalous Temperature effects in the Electrical Double Layer. *Molecular Simulation.* 2007;**33**(15):1279–1284.

Abstract: Monte Carlo simulations and a modified PoissonBoltzmann (MPB) theory are used to investigate the temperature dependence of the capacitance (around the potential of zero charge) of an electric double layer in the presence of surface polarization due to a dielectric boundary. Within the context of the restricted primitive model planar double layer, whose solvent dielectric constant is ε_2, the cases when the electrode is an insulator ($\varepsilon_1 = 1$), when the electrode and the electrolyte have the same permittivity ($\varepsilon_1 = \varepsilon_2$, no polarization), and when the electrode is a conductor ($\varepsilon_1 \to \infty$) are studied for the case where the electrolyte concentration is 0.1 M. The simulations reveal a capacitance anomaly, that is, a positive temperature dependence of the capacitance at low temperatures for the former two situations. The MPB theory also shows this effect for these two situations and is in qualitative or better agreement with the simulation data. In these two cases, both the simulations

and theory show a dramatic increase of the diffuse layer potential in the temperature regime where capacitance anomaly occurs. However, in the latter situation, where the electrode is metallic, the capacitance always has a negative temperature derivative for the MPB theory and probably also for the simulation data.

A.5 A Further Monte Carlo and Modified Poisson-Boltzmann Analysis of Two Recent Results in the Electric Double Layer Theory

Bhuiyan, Lutful Bari; Outhwaite, Christopher W.; Henderson, Douglas; Alawneh, Morad. A Further Monte Carlo and Modified Poisson-Boltzmann Analysis of Two Recent Results in the Electric Double Layer Theory. *Bangladesh Journal of Physics*. 2007;**4**:93–102.

Abstract: Monte Carlo simulation techniques and a modified Poisson-Boltzmann theory are employed to further examine some recent ideas involving the contact values of the electrode-ion density profiles in an electric double layer formed by a valency and size symmetric electrolyte next to a uniformly charged, planar hard wall. Specifically, the behaviour of (i) the product of the contact values of the counterion and coion density profiles, and (ii) the difference of these profiles (related to a simple formula for the contact value of the charge profile), as functions of the surface charge density on the electrode, are investigated at room temperature and at conditions apropos of electrolyte solution regime. The simulations reaffirm the trends for these quantities seen in recent literature, while the modified Poisson-Boltzmann theory is quite successful in predicting the simulation results.

A.6 Molecular Dynamics Results for the Radial Distribution Functions of Highly Asymmetric Hard Sphere Mixtures

Alawneh, Morad; Henderson, Douglas. Molecular Dynamics Results for the Radial Distribution Functions of Highly Asymmetric Hard Sphere Mixtures. *Molecular Physics*. 2008;**106**(6):607–614.

Abstract: Molecular dynamics (MD) results for the radial distribution functions of mixtures of large and small hard spheres are reported for size ratios whose (large/small) values are 1, 2.5, 5, 7.5,

and 10 in the region where the concentration of the large spheres is very small. The MD contact values of these functions are compared with formulae due to Boublik, Mansoori, Carnahan, Starling, Leland, Grundke, and Henderson, Viduna and Smith, Henderson, Trokhymchuk, Woodcock, and Chan, as well as new formulae that are considered here. The new formulae give good agreement for the largesmall contact values and reasonably good agreement for the largelarge contact values. The VidunaSmith formula is satisfactory for the smallsmall contact value and quite reasonable for the smalllarge contact value. Undoubtedly, further improvements are possible. These results give insight into what may be called the colloidal limit, where the size ratio is exceedingly large while the concentration of the large spheres is exceedingly small, and into the passage to this limit.

Appendix B

Presented Work at Scientific Meetings

B.1 Biophysical Society (51st Annual Meeting)

Alawneh, Morad; Busath, David; Henderson, Douglas. March 3–7, 2008. Baltimore, MD, USA.

- **Talk Title:** MD Simulations of Influenza A M_2 using Different Cation Sizes in a Lipid Bilayer.
- **Poster Title:** MD Simulations of Gramicidin A and Taurine Gramicidin A in a Lipid Bilayer.

B.2 Telluride Science Research Center (Ion Channel Biophysics)

Alawneh, Morad; Busath, David; Henderson, Douglas. July 30 – August 3, 2008. Telluride, CO, USA.

- **Talk Title:** A Comparative Study of Tryptophan Force Fields with Experiment Using MD Simulations.

- **Talk Title:** Studying the Influenza M_2 Channel Occupancy by other Ions Using MD Simulations.

B.3 Biophysical Society (52nd Annual Meeting)

Alawneh, Morad; Busath, David; Henderson, Douglas. February 2–6, 2008. Long Beach, CA, USA.

- **Poster Title:** CMAP Helps Solve the Gramicidin Problem.

B.4 Joint Northwest and Rocky Mountain Regional Meeting of the American Chemical Society

Alawneh, Morad; Busath, David. June 15–18, 2008. Park City, UT, USA.

- **Talk Title:** Molecular Dynamics Simulations of Na^+ Transport Free-Energy Profile for Gramicidin and Two Analogs.

Appendix C

Dissertation Work Status

The dissertation work has been submitted for publication and is under review. Both Chapter 2 and 4 have been submitted to Proteins: Structure, Function, and Bioinformatics; whereas Chapter 3 has been submitted to Journal of Physical Chemistry B.

Bibliography

(1) Allen, M.P.; Tildesley, D.J. *Computer Simulation of Liquids*. New York, NY: Oxford University Press; 1987.

(2) Frenkel, D.; Smit, B. *Understanding Molecular Simulation: From Algorithms to Applications*. 2nd ed. San Diego, CA, USA: Academic Press; 2002.

(3) Norberg, J.; Nilsson, L. High-Pressure Molecular-Dynamics of a Nucleic-Acid Fragment. *Chem Phys Lett*. 1994;**24**(1-2):219–224.

(4) Ramanan, H.; Auerbach, S.M.; Tsapatsis, M. Beyond Lattice Models of Activated Transport in Zeolites: High-Temperature Molecular Dynamics of Self-Diffusion and Cooperative Diffusion of Benzene in NaX. *J Phys Chem B*. 2004;**108**(44):17171–17178.

(5) Levine, I.N. *Quantum Chemistry*. 5th ed. Upper Saddle River, NJ: Prentice Hall; 1999.

(6) Karplus, M.; Petsko, G.A. Molecular Dynamics Simulations in Biology. *Nature*. 1990; **347**:631–639.

(7) Sansom, M.S.P.; Forrest, L.R.; Bull, R. Viral Ion Channels: Molecular Modeling and Simulation. *Bioessays*. 1998;**20**(12):992–1000.

(8) Townsley, L.E.; Tucker, W.A.; Sham, S.; Hinton, J.F. Structures of Gramicidins A, B, and C Incorporated into Sodium Dodecyl Sulfate Micelles. *Biochemistry*. 2001;**40**(39):11676–11686.

(9) Nishimura, K.; Kim, S.; Zhang, L.; Cross, T.A. The Closed State of a H^+ Channel Helical Bundle Combining Precise Orientational and Distance Restraints from Solid State NMR. *Biochemistry*. 2002;**41**(44):13170–13177.

(10) Roux, B. The Calculation of the Potential of Mean Force Using Computer Simulations. *Comput Phys Commun*. 1995;**91**(1-3):275–282.

(11) Allen, T.W.; Andersen, O.S.; Roux, B. Ion Permeation through a Narrow Channel: Using Gramicidin to Ascertain All-Atom Molecular Dynamics Potential of Mean Force Methodology and Biomolecular Force Fields. *Biophys J*. 2006;**90**(10):34473468.

(12) MacKerell, A.D., Jr.; Feig, M.; Brooks, C.L., III. Extending the Treatment of Backbone Energetics in Protein Force Fields: Limitations of Gas-Phase Quantum Mechanics in Reproducing Protein Conformational Distributions in Molecular Dynamics Simulations. *J Comput Chem*. 2004;**25**(11):1400–1415.

(13) Hille, B. *Ion Channels of Excitable Membranes*. 3rd ed. Sunderland, MA: Sinauer Associates Inc; 2001.

(14) Doyle, D.A.; Cabral, J.a.M.; Pfuetzner, R.A.; Kuo, A.; Gulbis, J.M.; Cohen, S.L.; Chait, B.T.; MacKinnon, R. The Structure of the Potassium Channel: Molecular Basis of K^+ Conduction and Selectivity. *Science*. 1998;**280**(5360):69–77.

(15) Catterall, W.A. From Ionic Currents to Molecular Mechanisms the Structure and Function of Voltage-Gated Sodium Channels. *Neuron*. 2000;**26**(1):13–25.

(16) Kuyucak, S.; Andersen, O.S.; Chung, S.H. Models of Permeation in Ion Channels. *Rep Prog Phys*. 2001;**64**(11):1011–1021.

(17) Yamakage, M.; Namiki, A. Calcium Channels – Basic Aspects of their Structure, Function and Gene Encoding; Anesthetic Action on the Channels – a Review. *Can J Anesth*. 2002; **49**(2):151–164.

(18) Catterall, W.A.; Goldin, A.L.; Waxman, S.G. International Union of Pharmacology. XLVII. Nomenclature and Structure-Function Relationships of Voltage-Gated Sodium Channels. *Pharmacol Rev*. 2005;**57**(4):397–409.

(19) Nonner, W.; Catacuzzeno, L.; Eisenberg, B. Binding and Selectivity in L-Type Calcium Channels: A Mean Spherical Approximation. *Biophys J*. 2000;**79**(4):1976–1992.

(20) Boda, D.; Valiskó, M.; Eisenberg, B.; Nonner, W.; Henderson, D.; Gillespie, D. The Effect of Protein Dielectric Coefficient on the Ionic Selectivity of a Calcium Channel. *J Chem Phys*. 2006;**125**(3):034901.

(21) Boda, D.; Nonner, W.; Valiskó, M.; Henderson, D.; Eisenberg, B.; Gillespie, D. Steric Selectivity in Na Channels Arising from Protein Polarization and Mobile Side Chains. *Biophys J*. 2007;**93**(6):1960–1980.

(22) Boda, D.; Valiskó, M.; Eisenberg, B.; Nonner, W.; Henderson, D.; Gillespie, D. Combined Effect of Pore Radius and Protein Dielectric Coefficient on the Selectivity of a Calcium Channel. *Phys Rev Lett*. 2007;**98**(16):168102.

(23) Boda, D.; Nonner, W.; Henderson, D.; Eisenberg, B.; Gillespie, D. Volume Exclusion in Calcium Selective Channels. *Biophys J*. 2008;**94**(9):3486–3496.

(24) Corry, B.; Allen, T.W.; Kuyucak, S.; Chung, S.H. Mechanisms of Permeation and Selectivity in Calcium Channels. *Biophys J*. 2001;**80**(1):195–214.

(25) Corry, B.; Kuyucak, S.; Chung, S.H. Dielectric Self-Energy in Poisson-Boltzmann and Poisson-Nernst-Planck Models of Ion Channels. *Biophys J*. 2003;**84**(6):3594–3606.

(26) Corry, B.; Vorab, T.; Chung, S.H. Electrostatic Basis of Valence Selectivity in Cationic Channels. *Biochim Biophys Acta Biomembr*. 2005;**1711**(1):72–86.

(27) Vora, T.; Corry, B.; Chung, S.H. A Model of Sodium Channels. *Biochim Biophys Acta Biomembr*. 2005;**1668**(1):106–116.

(28) Chung, S.H.; Corry, B. Conduction Properties of KcsA Measured Using Brownian Dynamics with Flexible Carbonyl Groups in the Selectivity Filter. *Biophys J*. 2007;**93**(1):44–53.

(29) Yang, Y.; Henderson, D.; Crozier, P.; Rowley, R.L.; Busath, D.D. Permeation of Ions through a Model Biological Channel: Effect of Periodic Boundary Conditions and Cell Size. *Mol Phys*. 2002;**100**(18):3011–3019.

(30) Yang, Y.; Henderson, D.; Busath, D. Applied-Field Molecular Dynamics Study of a Model Calcium Channel Selectivity Filter. *J Chem Phys*. 2003;**118**(9):4213–4220.

(31) Yang, Y.; Henderson, D.; Busath, D.D. Calcium Block of Sodium Current in a Model Calcium Channel: Cylindrical Atomistic Pore with Glutamate Side Chains. *Mol Simul*. 2004; **30**(2-3):75–80.

(32) Roeske, R.W.; Hrinyo-Pavlina, T.P.; Pottorf, R.S.; T., B.; Jin, X.Z.; Busath, D. Synthesis and Channel Properties of [Tau^{16}]gramicidin A. *Biochim Biophys Acta*. 1989;**982**(2):223–227.

(33) Chizhmakov, I.V.; Geraghty, F.M.; Ogden, D.C.; Hayhurst, A.; Antoniou, M.; Hay, A.J. Selective Proton Permeability and pH Regulation of the Influenza Virus M2 Channel Expressed in Mouse Erythroleukaemia Cells. *J Physiol*. 1996;**494**(2):329–336.

(34) Lin, T.I.; Schroeder, C. Definitive Assignment of Proton Selectivity and Attoampere Unitary Current to the M2 Ion Channel Protein of Influenza A Virus. *J Virol*. 2001;**75**(8):3647–3656.

(35) Mould, J.A.; Drury, J.E.; Frings, S.M.; Kaupp, U.B.; Pekosz, A.; Lamb, R.A.; Pinto, L.H. Permeation and Activation of the M_2 Ion Channel of Influenza A Virus. *J Biol Chem*. 2000; **275**(40):31038–31050.

(36) Chizhmakov, I.V.; Ogden, D.C.; Geraghty, F.M.; Hayhurst, A.; Skinner, A.; Betakova, T.; Hay, A.J. Differences in Conductance of M2 Proton Channels of Two Influenza Viruses at Low and High pH. *J Physiol*. 2003;**546**(2):427–438.

(37) Pinto, L.H.; Holsinger, L.J.; Lamb, R.A. Influenza Virus M_2 Protein Has Ion Channel Activity. *Cell*. 1992;**69**(3):517–528.

(38) Tosteson, M.T.; Pinto, L.H.; Holsinger, L.J.; Lamb, R.A. Reconstitution of the Influenza Virus M2 Ion Channel in Lipid Bilayers. *J Mol Biol*. 1994;**142**(1):117–126.

(39) Wang, C.; Lamb, R.A.; Pinto, L.H. Activation of the M_2 Ion Channel of Influenza Virus: A Role for the Transmembrane Domain Histidine Residue. *Biophys J*. 1995;**69**(4):1363–1371.

(40) Shimbo, K.; Brassard, D.L.; Lamb, R.A.; Pinto, L.H. Ion Selectivity and Activation of the M2 Ion Channel of Influenza Virus. *Biophys J*. 1996;**70**(3):1335–1346.

(41) Tang, Y.; Zaitseva, F.; Lamb, R.A.; Pinto, L.H. The Gate of the Influenza Virus M_2 Proton Channel Is Formed by a Single Tryptophan Residue. *J Biol Chem*. 2002;**277**(42):39880–39886.

(42) Israelachvili, J.N. *Intermolecular and Surface Forces*. San Diego, CA, USA: Academic Press; 1992.

(43) Errington, J.R.; Kofke, D.A. Calculation of Surface Tension via Area Sampling. *J Chem Phys*. 2007;**127**(17):174709.

(44) Arseniev, A.S.; Barsukov, I.L.; Bystrov, V.F. NMR Solution Structure of Gramicidin A Complex with Caesium Cations. *FEBS Lett*. 1985;**180**(1):33–39.

(45) Urry, D.W. The Gramicidin A Transmembrane Channel: A Proposed $\pi_{(L,D)}$ Helix. *Proc Natl Acad Sci USA*. 1971;**68**(3):672–676.

(46) Urry, D.W.; Goodall, M.C.; Glickson, J.D.; Mayers, D.F. The Gramicidin A Transmembrane Channel: Characteristics of Head-to-Head Dimerized $\pi_{(L,D)}$ Helices. *Proc Natl Acad Sci USA*. 1971;**68**(8):1907–1911.

(47) Sarges, R.; Witkop, B. Gramicidin A. V. The Structure of Valine- and Isoleucine-Gramicidin A. *J Am Chem Soc*. 1965;**87**(9):2011–2020.

(48) Koeppe, R.E., II; Anderson, O.S. Engineering the Gramicidin Channel. *Annu Rev Biophys Biomol Struct*. 1996;**25**:231–258.

(49) Kelkar, D.A.; Chattopadhyay, A. The Gramicidin Ion Channel: A Model Membrane Protein. *Biochim Biophys Acta Biomembr*. 2007;**1768**(9):2011–2025.

(50) Bamberg, E.; Apell, H.J.; Alpes, H.; Gross, E.; Morell, J.L.; Harbaugh, J.F.; Janko, K.; Läuger, P. Ion Channels Formed by Chemical Analogs of Gramicidin A. *Fed Proc*. 1978; **37**(12):2633–2638.

(51) Prasad, K.U.; Trapane, T.L.; Busath, D.; Szabo, G.; Urry, D.W. Synthesis and Characterization of (1-13c) Phe9 Gramicidin A. Effects of Side Chain Variations. *Int J Pept Protein Res*. 1983;**22**(3):341–347.

(52) Heitz, F.; Gavach, C.; Spach, G.; Trudelle, Y. Analysis of the Ion Transfer through the Channel of 9,11,13,15-Phenylalanylgramicidin A. *Biophys Chem*. 1986;**24**(2):143–148.

(53) Busath, D.D.; Hayon, E. Ultraviolet Flash Photolysis of Gramicidin-Doped Lipid Bilayers. *Biochim Biophys Acta*. 1988;**944**(1):73–78.

(54) Scarlata, S.F. The Effects of Viscosity on Gramicidin Tryptophan Rotational Motion. *Biophys J*. 1988;**54**(6):1149–1157.

(55) Takeuchi, H.; Nemoto, Y.; Harada, I. Environments and Conformations of Tryptophan Side Chains of Gramicidin A in Phospholipid Bilayers Studied by Raman Spectroscopy. *Biochemistry*. 1990;**29**(6):1572–1579.

(56) Becker, M.D.; Greathouse, D.V.; Koeppe, R.E.; Andersen, O.S. Amino Acid Sequence Modulation of Gramicidin Channel Function: Effects of Tryptophan-to-Phenylalanine Substitutions on the Single-Channel Conductance and Duration. *Biochemistry*. 1991;**30**(36):8830–8839.

(57) Daumas, P.; Benamar, D.; Heitz, F.; Ranjalahyrasoloarijao, L.; Mouden, R.; Lazaro, R.; Pullman, A. How Can the Aromatic Side-Chains Modulate the Conductance of the Gramicidin Channel – a New Approach Using Non-Coded Amino-Acids. *Int J Pept Protein Res*. 1991; **38**(3):218–228.

(58) Fonseca, V.; Daumas, P.; Ranjalahy-Rasoloarijao, L.; Heitz, F.; Lazaro, R.; Trudelle, Y.; Andersen, O.S. Gramicidin Channels that have no Tryptophan Residues. *Biochemistry*. 1992;**31**(23):5340–5350.

(59) Mukherjee, S.; Chattopadhyay, A. Motionally Restricted Tryptophan Environments at the Peptide-Lipid Interface of Gramicidin Channels. *Biochemistry*. 1994;**33**(17):5089–5097.

(60) Seoh, S.A.; Busath, D.D. Gramicidin Tryptophans Mediate Formamidinium-Induced Channel Stabilization. *Biophys J*. 1995;**68**(6):22712279.

(61) Woolf, T.B.; Roux, B. Structure, Energetics, and Dynamics of Lipid-Protein Interactions: A Molecular Dynamics Study of the Gramicidin A Channel in a DMPC Bilayer. *Proteins*. 1996;**24**(1):92–114.

(62) Chiu, S.W.; Subramaniam, S.; Jakobsson, E. Simulation Study of a Gramicidin/Lipid Bilayer System in Excess Water and Lipid. I. Structure of the Molecular Complex. *Biophys J*. 1999; **76**(4):1929–1938.

(63) Kóta, Z.; Páli, T.; Marsh, D. Orientation and Lipid-Peptide Interactions of Gramicidin A in Lipid Membranes: Polarized Attenuated Total Reflection Infrared Spectroscopy and Spin-Label Electron Spin Resonance. *Biophys J*. 2004;**86**(3):1521–1531.

(64) Petersen, F.N.R.; Jensen, M.Ø.; Nielsen, C.H. Interfacial Tryptophan Residues: A Role for the Cation-π Effect? *Biophys J*. 2005;**89**(6):3985–3996.

(65) Hu, W.; Lazo, N.D.; Cross, T.A. Tryptophan Dynamics and Structural Refinement in a Lipid Bilayer Environment: Solid State NMR of the Gramicidin Channel. *Biochemistry*. 1995; **34**(43):14138–14146.

(66) Hu, W.; Cross, T.A. Tryptophan Hydrogen Bonding and Electric Dipole Moments: Functional Roles in the Gramicidin Channel and Implications for Membrane Proteins. *Biochemistry*. 1995;**34**(43):14147–14155.

(67) Busath, D.D.; Thulin, C.D.; Hendershot, R.W.; Phillips, L.R.; Maughan, P.; Cole, C.D.; Bingham, N.C.; Morrison, S.; Baird, L.C.; Hendershot, R.J.; et al. Noncontact Dipole Effects on Channel Permeation. I. Experiments with (5F-Indole)Trp^{13} Gramicidin A Channels. *Biophys J*. 1998;**75**(6):2830–2844.

(68) Andersen, O.S.; Greathouse, D.V.; Providence, L.L.; Becker, M.D.; Koeppe, R.E., II. Importance of Tryptophan Dipoles for Protein Function: 5-Fluorination of Tryptophans in Gramicidin A Channels. *J Am Chem Soc*. 1998;**120**(21):5142–5146.

(69) Dorigo, A.E.; Anderson, D.G.; Busath, D.D. Noncontact dipole effects on channel permeation. ii. trp conformations and dipole potentials in gramicidin a. *Biophys J*. 1999; **76**(4):18971908.

(70) Cotten, M.; Tian, C.; Busath, D.D.; Shirts, R.B.; Cross, T.A. Modulating Dipoles for Structure-Function Correlations in the Gramicidin A Channel. *Biochemistry*. 1999; **38**(29):9185–9197.

(71) Phillips, L.R.; Cole, C.D.; Hendershot, R.J.; Cotten, M.; Cross, T.A.; Busath, D.D. Noncontact Dipole Effects on Channel Permeation. III. Anomalous Proton Conductance Effects in Gramicidin. *Biophys J*. 1999;**77**(5):2492–2501.

(72) Anderson, D.G.; Shirts, R.B.; Cross, T.A.; Busath, D.D. Noncontact Dipole Effects on Channel Permeation. V. Computed Potentials for Fluorinated Gramicidin. *Biophys J*. 2001; **81**(3):1255–1264.

(73) Thompson, N.; Thompson, G.; Cole, C.D.; Cotten, M.; Cross, T.A.; Busath, D.D. Noncontact Dipole Effects on Channel Permeation. IV. Kinetic Model of 5F-Trp$_{13}$ Gramicidin A Currents. *Biophys J*. 2001;**81**(3):12451254.

(74) Cole, C.D.; Frost, A.S.; Thompson, N.; Cotten, M.; Cross, T.A.; Busath, D.D. Noncontact Dipole Effects on Channel Permeation. VI. 5F- and 6F-Trp Gramicidin Channel Currents. *Biophys J*. 2002;**83**(4):1974–1986.

(75) Gowen, J.A.; Markham, J.C.; Morrison, S.E.; Cross, T.A.; Busath, D.D.; Mapes, E.J.; Schumaker, M.F. The role of trp side chains in tuning single proton conduction through gramicidin channels. *Biophys J*. 2002;**83**(2):880–898.

(76) Hemsley, G.; Busath, D. Small Iminium Ions Block Gramicidin Channels in Lipid Bilayers. *Biophys J*. 1991;**59**(4):901907.

(77) Patra, S.M.; Baştuğ, T.; Kuyucak, S. Binding of Organic Cations to Gramicidin A Channel Studied with Autodock and Molecular Dynamics Simulations. *J Phys Chem B*. 2007; **111**(38):11303–11311.

(78) Durrant, J.D.; Caywood, D.; Busath, D.D. Tryptophan Contributions to the Empirical Free-Energy Profile in Gramicidin A/M Heterodimer Channels. *Biophys J*. 2006;**91**(9):3230–3241.

(79) Woolf, T.B.; Roux, B. The Binding Site of Sodium in the Gramicidin A Channel: Comparison of Molecular Dynamics with Solid-State NMR Data. *Biophys J*. 1997;**92**(5):1930–1945.

(80) Allen, T.W.; Andersen, O.S.; Roux, B. Molecular Dynamics — Potential of Mean Force Calculations as a Tool for Understanding Ion Permeation and Selectivity in Narrow Channels. *Biophys Chem*. 2006;**124**(3):251–267.

(81) Macias, A.T.; MacKerell, A.D., Jr. Ch/π Interactions Involving Aromatic Amino Acids: Refinement of the CHARMM Tryptophan Force Field. *J Comput Chem*. 2005;**26**(14):1452–1463.

(82) Roux, B.; Karplus, M. Ion Transport in the Gramicidin Channel: Free Energy of the Solvated Right-Handed Dimer in a Model Membrane. *J Am Chem Soc*. 1993;**115**(8):3250–3262.

(83) Allen, T.W.; Baştuğ, T.; Kuyucak, S.; Chung, S.H. Gramicidin A Channel as a Test Ground for Molecular Dynamics Force Fields. *Biophys J*. 2003;**84**(4):2159–2168.

(84) Allen, T.W.; Andersen, O.S.; Roux, B. Energetics of Ion Conduction through the Gramicidin Channel. *Proc Natl Acad Sci USA*. 2004;**101**(1):117–122.

(85) Baştuğ, T.; Kuyucak, S. Test of Molecular Dynamics Force Fields in Gramicidin A. *Eur Biophys J*. 2005;**34**(5):377–382.

(86) Baştuğ, T.; Patra, S.M.; Kuyucak, S. Molecular Dynamics Simulations of Gramicidin A in a Lipid Bilayer: From Structure-Function Relations to Force Fields. *Chem Phys Lipids*. 2006; **141**(1-2):197–204.

(87) Baştuğ, T.; Gray-Weale, A.; Patra, S.M.; Kuyucak, S. Role of Protein Flexibility in Ion Permeation: A Case Study in Gramicidin A. *Biophys J*. 2006;**90**(7):2285–2296.

(88) Baştuğ, T.; Kuyucak, S. Energetics of Ion Permeation, Rejection, Binding, and Block in Gramicidin A from Free Energy Simulations. *Biophys J*. 2006;**90**(11):3941–3950.

(89) Baştuğ, T.; Kuyucak, S. Free Energy Simulations of Single and Double Ion Occupancy in Gramicidin A. *J Chem Phys*. 2007;**126**(10):105103.

(90) Ketchem, R.R.; Lee, K.C.; Huo, S.; Cross, T.A. Macromolecular Structural Elucidation with Solid-State NMR-Derived Orientational Constraints. *J Biomol NMR*. 1996;**8**(1):1–14.

(91) Edwards, S.; Corry, B.; Kuyucak, S.; Chung, S.H. Continuum Electrostatics Fails to Describe Ion Permeation in the Gramicidin Channel. *Biophys J*. 2002;**83**(3):13481360.

(92) Roux, B.; Karplus, M. Ion Transport in a Model Gramicidin Channel. Structure and Thermodynamics. *Biophys J*. 1991;**59**(5):961–981.

(93) Hao, Y.; Pear, M.R.; Busath, D.D. Molecular dynamics study of free energy profiles for organic cations in gramicidin a channels. *Biophys J*. 1997;**73**(4):1699–1716.

(94) Allen, T.W.; Andersen, O.S.; Roux, B. Structure of Gramicidin A in a Lipid Bilayer Environment Determined Using Molecular Dynamics Simulations and Solid-State NMR Data. *J Am Chem Soc*. 2003;**125**(32):9868–9877.

(95) Jorgensen, W.L.; Chandrasekhar, J.; Madura, J.D.; Impey, R.W.; Klein, M.L. Comparison of Simple Potential Functions for Simulating Liquid Water. *J Chem Phys*. 1983;**79**(2):926–935.

(96) Humphrey, W.; Dalke, A.; Schulten, K. VMD: Visual Molecular Dynamics. *J Mol Graphics*. 1996;**14**(1):33–38.

(97) Chiu, S.W.; Clark, M.; Balaji, V.; Subramaniam, S.; Scott, H.L.; Jakobsson, E. Incorporation of Surface Tension into Molecular Dynamics Simulation of an Interface: A Fluid Phase Lipid Bilayer Membrane. *Biophys J*. 1995;**69**(4):1230–1245.

(98) Zhang, Y.; Feller, S.E.; Brooks, R.W.; Pastor, R.W. Computer Simulation of Liquid/Liquid Interfaces. I. Theory and Application to Octane/Water. *J Chem Phys*. 1995;**103**(23):10252–10266.

(99) Feller, S.E.; Zhang, Y.; Pastor, R.W. Computer Simulation of Liquid/Liquid Interfaces. II. Surface Tension-Area Dependence of a Bilayer and Monolayer. *J Chem Phys*. 1995; **103**(23):10267–10276.

(100) Feller, S.E.; Pastor, R.W. Constant Surface Tension Simulations of Lipid Bilayers: The Sensitivity of Surface Areas and Compressibilities. *J Chem Phys*. 1999;**111**(3):1281–1287.

(101) Koenig, B.W.; Strey, H.H.; Gawrisch, K. Membrane Lateral Compressibility Determined by NMR and X-ray Diffraction: Effect of Acyl Chain Polyunsaturation. *Biophys J*. 1997; **73**(4):1954–1966.

(102) Takaoka, Y.; Pasenkiewicz-Gierula, M.; Miyagawa, H.; Kitamura, K.; Tamura, Y.; Kusumi, A. Molecular Dynamics Generation of Nonarbitrary Membrane Models Reveals Lipid Orientational Correlations. *Biophys J*. 2000;**79**(6):3118–3138.

(103) Högberg, C.J.; Lyubartsev, A.P. A Molecular Dynamics Investigation of the Influence of Hydration and Temperature on Structural and Dynamical Properties of a Dimyristoylphosphatidylcholine Bilayer. *J Phys Chem B*. 2006;**110**(29):14326–14336.

(104) Petrache, H.I.; Tristram-Nagle, S.; Harries, D.; Kučerka, N.; Nagle, J.F.; Parsegian, V.A. Swelling of Phospholipids by Monovalent Salt. *J Lipid Res*. 2006;**47**(2):302–309.

(105) Feller, S.E.; Pastor, R.W. On Simulating Lipid Bilayers with an Applied Surface Tension: Periodic Boundary Conditions and Undulations. *Biophys J*. 1996;**71**(3):13501355.

(106) Sankararamakrishnan, R.; Weinstein, H. Surface Tension Parameterization in Molecular Dynamics Simulations of a Phospholipid-bilayer Membrane: Calibration and Effects. *J Phys Chem B*. 2004;**108**(31):11802–11811.

(107) Harroun, T.A.; Heller, W.T.; Weiss, T.M.; Yang, L.; Huang, H.W. Experimental Evidence for Hydrophobic Matching and Membrane-Mediated Interactions in Lipid Bilayers Containing Gramicidin. *Biophys J*. 1999;**76**(2):937–945.

(108) Kučerka, N.; Liu, Y.; Chu, N.; Petrache, H.I.; Tristram-Nagle, S.; Nagle, J.F. Structure of Fully Hydrated Fluid Phase DMPC and DLPC Lipid Bilayers Using X-ray Scattering from Oriented Multilamellar Arrays and from Unilamellar Vesicles. *Biophys J*. 2005;**88**(1):2626–2637.

(109) Phillips, J.C.; Braun, R.; Wang, W.; Gumbart, J.; Tajkhorshid, E.; Villa, E.; Chipot, C.; Skeel, R.D.; Kalé, L.; Schulten, K. Scalable Molecular Dynamics with NAMD. *J Comput Chem*. 2005;**26**(16):1781–1802.

(110) MacKerell, A.D., Jr.; Bashford, D.; Bellott, R.L.; Dunbrack, R.L., Jr.; Evanseck, J.D.; Field, M.J.; Fischer, S.; Gao, J.; Guo, H.; Ha, S.; et al. All-Atom Empirical Potential for Molecular Modeling and Dynamics Studies of Proteins. *J Phys Chem B*. 1998;**102**(18):3586–3616.

(111) MacKerell, A.D., Jr.; Feig, M.; Brooks, C.L., III. Improved Treatment of the Protein Backbone in Empirical Force Fields. *J Am Chem Soc*. 2004;**126**(3):698–699.

(112) Beglov, D.; Benoît, R. Finite Representation of an Infinite Bulk System: Solvent Boundary Potential for Computer Simulations. *J Chem Phys*. 1994;**100**(12):9050–9063.

(113) Schlenkrich, M.; Brickmann, J.; MacKerell, A.D., Jr.; Karplus, M. An Empirical Potential Energy Function for Phospholipids: Criteria for Parameter Optimization and Applications. In: Merz, K.M.; Roux, B.; editors. *Biological Membranes: A Molecular Perspective from Computation and Experiment*. Boston, MA: Birkhäuser; 1996. p. 31–81.

(114) Feller, S.E.; MacKerell, A.D., Jr. An Improved Empirical Potential Energy Function for Molecular Simulations of Phospholipids. *J Phys Chem B*. 2000;**104**(31):7510–7515.

(115) Steinbach, P.J.; Brooks, B.R. New Spherical-Cutoff Methods for Long-Range Forces in Macromolecular Simulation. *J Comput Chem*. 1994;**15**(7):667–683.

(116) Martyna, G.J.; Tobias, D.J.; Klein, M.L. Constant Pressure Molecular Dynamics Algorithms. *J Chem Phys*. 1994;**101**(5):4177–4189.

(117) Feller, S.E.; Zhang, Y.; Pastor, R.W.; Brooks, B.R. Constant Pressure Molecular Dynamics Simulation: The Langevin Piston Method. *J Chem Phys*. 1995;**103**(11):4613–4621.

(118) Welch, B.B.; Jones, K.; Hobbs, J. *Practical Programming in Tcl and Tk.* 4th ed. Upper Saddle River, NJ: Prentice Hall PTR; 2003.

(119) Lovell, S.C.; Word, J.M.; Richardson, J.S.; Richardson, D.C. The Penultimate Rotamer Library. *Proteins*. 2000;**40**(3):389–408.

(120) Trzesniak, D.; Kunz, A.P.E.; van Gunsteren, W.F. A Comparison of Methods to Compute the Potential of Mean Force. *ChemPhysChem*. 2007;**8**(1):162–169.

(121) Grossfield, A. An Implementation of WHAM: The weighted histogram analysis method. Available from: http://membrane.urmc.rochester.edu/.

(122) Kumar, S.; Rosenberg, J.M.; Bouzida, D.; Swendsen, R.H.; Kollman, P.A. The Weighted Histogram Analysis Method for Free-Energy Calculations on Biomolecules. I. The Method. *J Comput Chem*. 1992;**13**(8):1011–1021.

(123) Souaille, M.; Roux, B. Extension to the Weighted Histogram Analysis Method: Combining Umbrella Sampling with Free Energy Calculations. *Comput Phys Commun*. 2001;**135**(1):40–57.

(124) Burden, R.L.; Faires, J.D. *Numerical Analysis*. 7th ed. Pacific Grove, CA: Brooks Cole; 2001.

(125) Petrache, H.I.; Dodd, S.W.; Brown, M.F. Area per Lipid and Acyl Length Distributions in Fluid Phosphatidylcholines Determined by ^{2}H NMR Spectroscopy. *Biophys J*. 2000; **79**(6):3172–3192.

(126) Otten, D.; Brown, M.F.; Beyer, K. Softening of Membrane Bilayers by Detergents Elucidated by Deuterium NMR Spectroscopy. *J Phys Chem B*. 2000;**104**(51):12119–12129.

(127) Aussenac, F.; Laguerre, M.; Schmitter, J.M.; Dufourc, E.J. Detailed Structure and Dynamics of Bicelle Phospholipids Using Selectively Deuterated and Perdeuterated Labels. ^{2}H NMR and Molecular Mechanics Study. *Langmuir*. 2003;**19**(25):10468–10479.

(128) Bingham, N.C.; Smith, N.E.C.; Cross, T.A.; Busath, D.D. Molecular Dynamics Simulations of Trp Side-Chain Conformational Flexibility in the Gramicidin A Channel. *Biopolymers*. 2003;**71**(5):593–600.

(129) Duffin, R.L.; Garrett, M.P.; Flake, K.B.; Durrant, J.D.; Busath, D.D. Modulation of Lipid Bilayer Interfacial Dipole Potential by Phloretin, RH421, and 6-Ketocholestanol as Probed by Gramicidin Channel Conductance. *Langmuir*. 2003;**19**(4):1439–1442.

(130) Apell, H.J.; Bamberg, E.; Alpes, H.; Läuger, P. Formation of Ion Channels by a Negatively Charged Analog of Gramicidin A. *J Mol Biol*. 1977;**31**(1):171–188.

(131) Cifu, A.S.; Koeppe, R.E., II; Andersen, O.S. On the Supramolecular Organization of Gramicidin Channels. The Elementary Conducting Unit is a Dimer. *Biophys J*. 1992;**61**(1):189–203.

(132) Woolley, G.A.; Jaikaran, A.S.I.; Zhang, Z.; Peng, S. Design of Regulated Ion Channels Using Measurements of Cis-Trans Isomerization in Single Molecules. *J Am Chem Soc*. 1995; **117**(16):4448–4454.

(133) Capone, R.; Blake, S.; Restrepo, M.R.; Yang, J.; Mayer, M. Designing Nanosensors Based on Charged Derivatives of Gramicidin A. *J Am Chem Soc*. 2007;**129**(31):9737–9745.

(134) Parent, L.; Gopalakrishnan, M. Glutamate Substitution in Repeat IV Alters Divalent and Monovalent Cation Permeation in the Heart Ca^{2+} Channel. *Biophys J*. 1995;**69**(5):1801–1813.

(135) Bahinski, A.; Yatani, A.; Mikala, G.; Tang, S.Q.; Yamamoto, S.; Schwartz, A. Charged Amino Acids Near the Pore Entrance Influence Ion-Conduction of a Human L-type Cardiac Calcium Channel. *Mol Cell Biochem*. 1997;**166**(1-2):125–134.

(136) Zhang, Z.; Xu, Y.; Dong, P.H.; Sharma, D.; Chiamvimonvat, N. A Negatively Charged Residue in the Outer Mouth of Rat Sodium Channel Determines the Gating Kinetics of the Channel. *Am J Physiol Cell Physiol*. 2003;**284**(5):C1247–C1254.

(137) Black, G.; Daily, J.; Didier, B.; Elsethagen, T.; Feller, D.; Gracio, D.; Hackler, M.; Havre, S.; Jones, D.; Jurrus, E.; et al. *ECCE, A Problem Solving Environment for Computational Chemistry, Software Version 4.5.1*. Richland, Washington 99352-0999, USA: Pacific Northwest National Laboratory; 2007.

(138) Kendall, R.A.; Apra, E.; Bernholdt, D.E.; Bylaska, E.J.; Dupuis, M.; Fann, G.I.; Harrison, R.J.; Ju, J.L.; Nichols, J.A.; Nieplocha, J.; et al. High Performance Computational Chemistry: An Overview of NWChem a Distributed Parallel Application. *Comput Phys Commun*. 2000; **128**(1-2):260–283.

(139) Bylaska, E.J.; de Jong, W.A.; Kowalski, K.; Straatsma, T.P.; Valiev, M.; Wang, D.; Aprà, E.; Windus, T.L.; Hirata, S.; Hackler, M.T.; et al. *NWChem, A Computational Chemistry Package for Parallel Computers, Version 5.0*. Richland, Washington 99352-0999, USA: Pacific Northwest National Laboratory; 2006.

(140) Crozier, P.S.; Henderson, D.; Rowley, R.L.; Busath, D.D. Model Channel Ion Currents in NaCl-Extended Simple Point Charge Water Solution with Applied-Field Molecular Dynamics. *Biophys J*. 2001;**81**(6):3077–3089.

(141) Teschke, O.; Ceotto, G.; de Souza, E.F. Interfacial Water Dielectric-Permittivity-Profile Measurements Using Atomic Force Microscopy. *Phys Rev E*. 2001;**64**(1):011605.

(142) Kell, D.B. On the Functional Proton Current Pathway of Electron Transport Phosphorylation: An Electrodic View. *Biochim Biophys Acta*. 1979;**549**(1):55–99.

(143) Cherepanov, D.A.; Feniouk, B.A.; Junge, W.; Mulkidjanian, A.Y. Low Dielectric Permittivity of Water at the Membrane Interface: Effect on the Energy Coupling Mechanism in Biological Membranes. *Biophys J*. 2003;**85**(2):1307–1316.

(144) Antonenko, Y.N.; Pohl, P. Microinjection in Combination with Microfluorimetry to Study Proton Diffusion along Phospholipid Membranes. *Eur Biophys J*. 2008;**37**(6):865–870.

(145) Lamb, R.A.; Zebedee, S.L.; Richardson, C.D. Influenza Virus M_2 Protein is an Integral Membrane Protein Expressed on the Infected-Cell Surface. *Cell*. 1985;**40**(3):627–633.

(146) Zebedee, S.L.; Lamb, R.A. Influenza A Virus M_2 Protein: Monoclonal Antibody Restriction of Virus Growth and Detection of M_2 in Virions. *J Virol*. 1988;**62**(8):2762–2772.

(147) Skehel, J.J.; Bayley, P.M.; Brown, E.B.; Martin, S.R.; Waterfield, M.D.; White, J.M.; Wilson, I.A.; Wiley, D. Changes in the Conformation of Influenza Virus Hemagglutinin at the pH Optimum of Virus-Mediated Membrane Fusion. *Proc Natl Acad Sci USA*. 1982;**79**(4):968–972.

(148) Sugrue, R.J.; Hay, A.J. Structural Characteristics of the M2 Protein of Influenza A Viruses: Evidence that It Forms a Tetrameric Channel. *Virology*. 1991;**180**(2):617–624.

(149) Davies, W.L.; Grunert, R.R.; Haff, R.F.; McGahen, J.W.; Neumayer, E.M.; Paulshock, M.; Watts, J.C.; Wood, T.R.; Hermann, E.C.; Hoffmann, C.E. Antiviral Activity of 1-Adamantanamine (Amantadine). *Science*. 1964;**144**(3620):862–863.

(150) Appleyard, G. Amantadine-Resistance as a Genetic Marker for Influenza Viruses. *J Gen Virol*. 1977;**36**(2):249–255.

(151) Hay, A.J.; Wolstenholme, A.J.; Skehel, J.J.; Smith, M.H. The Molecular Basis of the Specific Anti-influenza Action of Amantadine. *EMBO J*. 1985;**4**(11):3021–3024.

(152) Skehel, J.J. Amantadine Blocks the Channel. *Nature*. 1992;**358**(6382):110–111.

(153) Holsinger, L.J.; Nichani, D.; Pinto, L.H.; Lamb, R.A. Influenza A Virus M_2 Ion Channel Protein: A Structure-Function Analysis. *J Virol*. 1994;**68**(3):1551–1563.

(154) Astrahan, P.; Kass, I.; Cooper, M.A.; Arkin, I.T. A Novel Method of Resistance for Influenza Against a Channel-Blocking Antiviral Drug. *Proteins*. 2004;**55**(2):251–257.

(155) Sugrue, R.J.; Bahadur, G.; Zambon, M.C.; Hall-Smith, M.; Douglas, A.R.; Hay, A.J. Specific Structural Alteration of the Influenza Haemagglutinin by Amantadine. *EMBO J*. 1990; **9**(11):34693476.

(156) Okada, A.; Miura, T.; Takeuchi, H. Protonation of Histidine and Histidine-Tryptophan Interaction in the Activation of the M2 Ion Channel from Influenza A Virus. *Biochemistry*. 2001; **40**(20):6053–6060.

(157) Vijayvergiya, V.; Wilson, R.; Chorak, A.; Gao, P.F.; Cross, T.A.; Busath, D.D. Proton Conductance of Influenza Virus M2 Protein in Planar Lipid Bilayers. *Biophys J*. 2004; **87**(3):1697–1704.

(158) Hu, J.; Fu, R.; Cross, T.A. The Chemical and Dynamical Influence of the Anti-Viral Drug Amantadine on the M_2 Proton Channel Transmembrane Domain. *Biophys J*. 2007;**93**(1):276–283.

(159) Chen, H.; Wu, Y.; Voth, G.A. Proton Transport Behavior through the Influenza A M2 Channel: Insights from Molecular Simulation. *Biophys J*. 2007;**93**(10):3470–3479.

(160) Duff, K.C.; Ashley, R.H. The Transmembrane Domain of Influenza A M2 Protein Forms Amantadine-Sensitive Proton Channels in Planar Lipid Bilayers. *Virology*. 1992;**190**(1):485–489.

(161) Watanabe, T.; Watanabe, S.; Ito, H.; Kida, H.; Kawaoka, Y. Influenza A Virus Can Undergo Multiple Cycles of Replication without M2 Ion Channel Activity. *J Virol*. 2001;**75**(12):5656–5662.

(162) Takeda, M.; Pekosz, A.; Shuck, K.; Pinto, L.H.; Lamb, R.A. Influenza A Virus M_2 Ion Channel Activity Is Essential for Efficient Replication in Tissue Culture. *J Virol*. 2002; **76**(3):1391–1399.

(163) McCown, M.F.; Pekosz, A. Distinct Domains of the Influenza A Virus M2 Protein Cytoplasmic Tail Mediate Binding to the M1 Protein and Facilitate Infectious Virus Production. *J Virol*. 2006;**80**(16):8178–8189.

(164) Iwatsuki-Horimoto, K.; Horimoto, T.; Noda, T.; Kiso, M.; Maeda, J.; Watanabe, S.; Muramoto, Y.; Fujii, K.; Kawaoka, Y. The Cytoplasmic Tail of the Influenza A Virus M2 Protein Plays a Role in Viral Assembly. *J Virol*. 2006;**80**(11):5233–5240.

(165) Holsinger, L.J.; Lamb, R.A. Influenza Virus M_2 Integral Membrane Protein Is a Homotetramer Stabilized by Formation of Disulfide Bonds. *Virology*. 1991;**183**(1):32–43.

(166) Panayotov, P.P.; Schlesinger, R.W. Oligomeric Organization and Strain-Specific Proteolytic Modification of the Virion M2 Protein of Influenza A H1N1 Viruses. *Virology*. 1992; **186**(1):352–355.

(167) Sansom, M.S.P.; Kerr, I.D. Influenza Virus M_2 Protein: A Molecular Modelling Study of the Ion Channel. *Protein Eng*. 1993;**6**(1):65–74.

(168) Wang, J.; Kim, S.; Kovacs, F.; Cross, T.A. Structure of the Transmembrane Region of the M2 protein H^+ Channel. *Protein Sci*. 2001;**10**(11):2241–2250.

(169) Kovacs, F.A.; Cross, T.A. Transmembrane Four-Helix Bundle of Influenza A M2 Protein Channel: Structural Implications from Helix Tilt and Orientation. *Biophys J*. 1997; **73**(5):2511–2517.

(170) Pinto, L.H.; Dieckmann, G.R.; Gandhi, C.S.; Papworth, C.G.; Braman, J.; Shaughnessy, M.A.; Lear, J.D.; Lamb, R.A.; DeGrado, W.F. A Functionally Defined Model for the M_2 Proton Channel of Influenza A Virus Suggests a Mechanism for its Ion Selectivity. *Proc Natl Acad Sci USA*. 1997;**94**(21):11301–11306.

(171) Forrest, L.R.; Kukol, A.; Arkin, I.T.; Tieleman, D.P.; Sansom, M.S.P. Exploring Models of the Influenza A M2 Channel: MD Simulations in a Phospholipid Bilayer. *Biophys J*. 2000; **78**(1):55–69.

(172) Venkataraman, P.; Lamb, R.A.; Pinto, L.H. Chemical Rescue of Histidine Selectivity Filter Mutants of the M2 Ion Channel of Influenza A Virus. *J Biol Chem*. 2005;**280**(22):21463–21472.

(173) Sansom, M.S.P.; Kerr, I.D.; Smith, G.R.; Son, H.S. The Influenza A Virus M2 Channel: A Molecular Modeling and Simulation Study. *Virology*. 1997;**233**(1):163–173.

(174) Agmon, N. The Grotthuss Mechanism. *Chem Phys Lett*. 1995;**244**(5-6):456–462.

(175) Kass, I.; Arkin, I.T. How pH Opens a H^+ Channel: The Gating Mmechanism of Influenza A M2. *Structure*. 2005;**13**(12):1789–1798.

(176) Wu, Y.J.; Voth, G.A. A Computational Study of the Closed and Open States of the Influenza A M2 Proton Channel. *Biophys J*. 2005;**89**(4):2402–2411.

(177) Zhong, Q.F.; Husslein, T.; Moore, P.B.; Newns, D.M.; Pattnaik, P.; Klein, M.L. The M2 Channel of Influenza A Virus: A Molecular Dynamics Study. *FEBS Lett*. 1998;**434**(3):265–271.

(178) Schweighofer, K.J.; Pohorille, A. Computer Simulation of Ion Channel Gating: The M_2 Channel of Influenza A Virus in a Lipid Bilayer. *Biophys J*. 2000;**78**(1):150–163.

(179) Nemukhin, A.V.; Grigorenko, B.L.; Topol, I.A.; Burt, S.K. Quantum Chemical Simulations of the Proton Transfer in Water Wires Attached to Molecular Walls. *J Phys Chem B*. 2003; **107**(13):2958–2965.

(180) Hu, J.; Fu, R.; Nishimura, K.; Zhang, L.; Zhou, H.X.; Busath, D.D.; Vijayvergiya, V.; Cross, T.A. Histidines, Heart of the Hydrogen Ion Channel from Influenza A Virus: Toward an Understanding of Conductance and Proton Selectivity. *Proc Natl Acad Sci USA*. 2006;**103**(18):6865–6870.

(181) Adams, P.D.; Arkin, I.T.; Engelman, D.M.; Brünger, A.T. Computational Searching and Mutagenesis Suggest a Structure for the Pentameric Transmembrane Domain of Phospholamban. *Nat Struct Mol Biol*. 1995;**2**(2):154–162.

(182) Ben-Tal, N.; Honig, B. Helix-Helix Interactions in Lipid Bilayers. *Biophys J*. 1996; **71**(6):30463050.

(183) Forrest, L.R.; DeGrado, W.F.; R., D.G.; Sansom, M.S.P. Two Models of the Influenza A M2 Channel Domain: Verification by Comparison. *Fold Des*. 1998;**3**(6):443–448.

(184) Smondyrev, A.M.; Voth, G.A. Molecular Dynamics Simulation of Proton Transport through the Influenza A Virus M2 Channel. *Biophys J*. 2002;**83**(4):1987–1996.

(185) Stouffer, A.L.; Acharya, R.; Salom, D.; Levine, A.S.; Costanzo, L.D.; Soto, C.S.; Tereshko, V.; Nanda, V.; Stayrook, S.; F. DeGrado, W. Structural Basis for the Function and Inhibition of an Influenza Virus Proton Channel. *Nature*. 2008;**451**(7178):596–600.

(186) Hu, J.; Asbury, T.; Achuthan, S.; Li, C.; Bertram, R.; Quine, J.R.; Fu, R.; Cross, T.A. Backbone Structure of the Amantadine-Blocked Trans-Membrane Domain M2 Proton Channel from Influenza A Virus. *Biophys J*. 2007;**92**(12):4335–4343.

(187) Schnell, J.R.; Chou, J.J. Structure and Mechanism of the M2 Proton Channel of Influenza A Virus. *Nature*. 2008;**451**(7178):591–595.

(188) Tian, C.; Gao, P.F.; Pinto, L.H.; Lamb, R.A.; Cross, T.A. Initial Structural and Dynamic Characterization of the M2 Protein Transmembrane and Amphipathic Helices in Lipid Bilayers. *Protein Sci*. 2003;**12**(11):2597–2605.

(189) Zhong, Q.; Newns, D.M.; Pattnaik, P.; Lear, J.D.; Klein, M.L. Two Possible Conducting States of the Influenza A Virus M2 Ion Channel. *FEBS Lett*. 2000;**473**(2):195–198.

(190) Moffat, J.C.; Vijayvergiya, V.; Gao, P.F.; Cross, T.A.; Woodbury, D.J.; Busath, D.D. Proton Transport through Influenza A Virus M2 Protein Reconstituted in Vesicles. *Biophys J*. 2008; **94**(2):434–445.

(191) Dougherty, D.A. Cation-π Interactions in Chemistry and Biology: A New View of Benzene, Phe, Tyr, and Trp. *Science*. 1996;**271**(5246):163–168.

(192) Mecozzi, S.; West, A.P., Jr.; Dougherty, D.A. Cation–π Interactions in Aromatics of Biological and Medicinal Interest: Electrostatic Potential S—urfaces as a Useful Qualitative Guide. *Proc Natl Acad Sci USA*. 1996;**93**(20):1056610571.

(193) Mecozzi, S.; West, A.P., Jr.; Dougherty, D.A. Cation–π Interactions in Simple Aromatics: Electrostatics Provide a Predictive Tool. *J Am Chem Soc*. 1996;**118**(9):2307–2308.

(194) Gallivan, J.P.; Dougherty, D.A. Cation–π Interactions in Structural Biology. *Proc Natl Acad Sci USA*. 1999;**96**(17):9459–9464.

(195) Beene, D.L.; Brandt, G.S.; Zhong, W.; Zacharias, N.M.; Lester, H.A.; Dougherty, D.A. Cation–π Interactions in Ligand Recognition by Serotonergic (5-ht_{3A}) and Nicotinic Acetylcholine Receptors: The Anomalous Binding Properties of Nicotine. *Biochemistry*. 2002; **41**(32):10262–10269.

(196) Shi, Z.; Olson, C.A.; Kallenbach, N.R. Cation–π Interaction in Model α-Helical Peptides. *J Am Chem Soc*. 2002;**124**(13):3284–3291.

(197) Ammal, S.S.C.; Venuvanalingam, P. π–Systems as Lithium/Hydrogen Bond Acceptors: Some Theoretical Observations. *J Chem Phys*. 1998;**109**(22):9820–9830.

(198) Mould, J.A.; Li, H.C.; Dudlak, C.S.; Lear, J.D.; Pekosz, A.; Lamb, R.A.; Pinto, L.H. Mechanism for Proton Conduction of the M_2 Ion Channel of Influenza A Virus. *J Biol Chem*. 2000; **275**(12):8592–8599.

(199) Nagy, P.I.; Durant, G.J.; Smith, D.A. Theoretical Studies on Hydration of Pyrrole, Imidazole, and Protonated Imidazole in the Gas Phase and Aqueous Solution. *J Am Chem Soc*. 1993; **115**(7):2912–2922.